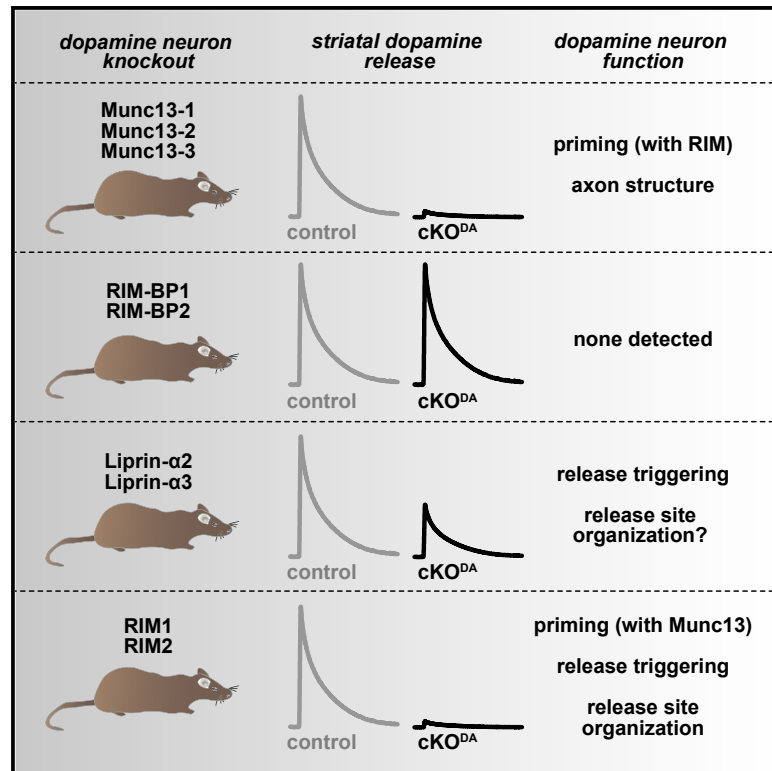


## Molecular and functional architecture of striatal dopamine release sites

### Graphical abstract



### Authors

Aditi Banerjee, Cordelia Imig, Karthik Balakrishnan, ..., Sonja M. Wojcik, Nils Brose, Pascal S. Kaeser

### Correspondence

kaeser@hms.harvard.edu

### In brief

Dopamine is a key neuromodulator for the control of striatal circuit function. Banerjee et al. show that evoked dopamine secretion occurs at release hotspots that contain active zone proteins. Munc13, Liprin- $\alpha$ , and RIM cooperate to mediate vesicle priming and release, while other known active zone proteins are dispensable.

### Highlights

- Evoked striatal dopamine release necessitates the active zone proteins Munc13 and RIM
- Ablating Munc13 from dopamine neurons leads to defects in their axon structure
- Dopamine release depends on Liprin- $\alpha$ 2 and Liprin- $\alpha$ 3, but not on RIM-BP1 and RIM-BP2
- RIM domains that bind to Munc13 and Liprin- $\alpha$  restore some release after RIM ablation



## Article

# Molecular and functional architecture of striatal dopamine release sites

Aditi Banerjee,<sup>1,3</sup> Cordelia Imig,<sup>2,3,4</sup> Karthik Balakrishnan,<sup>1</sup> Lauren Kershberg,<sup>1</sup> Noa Lipstein,<sup>2,5</sup> Riikka-Liisa Uronen,<sup>2</sup> Jiexin Wang,<sup>1,6</sup> Xintong Cai,<sup>1</sup> Fritz Benseler,<sup>2</sup> Jeong Seop Rhee,<sup>2</sup> Benjamin H. Cooper,<sup>2</sup> Changliang Liu,<sup>1</sup> Sonja M. Wojcik,<sup>2</sup> Nils Brose,<sup>2</sup> and Pascal S. Kaeser<sup>1,7,\*</sup>

<sup>1</sup>Department of Neurobiology, Harvard Medical School, Boston, MA 02115, USA

<sup>2</sup>Department of Molecular Neurobiology, Max Planck Institute of Experimental Medicine, 37075 Göttingen, Germany

<sup>3</sup>These authors contributed equally

<sup>4</sup>Present address: Department of Neuroscience, University of Copenhagen, 2200 Copenhagen, Denmark

<sup>5</sup>Present address: Leibniz-Forschungsinstitut für Molekulare Pharmakologie (FMP), 13125 Berlin, Germany

<sup>6</sup>Present address: Department of Neuroscience and Behavior, University of Massachusetts Amherst, Amherst, MA 01003, USA

<sup>7</sup>Lead contact

\*Correspondence: [kaeser@hms.harvard.edu](mailto:kaeser@hms.harvard.edu)

<https://doi.org/10.1016/j.neuron.2021.10.028>

## SUMMARY

Despite the importance of dopamine for striatal circuit function, mechanistic understanding of dopamine transmission remains incomplete. We recently showed that dopamine secretion relies on the presynaptic scaffolding protein RIM, indicating that it occurs at active zone-like sites similar to classical synaptic vesicle exocytosis. Here, we establish using a systematic gene knockout approach that Munc13 and Liprin- $\alpha$ , active zone proteins for vesicle priming and release site organization, are important for dopamine secretion. Furthermore, RIM zinc finger and C<sub>2</sub>B domains, which bind to Munc13 and Liprin- $\alpha$ , respectively, are needed to restore dopamine release after RIM ablation. In contrast, and different from typical synapses, the active zone scaffolds RIM-BP and ELKS, and RIM domains that bind to them, are expendable. Hence, dopamine release necessitates priming and release site scaffolding by RIM, Munc13, and Liprin- $\alpha$ , but other active zone proteins are dispensable. Our work establishes that efficient release site architecture mediates fast dopamine exocytosis.

## INTRODUCTION

Dopamine is a crucial neuromodulator for the control of locomotion, motivation, and reward. Although there is rich literature on dopamine action, dopamine signaling mechanisms remain incompletely understood. An important dopamine pathway in the vertebrate brain arises from cell bodies in the ventral midbrain, whose axons prominently project to the striatum. In the striatum, dopamine axons are extensively branched. A single axon covers a large area, and ascending action potentials as well as local regulatory mechanisms are important for dopamine release (Liu and Kaeser, 2019; Matsuda et al., 2009; Sulzer et al., 2016).

Dopamine is often considered a volume transmitter with slow and imprecise signaling: the majority of striatal dopamine varicosities lack synaptic specializations, dopamine receptors on target cells appear to be localized away from release sites, and timescales of G protein-coupled receptor (GPCR) signaling are orders of magnitude slower than those of ionotropic receptors (Agnati et al., 1995; Descarries et al., 1996; Missale et al., 1998; Uchigashima et al., 2016). Recent studies, however, showed that dopamine influences synapses and behavior with sub-sec-

ond precision (Howe and Dombeck, 2016; Menegas et al., 2018; Yagishita et al., 2014), and dopamine receptor activation can occur rapidly and requires a high dopamine concentration (Beckstead et al., 2004; Courtney and Ford, 2014; Gantz et al., 2018; Marcott et al., 2018), challenging the model of volume transmission. How signaling structures between dopamine-releasing and dopamine-receiving cells are organized to support such precise functions remains largely unknown (Liu et al., 2021). We recently showed that action potential-triggered dopamine release is executed with millisecond precision and requires the presynaptic scaffolding protein RIM (Banerjee et al., 2020; Liu et al., 2018; Robinson et al., 2019). This led to the working model that dopamine release is mediated at specialized secretory sites, but organizers of release site structure beyond RIM are not known. As an alternative to a scaffolded release site, it is possible that tethering functions of RIM are not important in dopamine varicosities. RIM could instead mediate dopamine secretion as a soluble protein or through association with vesicles.

At conventional synapses, exocytosis is ultrafast, triggered by Ca<sup>2+</sup>, and occurs only within the active zone (Kaeser and Regehr, 2014; Südhof, 2012). In addition to RIM, the active zone contains



members of five protein families: Munc13, ELKS, Liprin- $\alpha$ , RIM-BP, and Bassoon/Piccolo (Betz et al., 1998; Emperador-Melero and Kaeser, 2020; Wang et al., 2016; Wong et al., 2018). Together, these proteins form a molecular machine for the spatiotemporal control of secretion via three main mechanisms. First, docking and priming, mediated by RIM and Munc13, render vesicles ready for fast release (Augustin et al., 1999; Betz et al., 2001; Deng et al., 2011; Koushika et al., 2001; Richmond et al., 1999; Siksou et al., 2009; Varoqueaux et al., 2002). Second, the coupling of  $\text{Ca}^{2+}$  entry to these release-ready vesicles through close-by positioning of  $\text{Ca}^{2+}$  channels is orchestrated by a complex between RIM-BP, RIM, and channels of the  $\text{Ca}_v2$  family (Han et al., 2011; Held et al., 2020; Hibino et al., 2002; Kaeser et al., 2011; Liu et al., 2011; Müller et al., 2012). Third, the active zone coordinates the organization and function of essential release machinery components, including SNARE proteins and lipids, for example phosphatidylinositol 4,5-bisphosphate ( $\text{PIP}_2$ ) (van den Bogaart et al., 2011; Honigmann et al., 2013; de Jong et al., 2018; Ma et al., 2011; Milosevic et al., 2005; Di Paolo and De Camilli, 2006).

Striatal dopamine release is fast and has a high release probability (Banerjee et al., 2020; Liu et al., 2018), indicating the presence of active zone scaffolds to organize release. Indeed, dopamine axons contain at least some active zone proteins (e.g., RIM, ELKS, Munc13, Bassoon) (Daniel et al., 2009; Liu et al., 2018; Silm et al., 2019; Uchigashima et al., 2016). Moreover, removal of RIM specifically from dopamine neurons abolishes evoked dopamine release, while action potential-independent release persists (Liu et al., 2018; Robinson et al., 2019). In contrast, ELKS is dispensable, and roles of other active zone proteins are unknown (Liu and Kaeser, 2019; Liu et al., 2018). Altogether, it has remained uncertain whether dopamine axons use priming and scaffolding mechanisms similar to conventional synapses. Instead, dopamine release may not require the typical complement of active zone proteins, as has been proposed for the release of peptides, catecholamines, and other non-synaptic transmitters (Berwin et al., 1998; van de Bospoort et al., 2012; Farina et al., 2015; Held and Kaeser, 2018; van Keimpema et al., 2017; Liu et al., 2010; Renden et al., 2001). Likewise, dopamine release only partially depends on  $\text{Ca}^{2+}$  entry through  $\text{Ca}_v2$  channels (Brimblecombe et al., 2015), indicating that mechanisms other than those mediating the specific tethering of  $\text{Ca}_v2$ s are important.

Here, we determined functions of key active zone proteins in dopamine secretion and complemented this analysis with assessing roles of RIM domains that interact with these proteins. We show that Munc13 is essential for dopamine release and establish that interplay between RIM and Munc13 is important for priming of dopamine-laden vesicles. We find that scaffolding requirements of dopamine release sites are different from those at classical active zones: ELKS and RIM-BP are dispensable, and the RIM domains that bind to them do not contribute to release. Liprin- $\alpha2/3$  knockout leads to a ~50% impairment in dopamine release, and dopamine release is restored in RIM knockouts by re-expressing a fusion construct of the RIM zinc finger (which binds to Munc13) with the RIM  $\text{C}_2\text{B}$  domain (which binds to Liprin- $\alpha$ ). We conclude that dopamine release sites contain molecular scaffolds of relatively low complexity

compared with classical active zones. They use Munc13-mediated vesicle priming for fast release and rely on RIM, Munc13, and Liprin- $\alpha$  for release site scaffolding.

## RESULTS

### RIM domains cooperate in dopamine release

Molecular mechanisms of RIM function in dopamine release are unknown. At conventional synapses, RIM initiates vesicle priming via recruiting and activating Munc13, to which it binds with its N-terminal zinc finger domain (Figure 1A) (Andrews-Zwilling et al., 2006; Betz et al., 2001; Deng et al., 2011; Kaeser and Regehr, 2017). The RIM PDZ domain directly binds to  $\text{Ca}_v2$  channels and tethers them in concert with RIM-BP, which binds to a short proline-rich region of RIM between the C-terminal  $\text{C}_2$  domains (Hibino et al., 2002; Kaeser et al., 2011). The RIM  $\text{C}_2\text{A}$  and  $\text{C}_2\text{B}$  domains bind to  $\text{PIP}_2$ , and  $\text{C}_2\text{B}$  also interacts with Liprin- $\alpha$  and is essential for RIM function (de Jong et al., 2018; Koushika et al., 2001; Schoch et al., 2002).

We started assessing dopamine release mechanisms by rescue of RIM knockout phenotypes in striatal slices using amperometric recordings. We confirmed that conditional knockout of RIM in dopamine neurons (RIM  $\text{cKO}^{\text{DA}}$ ), generated by crossing floxed alleles for both RIM genes to  $\text{DAT}^{\text{IRES-cre}}$  mice (Bäckman et al., 2006; Kaeser et al., 2008, 2011; Liu et al., 2018), abolishes dopamine release evoked by electrical stimulation and KCl puffs (Figures 1B–1F). Electrical stimulation induces release through both the activation of dopamine axons and of cholinergic interneurons (Figure S1A), which trigger dopamine release via nicotinic acetylcholine receptors (nAChRs) on dopamine axons (Cachope et al., 2012; Giurguieff et al., 1976; Liu et al., 2018; Threlfell et al., 2012; Zhou et al., 2001). Adeno-associated viruses (AAVs) do not allow expression of full-length RIM from a single virus for rescue as the RIM coding sequence exceeds the packaging limit. We instead re-expressed either the RIM zinc finger domain (RIM1-Zn) or the C-terminal scaffolding sequences (RIM1- $\Delta\text{Zn}$ ), which together account for the known RIM domains (Figure 1G). Expression was restricted to midbrain dopamine neurons through the use of cre-dependent AAVs delivered by stereotaxic injection at postnatal day 33 (P33) to P54 and was confirmed via western blotting of striatal brain homogenates 7–10 weeks after injection (Figure S1B). We measured dopamine release in RIM  $\text{cKO}^{\text{DA}}$  mice injected either with a control virus or after re-expression of RIM1-Zn, RIM1- $\Delta\text{Zn}$ , or both. Each experiment was performed on two RIM  $\text{cKO}^{\text{DA}}$  mice (one with and one without rescue) on the same day (Figures 1H–1S), and an unrelated control mouse was recorded first on each day to establish stable dopamine detection (Figures S1C–S1H; all three mice were analyzed using the same carbon fiber electrode).

Expression of RIM1-Zn or RIM1- $\Delta\text{Zn}$  alone showed no rescue of dopamine release evoked by electrical stimulation when compared to RIM  $\text{cKO}^{\text{DA}}$  (Figures 1H–1K). This is surprising because similar constructs partially restore exocytosis of synaptic or peptidergic vesicles (Kaeser et al., 2011; Persoon et al., 2019). When RIM1-Zn and RIM1- $\Delta\text{Zn}$  were co-expressed, we observed some but incomplete rescue of dopamine release (Figures 1L and 1M). We next assessed dopamine release in

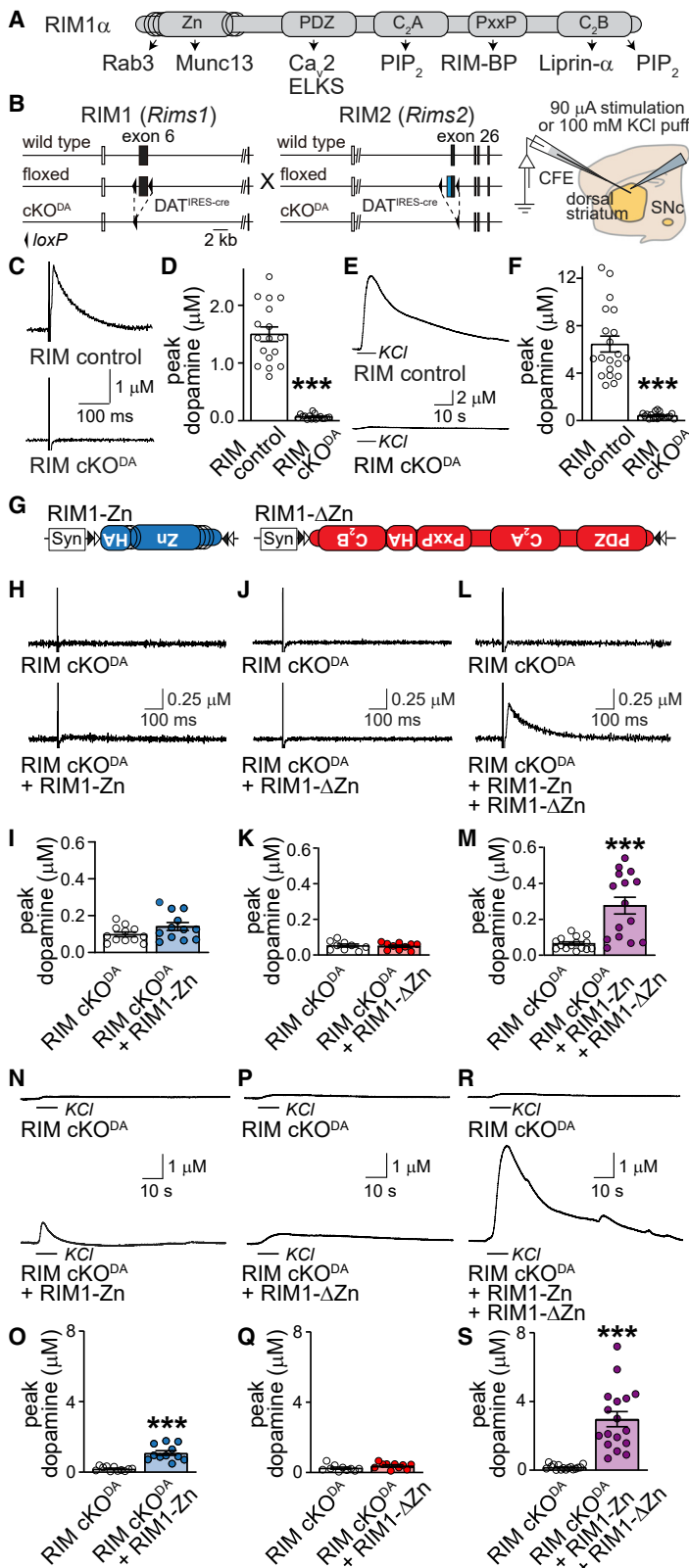


**Figure 1. RIM N- and C-terminal domains are necessary for evoked dopamine release**

(A) Schematic of RIM1 $\alpha$  domain structure and select interactions.

(B) Strategy for ablation of RIM1 $\alpha\beta$  and RIM2 $\alpha\beta\gamma$  in dopamine neurons (RIM cKO<sup>DA</sup>) and schematic of slice recordings, SNc: substantia nigra pars compacta.

(C and D) Sample traces (C, single sweeps) and quantification (D) of dopamine release in the dorsolateral striatum evoked by a 90  $\mu$ A electrical stimulus and measured using carbon fiber amperometry in acute brain slices, 17 slices/3 mice each.

(E and F) Sample traces (E) and quantification (F) of dopamine release evoked by a 100 mM KCl puff, 20/3 each.

(G) Schematic of AAV5 rescue viruses injected either alone or together into the midbrain. For all AAVs, a double-floxed inverted strategy restricts expression to cre-expressing neurons.

(H–M) Sample traces (H, J, and L, single sweeps) and quantification (I, K, and M) of dopamine release as in (C) and (D); (I) 12/4 each; (K) RIM cKO<sup>DA</sup> 9/3, RIM cKO<sup>DA</sup> + RIM1- $\Delta$ Zn 10/3; (M) 15/4 each.

(N–S) Same as (H)–(L), but for a local 100 mM KCl puff; (O) 11/4 each; (Q) 10/3 each; (S) RIM cKO<sup>DA</sup> 16/4, RIM cKO<sup>DA</sup> + RIM1-Zn + RIM1- $\Delta$ Zn 17/4.

Data are mean  $\pm$  SEM. \*\*\*p < 0.001 as assessed using Mann-Whitney tests. For means and errors, p values and the number of observations used for statistics for this and all following figures, see corresponding Tables S1–S8. For rescue expression and additional recordings, see Figure S1.

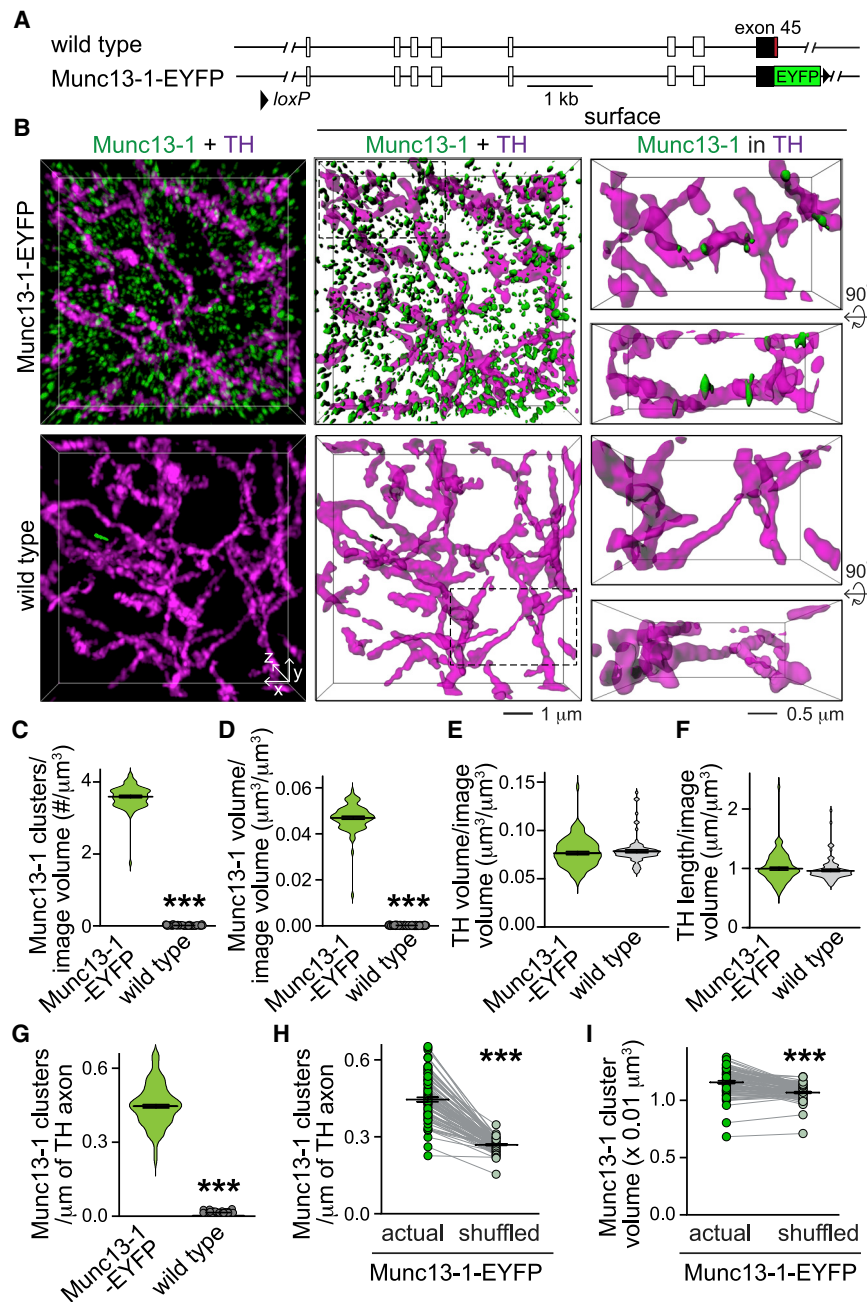


**Figure 2. Munc13-1 is present in sparse clusters in dopamine axons**

(A) Schematic of the Munc13-1-EYFP knockin mice.

(B) Sample 3D-SIM images of dorsolateral striatum stained with GFP antibodies (to detect Munc13-1) and TH antibodies (to visualize dopamine axons). Volume rendered images ( $10 \times 10 \times 2 \mu\text{m}^3$ ) showing Munc13-1 and TH (left), surface-rendered images of the same volumes (middle), and magnified view (right,  $5 \times 3 \times 2 \mu\text{m}^3$  from dotted rectangle in middle, frontal, and  $90^\circ$  rotated views of only Munc13-1 clusters with  $>40\%$  volume overlap with TH).

(C–I) Quantification of (B). For (H) and (I), each Munc13-1 object was locally (within  $1 \times 1 \times 1 \mu\text{m}^3$ ) and randomly shuffled 1,000 times, and the actual Munc13-1 densities and volumes were compared with the averaged result after shuffling; Munc13-1-EYFP 88 images/3 mice; wild-type 86/3.

Data are mean  $\pm$  SEM. \*\*\* $p < 0.001$  as assessed using unpaired (C–G) and paired (H and I) t tests.

### Munc13-1 forms small clusters in striatal dopamine axons

We next aimed to systematically assess loss-of-function phenotypes of RIM-interacting active zone proteins. The RIM zinc finger may enhance dopamine release through vesicle priming. At neuronal synapses, vesicle priming is executed by Munc13, which is recruited and activated by RIM zinc finger domains (Andrews-Zwilling et al., 2006; Augustin et al., 1999; Betz et al., 1998; Deng et al., 2011). Given the prominent role of RIM in dopamine release, we hypothesized that dopamine vesicles are primed by Munc13.

Of the three major brain Munc13 isoforms (Munc13-1, Munc13-2, and Munc13-3), Munc13-1 is strongly expressed in midbrain dopamine neurons, while the other Munc13s may be present at low levels (Lein et al., 2007; Saunders et al., 2018). Previous experiments in striatal synaptosomes suggested that Munc13-1 is present in dopamine varicosities and colocalizes with the release site marker Bassoon (Liu et al., 2018). However, a lack of suitable antibodies prevented the assessment of Munc13 distribution in intact striatum using superresolution microscopy. To circumvent this caveat, we used mice in which endogenous Munc13-1 is tagged with EYFP (Figure 2A) (Kalla et al., 2006). We stained striatal brain sections with anti-GFP antibodies and assessed signal distribution in tyrosine hydroxylase (TH)-labeled dopamine axons with three-dimensional structured illumination microscopy (3D-SIM) (Gustafsson et al., 2008; Liu et al., 2018) followed by an analysis pipeline detailed in the STAR Methods. As expected for a

response to depolarization triggered by local puff application of KCl. KCl-induced dopamine release depends on extracellular  $\text{Ca}^{2+}$  (Figures S1I and S1J) but not on nAChR or sodium channel activation (Figures S1K and S1L) and is absent in RIM cKO<sup>DA</sup> mice (Figures 1E and 1F) (Liu et al., 2018). RIM1-Zn mediated a small amount of KCl-triggered release, RIM1- $\Delta\text{Zn}$  was inactive, and combined expression led to more robust rescue (Figures 1N–1S). These data establish that the RIM cKO<sup>DA</sup> phenotype is partially reversible and that co-expression of RIM zinc finger and scaffolding domains is needed for action potential-triggered release.

As expected for a

prominent synaptic protein, Munc13-1 is abundant in the striatum and present in small clusters (Figures 2B–2D). TH labeling was similar between Munc13-1-EYFP and controls (Figures 2E and 2F), and we used a 40% volume overlap criterion as established before (Liu et al., 2018) to identify Munc13-1 clusters localized in TH axons. On average, there was one Munc13-1 cluster per  $\sim 2.5 \mu\text{m}$  of TH axon, and the average cluster volume was  $\sim 0.01 \mu\text{m}^3$  (Figures 2G–2I). We used local shuffling of Munc13 clusters to further assess the signal. Munc13-1 cluster density within dopamine axons dropped after shuffling, establishing that Munc13-1 clusters were more frequently present within TH axons than in their immediate environment. Furthermore, Munc13-1 clusters within TH axons were larger than the clusters detected after shuffling (which likely represent Munc13-1 clusters of close-by conventional synapses). These findings establish that Munc13-1 is present in clusters within dopamine axons and thus agree with our earlier findings made in synaptosomes (Liu et al., 2018).

### Munc13 is essential for evoked striatal dopamine release

To assess roles of Munc13 in dopamine release, we developed mouse mutants for deletion of Munc13-1, Munc13-2, and Munc13-3. We circumvented lethality of constitutive Munc13-1 deletion through the generation of Munc13-1 conditional knockout mice in which exon 21 was flanked with *loxP* sites by homologous recombination in embryonic stem cells (Figures S2A and S2B). The Munc13-1 floxed mice had normal Munc13-1 levels (Figures S2C and S2D) and germline cre-recombination removed full-length Munc13-1 (Figures S2E and S2F). A very small amount of Munc13-1 (<5%) at a slightly lower molecular weight persisted, likely representing a protein that lacks exons 21 and 22 (Figure S2E). In cultured autaptic neurons of these mice, excitatory synaptic transmission was strongly impaired but not abolished (Figure S3), with a dramatic reduction in the readily releasable pool (Figures S3F and S3G), but a larger evoked excitatory postsynaptic current (EPSC) (Figures S3D and S3E) than expected from previous constitutive Munc13-1 knockout mice (Augustin et al., 1999). This difference may be due to the persistence of a small amount of the shorter and possibly partially active Munc13-1 variant in the new mutant (Figures S2E and S2F).

To test whether Munc13 is needed for dopamine release, we crossed the Munc13-1 conditional (floxed) allele to constitutive Munc13-2 and Munc13-3 knockout mice (Augustin et al., 2001; Varoqueaux et al., 2002) and to DAT<sup>ires-cre</sup> mice (Bäckman et al., 2006; Figure 3A). Munc13 cKO<sup>DA</sup> mice (Munc13-1<sup>+/f</sup> × Munc13-2<sup>-/-</sup> × Munc13-3<sup>-/-</sup> × DAT<sup>ires-cre</sup> <sup>+/cre</sup>) and Munc13 control mice (Munc13-1<sup>+/f</sup> × Munc13-2<sup>+/-</sup> × Munc13-3<sup>-/-</sup> × DAT<sup>ires-cre</sup> <sup>+/cre</sup>) were generated from the same crossings. To selectively activate dopamine axons, we expressed a fast version of channelrhodopsin (oChIEF; Lin et al., 2009) specifically in dopamine neurons using cre-dependent AAVs delivered by stereotaxic injections (Figure 3B) at P29–P36 (Banerjee et al., 2020; Liu et al., 2018). Three or more weeks after injection, we prepared acute brain slices and measured dopamine release triggered by optogenetic activation. In Munc13 control mice, dopamine release appeared normal and very similar in extent

to other control mice (Liu et al., 2018; Figures 6 and 7). Peak amplitudes strongly depressed during brief stimulus trains, indicative of a high initial release probability as described (Liu et al., 2018). Release was abolished by the sodium channel blocker tetrodotoxin (TTX; Figures 3C and 3D), establishing that optogenetic stimulation triggers release through inducing action potentials. Strikingly, dopamine release was almost completely absent in Munc13 cKO<sup>DA</sup> mice, and there was no buildup of release during short stimulus trains (Figures 3C–3E). Action potentials were readily elicited by light stimulation in Munc13 cKO<sup>DA</sup> mice (Figure S4). In Munc13 control mice, KCl puffs triggered dopamine release with a  $\sim 3.5$ -fold larger amplitude than release evoked by optogenetic stimulation (Figures 3F–3H). In Munc13 cKO<sup>DA</sup> mice, KCl application did not induce detectable release. Finally, electrical stimulation also failed to induce robust release in these mutants (Figures 4A–4D). We conclude that Munc13 is essential for depolarization-induced dopamine secretion and even strong stimuli fail to elicit significant release after removing Munc13.

To determine whether Munc13 is important for dopamine release *in vivo*, we performed microdialysis in anesthetized mice (Figure 4E). In control mice, extracellular dopamine was reduced to  $\sim 25\%$  of its initial levels by reverse dialysis of TTX (to block firing). In Munc13 cKO<sup>DA</sup> mice, dopamine levels were strongly decreased at baseline. Reverse dialysis of TTX only mildly reduced extracellular dopamine, and after TTX the dopamine levels between Munc13 control and cKO<sup>DA</sup> mice were indistinguishable. We conclude that Munc13 is essential for action potential-triggered dopamine release *in vivo*. Notably, some extracellular dopamine persists after Munc13 knockout, and this could be due to release that is independent of Munc13 and action potentials similar to RIM-independent release (Liu et al., 2018; Robinson et al., 2019), release mediated by residual Munc13-1 (Figure S2), or—trivially—tissue damage during microdialysis.

### Roles for Munc13 in dopamine axon structure

Although Munc13 is essential for synaptic vesicle release, removal of Munc13 and the resulting block of glutamate release in cultured hippocampal neurons or slices did not detectably impair neuronal or synapse structure (Sigler et al., 2017; Varoqueaux et al., 2002). To assess whether Munc13 is important for axonal and release site structure in dopamine neurons, we first prepared synaptosomes from striatal homogenates of Munc13 control and Munc13 cKO<sup>DA</sup> mice (Figures 5A–5E) as described (Liu et al., 2018). This circumvents limitations of quantifying fluorescent signals in tissue densely packed with synapses. We stained synaptosomes with antibodies against the active zone marker Bassoon, the synaptic vesicle protein synaptophysin, and the dopamine neuron marker TH. We generated regions of interest (ROIs) containing TH (TH<sup>+</sup>) and synaptophysin (syp<sup>+</sup>) and quantified intensities within these ROIs as described in the STAR Methods. In Munc13 cKO<sup>DA</sup> TH<sup>+</sup> ROIs, TH intensities were moderately increased (Figure 5B) and those of synaptophysin were somewhat decreased (Figure 5C), suggesting structural alterations. Bassoon intensities, used as a proxy for release site structure, were increased in dopaminergic synaptosomes (TH<sup>+</sup>/syp<sup>+</sup> ROIs) after Munc13 ablation (Figures 5D and 5E). The same was true for TH<sup>+</sup> only ROIs for Bassoon (Figures S5A–S5C) and

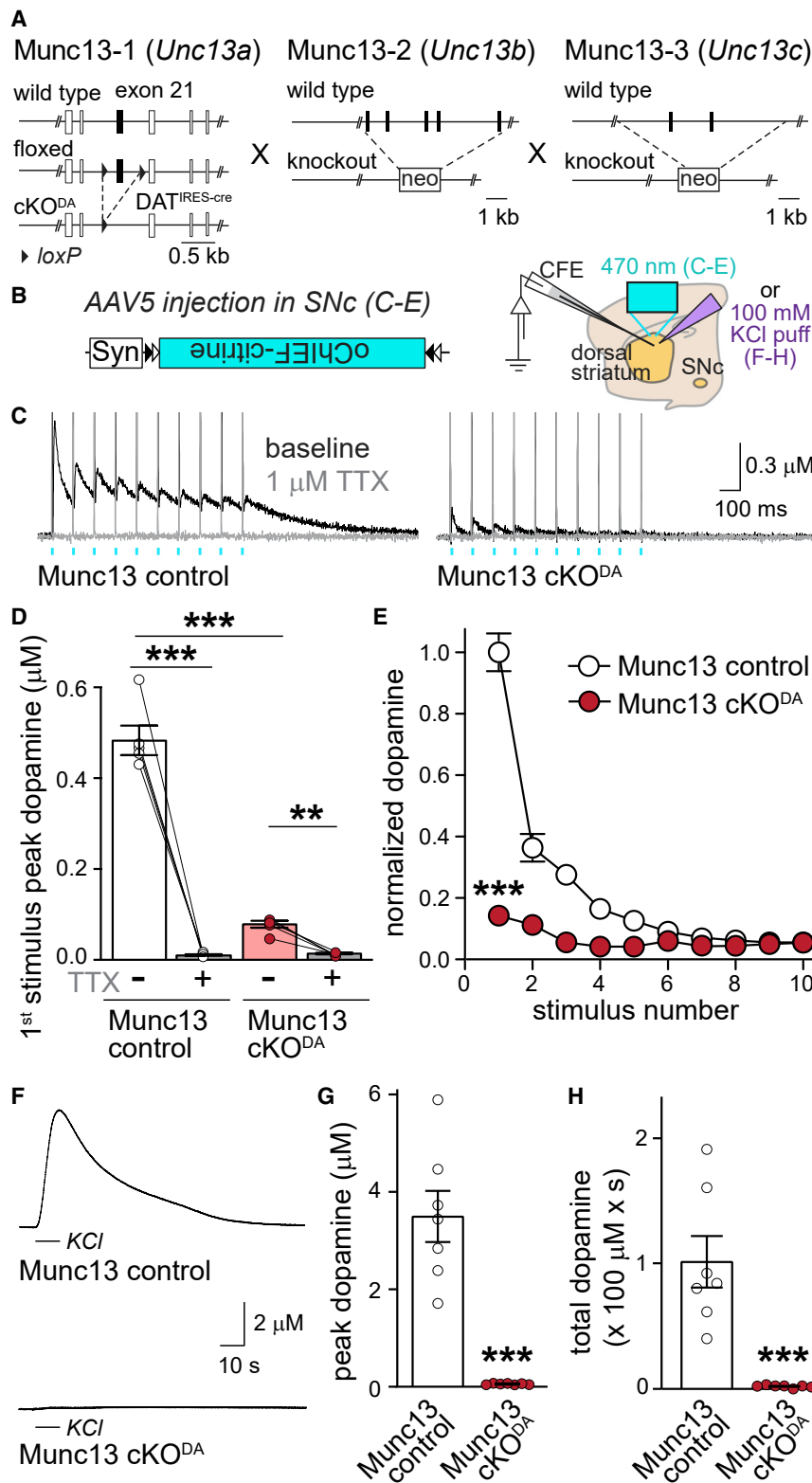


**Figure 3. Munc13 is essential for evoked dopamine release**

(A) Targeting strategy for deletion of Munc13-1, Munc13-2, and Munc13-3 (Munc13 cKO<sup>DA</sup>).

(B) Schematics of cre-dependent expression of oChIEF and of slice recordings.

(C–E) Sample traces (C, average of four sweeps) of dopamine release evoked by ten 1 ms light pulses at 10 Hz before and after TTX, quantification of the first stimulus amplitudes (D) and peak amplitudes normalized to the average first peak of Munc13 control (E); (D) 5 slices/3 mice each; (E) 6/3 each.

(F–H) Sample traces (F) and quantification of KCl-triggered peak dopamine release (G) and area under the curve (H, start of puff to 50 s), 7/3 each. Data are mean ± SEM. \*\*p < 0.01 and \*\*\*p < 0.001 as assessed using repeated-measures one-way ANOVA followed by Sidak's multiple-comparisons tests in (D); two-way ANOVA (\*\*p < 0.001 for genotype, stimulus number, and interaction) followed by Sidak's multiple-comparisons tests in E (\*\*p < 0.001 for stimuli 1–4, \*\*p < 0.01 for stimulus 5), and Mann-Whitney tests in (G) and (H). For generation and analyses of Munc13-1 cKO mice, see Figures S2 and S3; for extracellular recordings, see Figure S4.

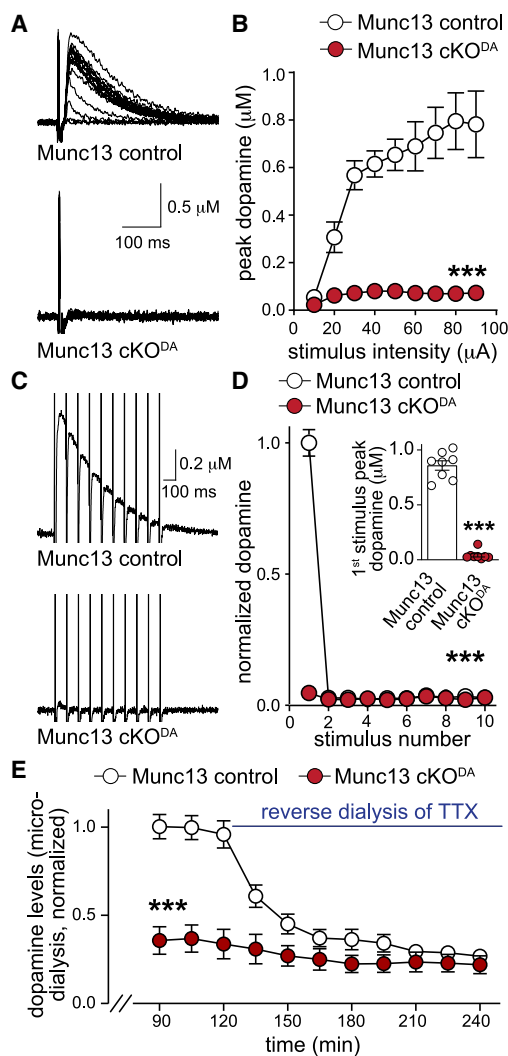


**Figure 4. Roles for Munc13 in other modes of dopamine release**  
 (A and B) Sample traces (A, single sweeps) and quantification of peak amplitudes (B) of dopamine release evoked by electrical stimulation (10–90  $\mu$ A single electrical pulses), 10 slices/5 mice each.  
 (C and D) Sample traces (C, average of four sweeps) and quantification of peak dopamine amplitudes normalized to the first peak amplitude of Munc13 control (D) in response to ten electrical pulses at 10 Hz; inset in (D) shows peak amplitude for the first stimulus, 8/4 each.  
 (E) Quantification of extracellular dopamine levels within dorsal striatum measured using *in vivo* microdialysis. Values were normalized to average dopamine values of the 76th to 120th min of Munc13 control. TTX (10  $\mu$ M) was reverse dialyzed starting at 121 min, 7 mice each.  
 Data are mean  $\pm$  SEM. \*\* $p < 0.01$  and \*\*\* $p < 0.001$  as assessed using two-way ANOVA ( $p < 0.001$  for genotype, stimulus intensity/stimulus number/time, and interaction) in (B), (D), and (E) followed by Sidak's multiple-comparisons tests (B, \*\* $p < 0.01$  for 20  $\mu$ A and \*\*\* $p < 0.001$  for 30–90  $\mu$ A; D, \*\*\* $p < 0.001$  for first stimulus; E, \*\*\* $p < 0.001$  for 90th to 150th min and \*\* $p < 0.01$  for 165th to 195th min), and Mann-Whitney test for inset in (D).

RIM (Figures S5D–S5F). Munc13 cKO<sup>DA</sup> did not affect Bassoon intensities in non-dopamine synaptosomes (TH<sup>-</sup>/syp<sup>+</sup> ROIs; Figure 5D).

To assess whether similar changes were present in intact striatum, we used 3D-SIM (Figures 5F–5L). In slices of the dorsolateral striatum, TH axons appeared less dense and irregular in shape in Munc13 cKO<sup>DA</sup> compared with control, the volume occupied by TH was somewhat reduced, and the length of the skeletonized TH axon network was decreased (Figures 5F–5H). When we plotted binned histograms of the radii of TH axons, a right shift was detected, indicating that there were more axonal segments with larger radii (Figures 5I and 5J). This likely explains the increased TH intensities in synaptosomes (Figure 5B). We further found that the density and volume of Bassoon clusters were higher after Munc13 ablation (Figures 5K and 5L), again matching with the synaptosome data (Figures 5D and 5E). Similar results were obtained for ELKS2 (Figures S5G–S5K), another active zone scaffold in dopamine axons. We conclude that Munc13 is necessary for normal dopamine axon structure. This role is likely independent of dopamine release impairments because ablation of RIM or synaptotagmin-1 induce similarly strong dopamine secretory defects, but TH axons appear less prominently affected in these mutants (Banerjee et al., 2020; Liu et al., 2018).

#### RIM-BP1 and RIM-BP2 are dispensable for dopamine release

RIM and Munc13 control dopamine release likely via vesicle priming. Restoring their interaction by expressing the RIM zinc finger in RIM cKO<sup>DA</sup> mice, however, is not sufficient to rescue dopamine release; C-terminal sequences are also needed (Figure 1). At conventional synapses, the C-terminal RIM domains mediate scaffolding, including the tethering of Ca<sup>2+</sup> channels (Han et al., 2011; Kaeser et al., 2011). RIM contributes to this function in a tripartite complex with Ca<sub>v</sub>2s and RIM-BP (Acuna et al., 2016; Hibino et al., 2002; Kaeser et al., 2011; Liu et al., 2011). It is noteworthy that striatal dopamine release is partially resistant to blockade of Ca<sub>v</sub>2.1 (P/Q-type) and 2.2 (N-type) channels (Brimblecombe et al., 2015), establishing the contribution of other Ca<sup>2+</sup> sources. RIM-BP expression is detected in dopamine neurons (Lein et al., 2007; Saunders et al., 2018), and RIM-BPs would be suited to couple to both Ca<sub>v</sub>2s and other Ca<sub>v</sub>s, for example Ca<sub>v</sub>1s, because RIM-BP SH3 domains bind to proline-rich regions of Ca<sub>v</sub>1 and Ca<sub>v</sub>2 C termini (Hibino et al., 2002).

We ablated RIM-BP1 and RIM-BP2 from dopamine neurons (RIM-BP cKO<sup>DA</sup>; Figure 6A) by crossing “floxed” alleles for these genes (Acuna et al., 2015) to DAT<sup>ires-cre</sup> mice (Bäckman et al., 2006). Surprisingly, dopamine release evoked by optogenetic activation (Figures 6B–6D), electrical stimulation (Figure S6), or KCl depolarization (Figures 6E–6G) was not affected by RIM-BP ablation. Although it is possible that RIM-BP1/2 cKO<sup>DA</sup> has subtle effects on dopamine secretion that cannot be detected with the approaches used here, our results establish that RIM-BPs are mostly dispensable for striatal dopamine release, different from mouse hippocampal mossy fiber synapses, the mouse calyx of Held, and the fly neuromuscular junction, where RIM-BP has robust roles (Acuna et al., 2015; Brockmann et al., 2019; Liu et al., 2011).

#### Roles for Liprin- $\alpha$ 2 and Liprin- $\alpha$ 3 in dopamine release

Given that RIM-BP (Figure 6) and ELKS (Liu et al., 2018) are dispensable for dopamine release, other C-terminal interactions



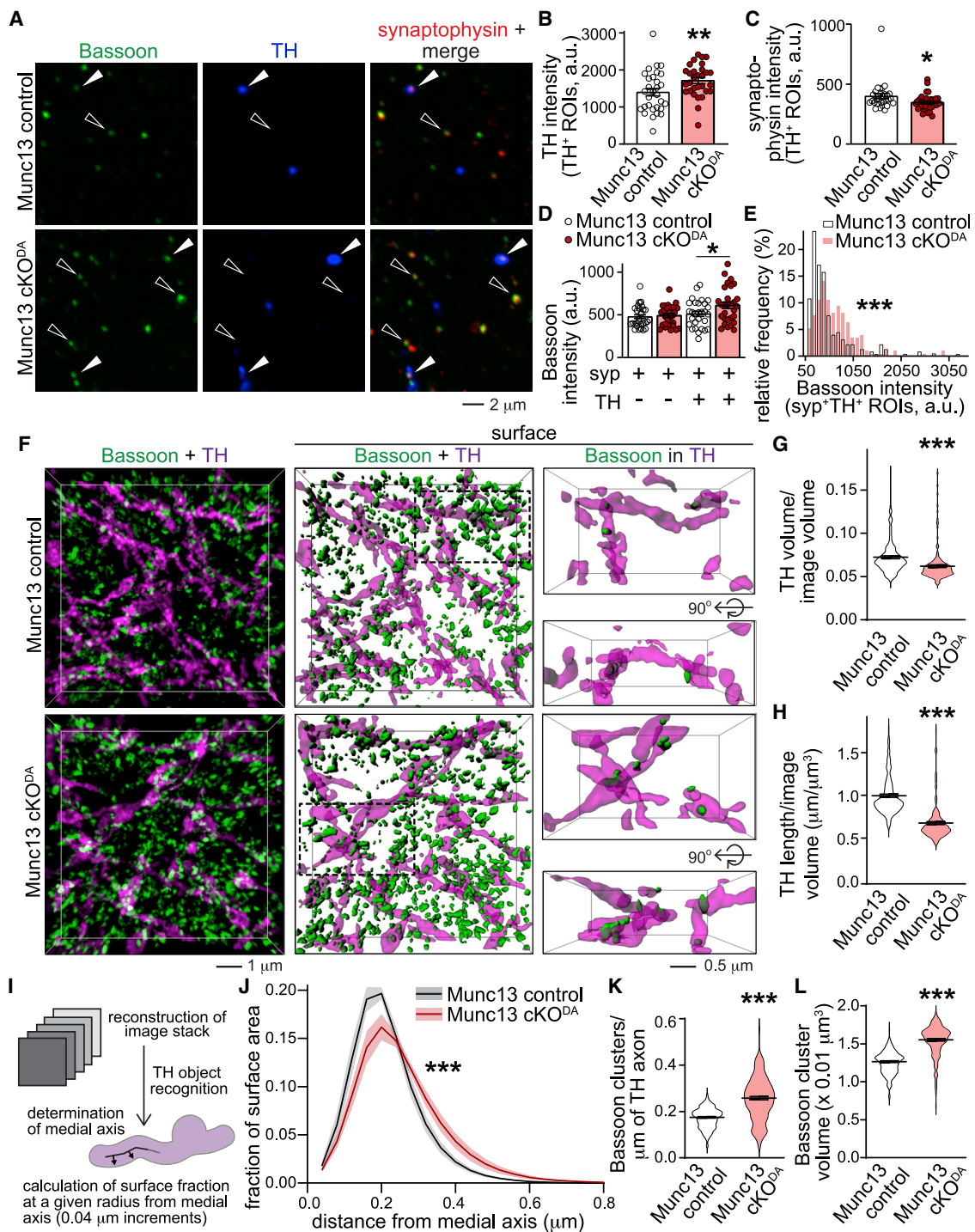


**Figure 5. Munc13 cKO<sup>DA</sup> affects dopamine axon structure and Bassoon clustering**

(A) Sample confocal images of striatal synaptosomes stained with the active zone marker Bassoon, the vesicle marker synaptophysin, and TH; synaptosomes co-expressing all three proteins (solid arrowheads) or non-dopaminergic synaptosomes (hollow arrowheads, no TH signal) are highlighted.

(B–E) Quantification of (A). (E) shows the frequency histogram for Bassoon intensity in syp<sup>+</sup>TH<sup>+</sup> ROIs; (B) and (C) 30 images/3 mice each; (D) syp<sup>+</sup>TH<sup>+</sup> 30/3 each, syp<sup>+</sup>TH<sup>−</sup> 29/3 each; (E) Munc13 control 221 ROIs/29 images/3 mice, Munc13 cKO<sup>DA</sup> 168/29/3.

(F) Sample 3D-SIM images (dimensions and overlap criteria as in Figure 2B) of dorsolateral striatum stained for Bassoon and TH.

(G–L) Quantification of (F) as in Figure 2. In (I) and (J), TH axon shape was assessed by determining the proportion of the axon surface at a specific distance from the medial axis of the TH-labeled axon, Munc13 control 163 images/4 mice; Munc13 cKO<sup>DA</sup> 165/4 (G, H, K, and L), 160/4 each (J).

Data are mean  $\pm$  SEM except for (J, mean  $\pm$  SD). \*p < 0.05, \*\*p < 0.01, and \*\*\*p < 0.001 as assessed using unpaired t tests in (B), (C), (G), (H), (K), and (L); one-way ANOVA followed by Sidak's multiple-comparisons tests in (D); Kolmogorov-Smirnov test in (E) and two-way ANOVA (\*\*\*) p < 0.001 for genotype, distance, and interaction) in (J). For additional morphological analyses, see Figure S5.

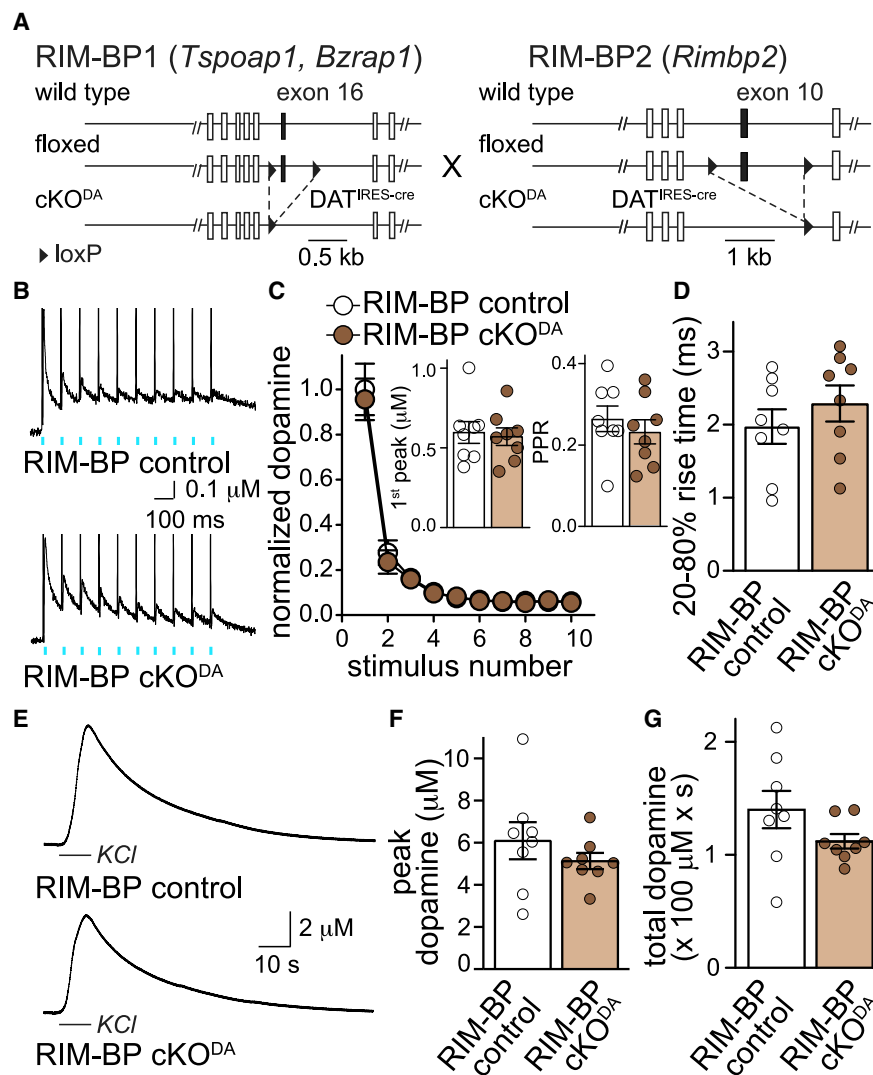


**Figure 6. RIM-BP is dispensable for dopamine release**

(A) Strategy for ablation of RIM-BP1 and RIM-BP2 in dopamine neurons (RIM-BP cKO<sup>DA</sup>).

(B–D) Sample traces of dopamine release (B, average of four sweeps) evoked by ten 1 ms light pulses at 10 Hz, quantification of amplitudes (C) normalized to the average of the first peak amplitude of RIM-BP control, peak amplitude evoked by the first stimulus and paired pulse ratios (PPR) of the second to the first stimulus (C, inset), and 20%–80% rise times (D), 8 slices/5 mice each.

(E–G) Sample traces (E), quantification of peak amplitudes (F), and area under the curve (G) in response to a KCl puff, 8/3 each.

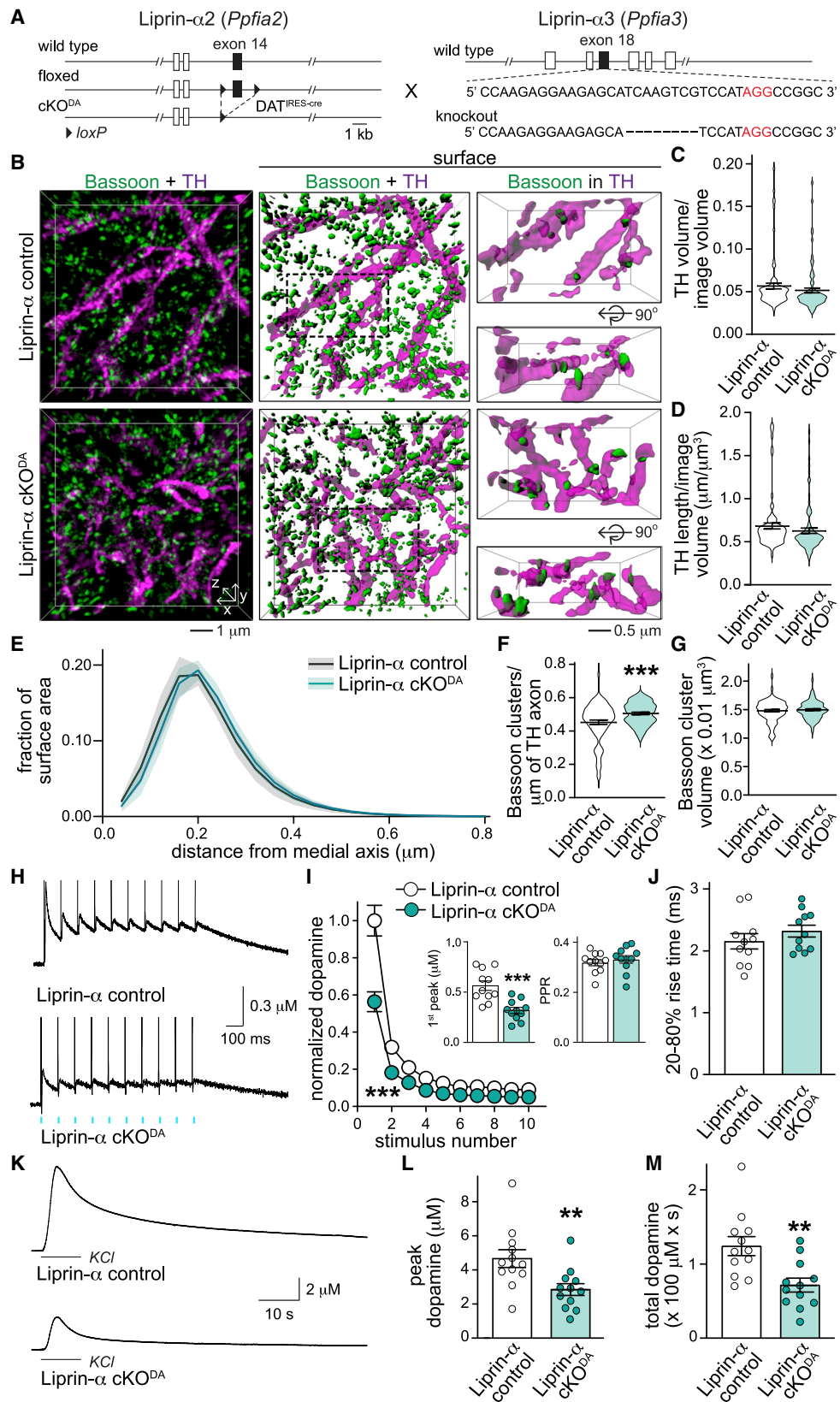
Data are mean  $\pm$  SEM. \*\*\* $p < 0.001$  as assessed using two-way ANOVA (\*\*\*) for stimulus number, not significant [n.s.] for genotype, interaction) followed by Sidak's multiple-comparisons tests in (C), and Mann-Whitney tests in (C, insets), (F), and (G). For electrical stimulation experiments, see Figure S6.

of RIM are likely important. RIM binds to Liprin- $\alpha$  with its C<sub>2</sub>B domain (Schoch et al., 2002). Liprin- $\alpha$  proteins are organizers of invertebrate active zones (Böhme et al., 2016; Patel and Shen, 2009; Zhen and Jin, 1999). Vertebrates express four Liprin- $\alpha$  genes (*Ppfia1–4*) to produce Liprin- $\alpha$ 1 through Liprin- $\alpha$ 4. Liprin- $\alpha$ 2 and Liprin- $\alpha$ 3 are strongly expressed in brain and localized to synapses, and brain Liprin- $\alpha$ 1 and Liprin- $\alpha$ 4 expression is generally low (Emperador-Melero et al., 2021a; Wong et al., 2018; Zürner et al., 2011).

We generated dopamine-neuron double-knockout mice for Liprin- $\alpha$ 2 and Liprin- $\alpha$ 3 (Liprin- $\alpha$  cKO<sup>DA</sup>; Figure 7A) by crossing floxed Liprin- $\alpha$ 2 mice to constitutive Liprin- $\alpha$ 3 knockouts and

DAT<sup>IRES-cre</sup> mice (Bäckman et al., 2006; Emperador-Melero et al., 2021a; Wong et al., 2018). We first probed for changes in dopamine axon structure. Apart from slightly increased Bassoon cluster densities, no morphological defects were detected (Figures 7B–7G).

Dopamine release induced by optogenetic activation was reduced by  $\sim$ 50% in Liprin- $\alpha$  cKO<sup>DA</sup> mice (Figures 7H–7J), while dopamine axon action potential firing was not detectably affected (Figures S7E–S7G). Release triggered by KCl was reduced as well (Figures 7K–7M). In contrast, release triggered by electrical stimulation, which strongly depends on nAChR receptor activation (Liu et al., 2018; Threlfell et al., 2012), appeared



(legend on next page)

unimpaired (Figures S7A–S7D). This could be because cholinergic interneuron function may be affected by constitutive Liprin- $\alpha$ 3 knockout, for example by enhancement of release probability as we recently described for excitatory hippocampal synapses after Liprin- $\alpha$ 2/3 ablation (Emperador-Melero et al., 2021a) or due to technical differences in the stimulation paradigm. Altogether, our data indicate important, albeit not essential, roles for Liprin- $\alpha$  in striatal dopamine release.

### Attaching the RIM C<sub>2</sub>B domain to the RIM zinc finger restores dopamine release

Our analyses suggest that RIM zinc finger domains prime dopamine vesicles through Munc13 (Figures 1, 2, 3, 4, and 5). C-terminal RIM C<sub>2</sub>B domain interactions with Liprin- $\alpha$  may mediate scaffolding (Figure 7). Interaction partners of the central RIM domains (e.g. ELKS and RIM-BP) appear less important (Figure 6; Liu et al., 2018). If true, dopamine release should be restored by the presence of the zinc finger domain to boost vesicle priming via Munc13 and the RIM C<sub>2</sub>B domain, which may support scaffolding via Liprin- $\alpha$  and PIP<sub>2</sub> (de Jong et al., 2018; Schoch et al., 2002). To test this, we compared three RIM rescue constructs (Figure 8A):

- (1) a RIM1-ZnC<sub>2</sub>B protein in which the zinc finger and C<sub>2</sub>B domains are connected with endogenous linker sequences that follow the RIM zinc finger;
- (2) a RIM1-ZnC<sub>2</sub>B<sup>KE</sup> protein, which is identical to RIM1-ZnC<sub>2</sub>B except for two point mutations (K1513E, K1515E) that disrupt the activity of C<sub>2</sub>B in release (de Jong et al., 2018); and
- (3) a RIM1-ZnPCP protein in which all RIM sequences (PDZ-C<sub>2</sub>A-PxxP) that are not present in RIM1-ZnC<sub>2</sub>B are fused to the zinc finger.

These rescue constructs were expressed in RIM cKO<sup>DA</sup> mice using cre-dependent AAVs, and expression was assessed using western blotting (Figure S8A). For each construct, we performed a comparison of its rescue activity to RIM cKO<sup>DA</sup> (RIM1-ZnC<sub>2</sub>B: Figures 8B, 8C, 8H, and 8I; RIM1-ZnC<sub>2</sub>B<sup>KE</sup>: Figures S8J–S8M; RIM1-ZnPCP: Figures 8F, 8G, 8L, and 8M), and we also directly compared RIM1-ZnC<sub>2</sub>B and RIM1-ZnC<sub>2</sub>B<sup>KE</sup> to one another (Figures 8D, 8E, 8J, and 8K).

Strikingly, RIM1-ZnC<sub>2</sub>B enhanced dopamine release evoked by electrical stimuli and KCl puffs over RIM cKO<sup>DA</sup> (Figures 8B, 8C, 8H, and 8I) as effectively as co-expression of RIM1-Zn and RIM1- $\Delta$ Zn (Figures 1L, 1M, 1R, 1S, S8N, and S8O). Inactivation of the C<sub>2</sub>B domain in this construct (RIM1-ZnC<sub>2</sub>B<sup>KE</sup>) or fusion of the other RIM domains to RIM1-Zn (RIM1-ZnPCP) disrupted the

ability to restore release evoked by electrical stimulation (Figures 8D–8G, S8J, and S8K). All three constructs partially restored KCl-triggered release (Figures 8H–8M, S8L, and S8M), similar to co-expression of RIM1-Zn and RIM1- $\Delta$ Zn (Figures 1L, 1M, 1R, and 1S). We compared rescue activity of all experiments through normalization against the average of all control recordings (Figures S8N and S8O). This comparison revealed that RIM1-ZnC<sub>2</sub>B or RIM1-Zn + RIM1- $\Delta$ Zn both restore action potential evoked release, while fusion of any other tested domain to RIM1-Zn supports KCl-triggered release. It is noteworthy that altogether, rescue is incomplete, with a maximum rescue of ~30%–40% compared with unrelated control mice (Figures S8N and S8O). This could be due to a combination of factors, including that rescue constructs may not be expressed in all dopamine neurons, that full-length RIM may be required, or that the RIM cKO<sup>DA</sup> phenotype may not be fully reversible. Currently, AAV capacity limits prevent efficient expression of full-length RIM and co-expression of optogenetic actuators in the same neurons. Hence, our conclusions should rely on comparing the various rescue conditions with one another in their activity over RIM cKO<sup>DA</sup>.

We propose that RIM-C<sub>2</sub>B domains enable scaffolding of the RIM zinc finger to release sites to restore action potential-triggered dopamine release (Figure 8N). The zinc finger and C<sub>2</sub>B domains appear sufficient to mediate the minimally needed release site functions, suggesting strikingly limited molecular requirements for dopamine release. Release triggered by KCl may represent a measure of vesicle fusogenicity. The strong stimulus may partially override the need for vesicle tethering close to Ca<sup>2+</sup> entry and does not require the C<sub>2</sub>B domain.

## DISCUSSION

Despite central roles for striatal dopamine in circuit regulation and behavior, there remain major gaps in the understanding of the molecular and functional organization of its release. Dopamine release requires the active zone protein RIM (Liu et al., 2018; Robinson et al., 2019), but components or mechanisms of active zone-like release sites beyond this requirement were essentially unknown. Here, we found that Munc13 is essential for dopamine release, and we propose that RIM and Munc13 cooperate to promote dopamine vesicle priming (Figures 1, 2, 3, 4, and 5). The scaffolding mechanisms that organize dopamine release sites appear quite simple compared with classical synapses (Figures 1, 6, 7, and 8). The active zone scaffolds RIM-BP (Figure 6) and ELKS (Liu et al., 2018) are dispensable

### Figure 7. Liprin- $\alpha$ is important for dopamine release

(A) Strategy for ablation of Liprin- $\alpha$ 2 and Liprin- $\alpha$ 3 (Liprin- $\alpha$  cKO<sup>DA</sup>).  
 (B) Sample 3D-SIM images (dimensions and overlap criteria as in Figure 2B) of dorsolateral striatum stained for Bassoon and TH.  
 (C–G) Quantification of (B) as in Figures 5G–5L; Liprin- $\alpha$  control 84 images/4 mice; Liprin- $\alpha$  cKO<sup>DA</sup> 85/4.  
 (H–J) Sample traces of dopamine release (H, average of four sweeps) evoked by ten 1 ms light pulses at 10 Hz and quantification of amplitudes (I) normalized to the average of the first peak amplitude of RIM-BP control, first stimulus peak amplitude and PPR (I, insets), and 20%–80% rise times (J), 11 slices/4 mice each.  
 (K–M) Sample traces (K), quantification of peak amplitudes (L), and area under the curve (M) in response to a KCl puff, 12/8 each.  
 Data are mean  $\pm$  SEM, except for (E, mean  $\pm$  SD). \*\*p < 0.01 and \*\*\*p < 0.001 as assessed using unpaired t tests in (C), (D), (F), and (G); two-way ANOVA (\*\*p < 0.001 for distance and interaction, n.s. for genotype) in (E); two-way ANOVA (\*\*p < 0.001 for genotype, stimulus number, and interaction) followed by Sidak's multiple-comparisons tests in (I, \*\*\*p < 0.001 for first and second stimuli), Mann-Whitney tests in (I, insets), (J), (L), and (M). For additional Liprin- $\alpha$  cKO<sup>DA</sup> analyses, see Figure S7.

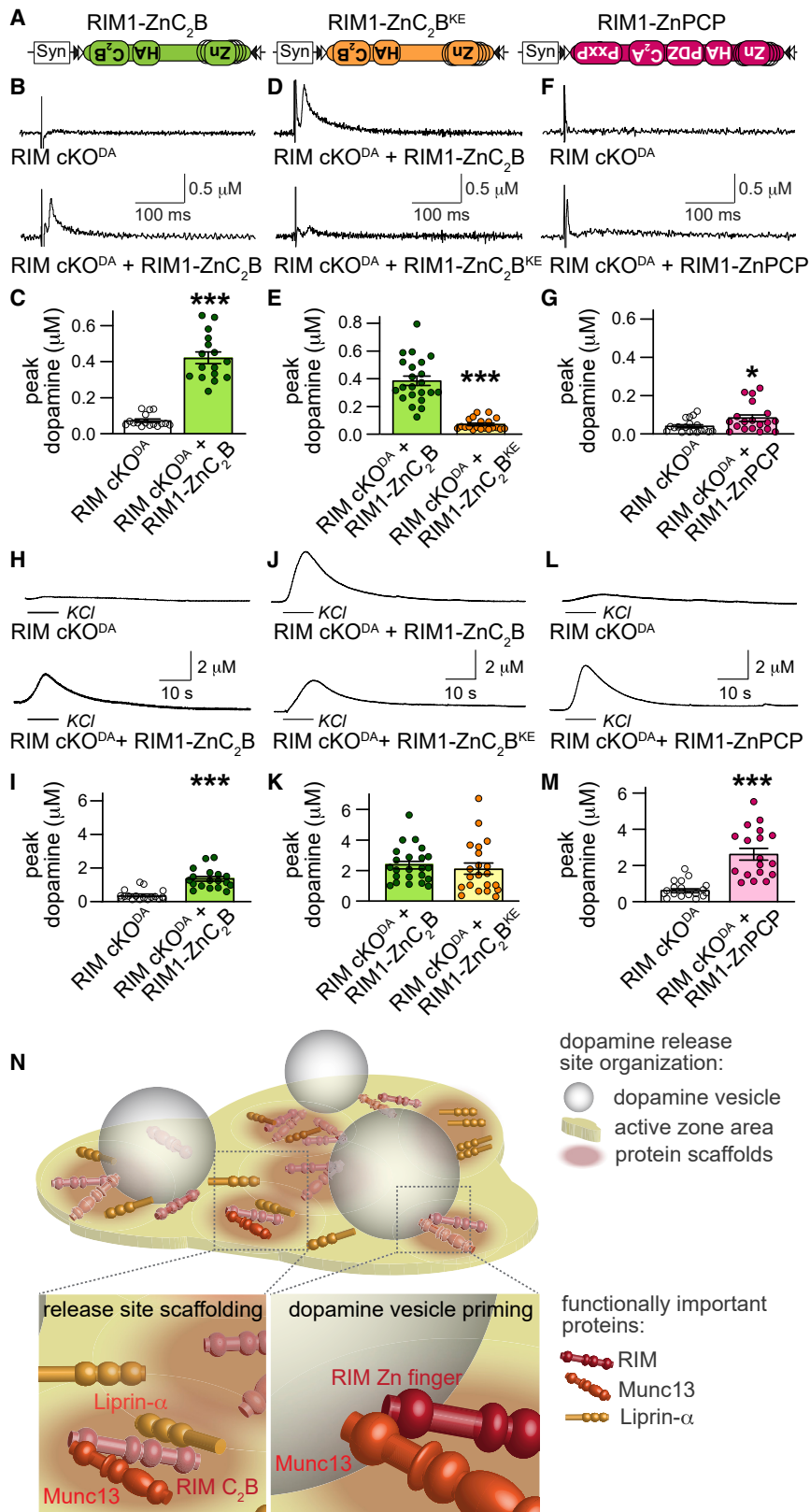


**Figure 8. RIM C<sub>2</sub>B domains are important for evoked dopamine release**

(A) Schematic of AAV5 viruses injected into the midbrain for cre-dependent expression of rescue proteins.

(B-G) Sample traces (B, D, and F, single sweeps) and quantification (C, E, and G) of dopamine release evoked by a 90  $\mu$ A electrical stimulus; (C) 16 slices/4 mice each; (E) RIM cKO<sup>DA</sup> + RIM1-ZnC<sub>2</sub>B 22/5, RIM cKO<sup>DA</sup> + RIM1-ZnC<sub>2</sub>B<sup>KE</sup> 20/5; (G) 19/4 each.

(H-M) Same as (B)-(G), but for a local 100 mM puff of KCl; (I) 18/4 each; (K) RIM cKO<sup>DA</sup> + RIM1-ZnC<sub>2</sub>B 23/5, RIM cKO<sup>DA</sup> + RIM1-ZnC<sub>2</sub>B<sup>KE</sup> 21/5; (M) 18/4 each.

(N) Model of an active zone-like site in the dorsal striatum. RIM, Munc13, and Liprin- $\alpha$  form release sites in dopamine varicosities, with Munc13 and RIM mediating dopamine vesicle priming and all three proteins contributing to scaffolding.

Data are mean  $\pm$  SEM. \* $p < 0.05$  and \*\*\* $p < 0.001$  as assessed using Mann-Whitney tests in (C), (E), (G), (I), (K), and (M). For control recordings, additional rescue, and comparisons of all rescue experiments, see Figure S8.

for dopamine release, while Liprin- $\alpha$ 2 and Liprin- $\alpha$ 3 knockout has more pronounced effects on dopamine release (Figure 7) than at hippocampal synapses (Emperador-Melero et al., 2021a). The C-terminal RIM C<sub>2</sub>B domain is important for dopamine release and may contribute through binding of Liprin- $\alpha$  and/or PIP<sub>2</sub> (Figures 1, 7, and 8). Our data lead to a model (Figure 8N) in which RIM and Munc13 mediate vesicle priming and operate together with Liprin- $\alpha$  for rapid and precise release.

### Does Munc13 prime dopamine vesicles for fast release?

Fast neurotransmitter release relies on vesicle priming, which prepares vesicles and plasma membranes for exocytosis and involves vesicle attachment to the target membrane (Imig et al., 2014; Kaeser and Regehr, 2017). At fast synapses, RIM recruits Munc13 to active zones and activates it, and Munc13 controls the assembly of SNARE complexes (Andrews-Zwilling et al., 2006; Betz et al., 2001; Camacho et al., 2017; Deng et al., 2011; Imig et al., 2014; Ma et al., 2013; Varoqueaux et al., 2002). For the release of modulatory transmitters, the priming mechanisms are less well understood. In some cases, they rely less on Munc13 and instead may use alternative or additional priming pathways (Berwin et al., 1998; van de Bospoort et al., 2012; van Keimpema et al., 2017; Man et al., 2015; Renden et al., 2001). The observations that action potential-triggered dopamine release requires RIM and Munc13 and is mediated by RIM zinc finger domains indicate that striatal dopamine axons employ priming mechanisms similar to conventional synapses. These findings support the overall model of fast and efficient dopamine secretion (Liu et al., 2018, 2021).

Munc13 cKO<sup>DA</sup> mice have altered dopamine axon and release site structure. This is unanticipated because previous studies found normal synapse assembly in the absence of Munc13 (Augustin et al., 1999; Sigler et al., 2017; Varoqueaux et al., 2002), synaptic vesicle exocytosis (Verhage et al., 2000), or presynaptic Ca<sup>2+</sup> entry (Held et al., 2020). Furthermore, strong impairments in action potential-triggered dopamine secretion by ablation of synaptotagmin-1 (Banerjee et al., 2020) or RIM (Liu et al., 2018) do not lead to similarly prominent phenotypes. Hence, dopamine axon alterations are unlikely caused by loss of dopamine secretion, but Munc13 may have independent roles in dopamine axon structure. These effects may be similar to a previously described role of Munc13 in the delay of growth rates of neurites in dissociated and organotypic slice cultures (Broeke et al., 2010). In our experiments, these roles could arise from cell-autonomous Munc13 functions or could be mediated by knockout of Munc13-2 and Munc13-3 in surrounding cells, for example through loss of secretion of modulatory substances important for growth. Roles in release site assembly, observed here as altered Bassoon clustering, have also been described in the fly neuromuscular junction and in cultured hippocampal neurons, where Munc13 controls the clustering of Brp or syntaxin, respectively (Böhme et al., 2016; Sakamoto et al., 2018). Hence, release site scaffolding may be a Munc13 function that is shared across several secretory systems.

### Functional organization of active zone-like dopamine release sites

Initial observations suggested that RIM organizes active zone-like release sites (Liu et al., 2018). However, it remained unclear

whether RIM operates as a release site scaffold or as a soluble or vesicle-associated release factor. We found that RIM C<sub>2</sub>B domains are important, supporting the model of a scaffolded site. At classical synapses, active zone scaffolding mechanisms support three fundamental requirements: (1) they tether Ca<sup>2+</sup> channels to release sites, (2) they dock vesicles to exocytotic sites, and (3) they mediate the attachment and positioning of release machinery at the correct place in the target membrane. How are these functions executed to support striatal dopamine release?

For synaptic secretion, Ca<sup>2+</sup> channel tethering (1) is mediated by RIMs and RIM-BPs (Hibino et al., 2002; Kaeser et al., 2011; Wu et al., 2019). Several observations suggest that Ca<sup>2+</sup> secretion coupling in the dopamine system does not strongly rely on this synaptic protein complex. First, dopamine release is dependent on multiple Ca<sub>v</sub>s, including Ca<sub>v</sub>1, Ca<sub>v</sub>2, and Ca<sub>v</sub>3 (Brimblecombe et al., 2015; Liu and Kaeser, 2019), and mechanisms that rely on RIM-Ca<sub>v</sub> interactions unlikely explain the localization of channels other than Ca<sub>v</sub>2s (Kaeser et al., 2011). Second, although RIM-BP may organize channels other than Ca<sub>v</sub>2s (Hibino et al., 2002), RIM-BP1 and RIM-BP2 are dispensable for dopamine release. Third, at synapses where RIM organizes Ca<sub>v</sub>2s, the presence of high extracellular Ca<sup>2+</sup> overrides the need for RIM (Kaeser et al., 2011, 2012), but this is not the case for striatal dopamine release (Liu et al., 2018). Finally, RIM-containing dopamine release sites are sparse, but Ca<sup>2+</sup> entry appears to be present in all varicosities (Liu et al., 2018; Pereira et al., 2016). Together, these observations suggest that the RIM/RIM-BP complex is not the major or only organizer of Ca<sup>2+</sup> channel complexes in dopamine axons. What other mechanisms could contribute? One possibility is that Ca<sub>v</sub>s are organized through transmembrane proteins rather than active zone complexes, for example by neuroligins, which organize Ca<sub>v</sub>s and may drive synapse formation in cultured dopamine neurons (Ducrot et al., 2021; Luo et al., 2020). Another possibility is that  $\alpha$ 2 $\delta$  proteins or  $\beta$  subunits drive positioning of various Ca<sub>v</sub>s in dopamine neurons, which could explain why subtype-specific positioning mechanism are dispensable (Held et al., 2020; Hoppa et al., 2012). While our data indicate that dopamine release does not build upon the classical Ca<sup>2+</sup> secretion coupling mechanisms, future studies should address how Ca<sup>2+</sup> entry and its coupling to release-ready vesicles are organized in the dopamine system.

Tethering and docking of vesicles (2) is likely important given the rapidity of dopamine release. At classical synapses, RIM and Munc13 mediate vesicle docking (Han et al., 2011; Imig et al., 2014; Kaeser et al., 2011; Wang et al., 2016; Wong et al., 2018). Technical limitations have prevented tests of vesicle docking in the dopamine system. Assessment of docking requires high pressure freezing rather than chemical fixation, which is difficult to adapt and optimize for acute brain slices from different brain regions, and, more important, dopamine-releasing varicosities are very sparse and difficult to identify. However, fast kinetics, high release probability, and Munc13 and RIM dependence support that dopamine vesicle docking is mediated by classical, synaptic mechanisms. Alternative or complementary attachment could be mediated by phospholipid interactions, for example between PIP<sub>2</sub> and synaptotagmin-1

(Chang et al., 2018; Jahn and Fasshauer, 2012). One interesting possibility is that both  $\text{Ca}^{2+}$  entry and vesicle-target membrane tethering, for example via synaptotagmin-1, are present in all dopamine varicosities (Banerjee et al., 2020; Pereira et al., 2016), but that priming for release only occurs in active zone-containing varicosities (Liu et al., 2018; Pereira et al., 2016). This may explain why some varicosities remain silent upon stimulation despite the presence of vesicles.

Target membrane attachment and positioning of release machinery (3) is poorly understood (Emperador-Melero and Kaeser, 2020). Proposed mechanisms at synapses include interactions with transmembrane proteins or target membrane phospholipids. However, strong active zone assembly phenotypes have not been reported upon disruption of any specific mechanism, for example, abolishing binding to  $\text{PIP}_2$ , or knocking out of Cav2s, LAR-PTPs or neuroligins (Chen et al., 2017; Emperador-Melero et al., 2021b; Held et al., 2020; de Jong et al., 2018; Scлип and Südhof, 2020). Given the dopamine secretory deficits in Liprin- $\alpha$  cKO<sup>DA</sup> mice (Figure 6), Liprin- $\alpha$  binding to LAR-PTPs (Serra-Pagès et al., 1995, 1998) and the dependence of dopamine release on RIM C<sub>2</sub>B domains (which bind to Liprin- $\alpha$  and  $\text{PIP}_2$ ), the most parsimonious working model is that RIM C<sub>2</sub>B domains provide a key tethering mechanism at dopamine release sites. For glutamatergic transmission, secretory hotspots are strategically assembled opposed to postsynaptic receptor nanodomains (Biederer et al., 2017; Tang et al., 2016). This model is interesting to assess for the dopamine system, in which most varicosities are not associated with target cells through a synaptic organization (Descarries et al., 1996). One possibility is that release site localization is independent of dopamine receptor domains. An alternative model is that the small fraction of dopamine varicosities that is associated with postsynaptic cells (Descarries et al., 1996; Uchigashima et al., 2016) relies on transsynaptic organization, and only varicosities with this synaptic organization contain active zones for dopamine release. Recent work favors the former model, because both synaptic and non-synaptic varicosities have release capacity (Ducrot et al., 2021; Liu et al., 2021). Future work should address the relationship between dopamine receptors and the active zone-like release sites that we describe here.

Overall, our findings establish that dopamine release sites have evolved to be fast and efficient. Scaffolding appears less complex than at classical synapses, on the basis of three lines of evidence. First, functional effects of RIM deletion are stronger than at regular synapses (de Jong et al., 2018; Kaeser et al., 2011; Liu et al., 2018). Second, the scaffolds ELKS (Liu et al., 2018) and RIM-BP (Figure 6) are dispensable for dopamine release. Third, the RIM C-terminal domains are important scaffolds of dopamine release machinery (Figures 1 and 8), and Munc13 has scaffolding roles as well (Figure 5), but at conventional synapses, these structural roles are largely dispensable (Augustin et al., 1999; Deng et al., 2011; Han et al., 2011; Kaeser et al., 2011; Sigler et al., 2017; Varoqueaux et al., 2002), indicating more redundancy. Hence, dopamine release site architecture appears different from prototypical synapses and relies on simple, streamlined scaffolding mechanisms. Finally, our work supports a growing body of literature on release site diversity across transmitter systems and neuron

subtypes (Brockmann et al., 2019; Emperador-Melero et al., 2021a; Held et al., 2016). Our findings on RIM, Munc13, and Liprin- $\alpha$  may be relevant for understanding the organization of release machinery at specific classical synapses or in other neuromodulatory systems as well.

## STAR★METHODS

Detailed methods are provided in the online version of this paper and include the following:

- KEY RESOURCES TABLE
- RESOURCE AVAILABILITY
  - Lead contact
  - Materials availability
  - Data and code availability
- EXPERIMENTAL MODEL AND SUBJECT DETAILS
- METHOD DETAILS
  - Rescue constructs and production of AAV viruses
  - Stereotaxic surgery
  - Electrophysiology in brain slices
  - Immunostaining of brain sections
  - 3D-SIM image acquisition and analysis
  - Generation of conditional Munc13-1 knockout mice
  - Immunoblotting
  - Generation of autaptic mouse hippocampal neuron cultures
  - Electrophysiology on neurons in autaptic hippocampal cultures
  - Microdialysis
  - Striatal synaptosome preparation and immunostaining
  - Confocal microscopy and image analysis of striatal synaptosomes
- QUANTIFICATION AND STATISTICAL ANALYSIS

## SUPPLEMENTAL INFORMATION

Supplemental information can be found online at <https://doi.org/10.1016/j.neuron.2021.10.028>.

## ACKNOWLEDGMENTS

This work was supported by the National Institutes of Health (R01NS103484 and R01MH113349 to P.S.K.; F31NS105159 to L.K.), the Dean's Initiative Award for Innovation (P.S.K.), a Harvard-MIT Joint Research Grant (P.S.K.), a William Randolph Hearst fellowship (A.B.), an Alice Joseph Brooks fellowship (A.B.), a Mahoney fellowship (A.B.), a Gordon family fellowship (C.L.), the European Commission (European Research Council [ERC] Advanced Grant Syn-Prime to N.B.), and Germany's Excellence Strategy (EXC 2067/1-390729940 to N.B.). X.C. is a visiting graduate student and was in part supported by a PhD Mobility National Grants fellowship from the China Scholarship Council/Xi'an Jiaotong University. We thank C. Qiao, M. Han, A. Zeuch, A. Günther, and S. Beuermann for technical assistance and T.C. Südhof for the floxed RIM-BP mice. We acknowledge the HMS Neurobiology Imaging Facility (supported by P30NS072030) and the HMS Cell Biology Microscopy Facility for availability of microscopes and advice, T. Lambert for help with 3D-SIM, M. Cicconet and the HMS Image and Data Analysis Core for help with developing TH axon analyses, the MPI-EM DNA Core Facility for mouse genotyping, the MPI-EM and HMS animal facilities for mouse husbandry, and U. Fünfschilling and M. Schindler for blastocyst injections.

## AUTHOR CONTRIBUTIONS

Conceptualization, A.B. and P.S.K.; Methodology, A.B., C.I., K.B., L.K., N.L., R.-L.U., J.W., X.C., F.B., J.S.R., B.H.C., C.L., and S.M.W.; Formal Analysis, A.B., C.I., K.B., L.K., N.L., J.S.R., B.H.C., C.L., S.M.W., N.B., and P.S.K.; Investigation, A.B., C.I., K.B., L.K., N.L., R.-L.U., J.S.R., B.H.C., and C.L.; Resources, A.B., C.I., K.B., J.W., X.C., F.B., S.M.W., N.B., and P.S.K.; Writing – Original Draft, A.B., C.I., and P.S.K.; Writing – Review & Editing, A.B., C.I., K.B., L.K., N.L., C.L., N.B., and P.S.K.; Supervision, J.S.R., C.L., S.M.W., N.B., and P.S.K.; Funding Acquisition, N.B. and P.S.K.

## DECLARATION OF INTERESTS

The authors declare no competing interests. L.K. is currently an employee of Precisient Healthcare Group (Jersey City, NJ). R.-L.U. is currently an employee of Medafcon Oy (Espoo, Finland). X.C. is a visiting graduate student from Xi'an Jiaotong University (China). N.B. is a member of the *Neuron* Advisory Board.

Received: December 19, 2020

Revised: September 22, 2021

Accepted: October 19, 2021

Published: November 11, 2021

## REFERENCES

- Acuna, C., Liu, X., Gonzalez, A., and Südhof, T.C. (2015). RIM-BPs mediate tight coupling of action potentials to Ca<sup>2+</sup>-triggered neurotransmitter release. *Neuron* 87, 1234–1247.
- Acuna, C., Liu, X., and Südhof, T.C. (2016). How to make an active zone: unexpected universal functional redundancy between RIMs and RIM-BPs. *Neuron* 91, 792–807.
- Adams, D.J., Quail, M.A., Cox, T., van der Weyden, L., Gorick, B.D., Su, Q., Chan, W.I., Davies, R., Bonfield, J.K., Law, F., et al. (2005). A genome-wide, end-sequenced 129Sv BAC library resource for targeting vector construction. *Genomics* 86, 753–758.
- Agnati, L.F., Zoli, M., Strömberg, I., and Fuxe, K. (1995). Intercellular communication in the brain: wiring versus volume transmission. *Neuroscience* 69, 711–726.
- Andrews-Zwilling, Y.S., Kawabe, H., Reim, K., Varoqueaux, F., and Brose, N. (2006). Binding to Rab3A-interacting molecule RIM regulates the presynaptic recruitment of Munc13-1 and ubMunc13-2. *J. Biol. Chem.* 281, 19720–19731.
- Augustin, I., Rosenmund, C., Südhof, T.C., and Brose, N. (1999). Munc13-1 is essential for fusion competence of glutamatergic synaptic vesicles. *Nature* 400, 457–461.
- Augustin, I., Korte, S., Rickmann, M., Kretschmar, H.A., Südhof, T.C., Herms, J.W., and Brose, N. (2001). The cerebellum-specific Munc13 isoform Munc13-3 regulates cerebellar synaptic transmission and motor learning in mice. *J. Neurosci.* 21, 10–17.
- Bäckman, C.M., Malik, N., Zhang, Y., Shan, L., Grinberg, A., Hoffer, B.J., Westphal, H., and Tomac, A.C. (2006). Characterization of a mouse strain expressing Cre recombinase from the 3' untranslated region of the dopamine transporter locus. *Genesis* 44, 383–390.
- Banerjee, A., Lee, J., Nemcova, P., Liu, C., and Kaeser, P.S. (2020). Synaptotagmin-1 is the Ca<sup>2+</sup> sensor for fast striatal dopamine release. *eLife* 9, e58359.
- Beckstead, M.J., Grandy, D.K., Wickman, K., and Williams, J.T. (2004). Vesicular dopamine release elicits an inhibitory postsynaptic current in midbrain dopamine neurons. *Neuron* 42, 939–946.
- Berwin, B., Floor, E., and Martin, T.F. (1998). CAPS (mammalian UNC-31) protein localizes to membranes involved in dense-core vesicle exocytosis. *Neuron* 21, 137–145.
- Betz, A., Okamoto, M., Benseler, F., and Brose, N. (1997). Direct interaction of the rat unc-13 homologue Munc13-1 with the N terminus of syntaxin. *J. Biol. Chem.* 272, 2520–2526.
- Betz, A., Ashery, U., Rickmann, M., Augustin, I., Neher, E., Südhof, T.C., Rettig, J., and Brose, N. (1998). Munc13-1 is a presynaptic phorbol ester receptor that enhances neurotransmitter release. *Neuron* 21, 123–136.
- Betz, A., Thakur, P., Junge, H.J., Ashery, U., Rhee, J.S., Scheuss, V., Rosenmund, C., Rettig, J., and Brose, N. (2001). Functional interaction of the active zone proteins Munc13-1 and RIM1 in synaptic vesicle priming. *Neuron* 30, 183–196.
- Biederer, T., Kaeser, P.S., and Blanpied, T.A. (2017). Transcellular nanoalignment of synaptic function. *Neuron* 96, 680–696.
- Böhme, M.A., Beis, C., Reddy-Alla, S., Reynolds, E., Mampell, M.M., Grasskamp, A.T., Lützkendorf, J., Bergeron, D.D., Driller, J.H., Babikir, H., et al. (2016). Active zone scaffolds differentially accumulate Unc13 isoforms to tune Ca<sup>2+</sup> channel-vesicle coupling. *Nat. Neurosci.* 19, 1311–1320.
- Brimblecombe, K.R., Gracie, C.J., Platt, N.J., and Cragg, S.J. (2015). Gating of dopamine transmission by calcium and axonal N-, Q-, T- and L-type voltage-gated calcium channels differs between striatal domains. *J. Physiol.* 593, 929–946.
- Brockmann, M.M., Maglione, M., Willmes, C.G., Stumpf, A., Bouazza, B.A., Velasquez, L.M., Grauel, M.K., Beed, P., Lehmann, M., Gimber, N., et al. (2019). RIM-BP2 primes synaptic vesicles via recruitment of Munc13-1 at hippocampal mossy fiber synapses. *eLife* 8, e43243.
- Broeke, J.H.P., Roelandse, M., Luteijn, M.J., Boiko, T., Matus, A., Toonen, R.F., and Verhage, M. (2010). Munc18 and Munc13 regulate early neurite outgrowth. *Biol. Cell* 102, 479–488.
- Burgalossi, A., Jung, S., Man, K.N., Nair, R., Jockusch, W.J., Wojcik, S.M., Brose, N., and Rhee, J.-S. (2012). Analysis of neurotransmitter release mechanisms by photolysis of caged Ca<sup>2+</sup> in an autaptic neuron culture system. *Nat. Protoc.* 7, 1351–1365.
- Cachope, R., Mateo, Y., Mathur, B.N., Irving, J., Wang, H.-L., Morales, M., Lovinger, D.M., and Cheer, J.F. (2012). Selective activation of cholinergic interneurons enhances accumbal phasic dopamine release: setting the tone for reward processing. *Cell Rep.* 2, 33–41.
- Camacho, M., Basu, J., Trimbuch, T., Chang, S., Pulido-Lozano, C., Chang, S.-S., Duluvova, I., Abo-Rady, M., Rizo, J., and Rosenmund, C. (2017). Heterodimerization of Munc13 C<sub>2</sub>A domain with RIM regulates synaptic vesicle docking and priming. *Nat. Commun.* 8, 15293.
- Chang, S., Trimbuch, T., and Rosenmund, C. (2018). Synaptotagmin-1 drives synchronous Ca<sup>2+</sup>-triggered fusion by C<sub>2</sub>B-domain-mediated synaptic-vesicle-membrane attachment. *Nat. Neurosci.* 21, 33–40.
- Chen, L.Y., Jiang, M., Zhang, B., Gokce, O., and Südhof, T.C. (2017). Conditional deletion of all neurexins defines diversity of essential synaptic organizer functions for neurexins. *Neuron* 94, 611–625.e4.
- Cooper, B., Hemmerlein, M., Ammermüller, J., Imig, C., Reim, K., Lipstein, N., Kalla, S., Kawabe, H., Brose, N., Brandstätter, J.H., and Varoqueaux, F. (2012). Munc13-independent vesicle priming at mouse photoreceptor ribbon synapses. *J. Neurosci.* 32, 8040–8052.
- Courtney, N.A., and Ford, C.P. (2014). The timing of dopamine- and noradrenaline-mediated transmission reflects underlying differences in the extent of spillover and pooling. *J. Neurosci.* 34, 7645–7656.
- Daniel, J.A., Galbraith, S., Iacovitti, L., Abdipranoto, A., and Vissel, B. (2009). Functional heterogeneity at dopamine release sites. *J. Neurosci.* 29, 14670–14680.
- de Jong, A.P.H., Roggero, C.M., Ho, M.-R., Wong, M.Y., Brautigam, C.A., Rizo, J., and Kaeser, P.S. (2018). RIM C<sub>2</sub>B domains target presynaptic active zone functions to PIP<sub>2</sub>-containing membranes. *Neuron* 98, 335–349.e7.
- Deng, L., Kaeser, P.S., Xu, W., and Südhof, T.C. (2011). RIM proteins activate vesicle priming by reversing autoinhibitory homodimerization of Munc13. *Neuron* 69, 317–331.
- Descarries, L., Watkins, K.C., Garcia, S., Bosler, O., and Doucet, G. (1996). Dual character, asynchronous and synaptic, of the dopamine innervation in adult rat neostriatum: a quantitative autoradiographic and immunocytochemical analysis. *J. Comp. Neurol.* 375, 167–186.



- Di Paolo, G., and De Camilli, P. (2006). Phosphoinositides in cell regulation and membrane dynamics. *Nature* 443, 651–657.
- Ducrot, C., Bourque, M.-J., Delmas, C.V.L., Racine, A.-S., Guadarrama Bello, D., Delignat-Lavaud, B., Domenic Lycas, M., Fallon, A., Michaud-Tardif, C., Burke Nanni, S., et al. (2021). Dopaminergic neurons establish a distinctive axonal arbor with a majority of non-synaptic terminals. *FASEB J.* 35, e21791.
- Emperador-Melero, J., and Kaeser, P.S. (2020). Assembly of the presynaptic active zone. *Curr. Opin. Neurobiol.* 63, 95–103.
- Emperador-Melero, J., Wong, M.Y., Wang, S.S.H., de Nola, G., Nyitrai, H., Kirchhausen, T., and Kaeser, P.S. (2021a). PKC-phosphorylation of Liprin- $\alpha$ 3 triggers phase separation and controls presynaptic active zone structure. *Nat. Commun.* 12, 3057.
- Emperador-Melero, J., de Nola, G., and Kaeser, P.S. (2021b). Intact synapse structure and function after combined knockout of PTP $\delta$ , PTP $\sigma$  and LAR. *eLife* 10, e66638.
- Farina, M., van de Bospoort, R., He, E., Persoon, C.M., van Weering, J.R.T., Broeke, J.H., Verhage, M., and Toonen, R.F. (2015). CAPS-1 promotes fusion competence of stationary dense-core vesicles in presynaptic terminals of mammalian neurons. *eLife* 4, e05438.
- Farley, F.W., Soriano, P., Steffen, L.S., and Dymecki, S.M. (2000). Widespread recombinase expression using FLP $\alpha$  (flipper) mice. *Genesis* 28, 106–110.
- Gantz, S.C., Ford, C.P., Morikawa, H., and Williams, J.T. (2018). The evolving understanding of dopamine neurons in the substantia nigra and ventral tegmental area. *Annu. Rev. Physiol.* 80, 219–241.
- Giorgiuffi, M.F., Le Floc'h, M.L., Westfall, T.C., Glowinski, J., and Besson, M.J. (1976). Nicotinic effect of acetylcholine on the release of newly synthesized (3H) dopamine in rat striatal slices and cat caudate nucleus. *Brain Res.* 106, 117–131.
- Gustafsson, M.G.L., Shao, L., Carlton, P.M., Wang, C.J.R., Golubovskaya, I.N., Cande, W.Z., Agard, D.A., and Sedat, J.W. (2008). Three-dimensional resolution doubling in wide-field fluorescence microscopy by structured illumination. *Biophys. J.* 94, 4957–4970.
- Han, Y., Kaeser, P.S., Südhof, T.C., and Schneggenburger, R. (2011). RIM determines Ca<sup>2+</sup> channel density and vesicle docking at the presynaptic active zone. *Neuron* 69, 304–316.
- Held, R.G., and Kaeser, P.S. (2018). ELKS active zone proteins as multitasking scaffolds for secretion. *Open Biol.* 8, 170258.
- Held, R.G., Liu, C., and Kaeser, P.S. (2016). ELKS controls the pool of readily releasable vesicles at excitatory synapses through its N-terminal coiled-coil domains. *eLife* 5, e14862.
- Held, R.G., Liu, C., Ma, K., Ramsey, A.M., Tarr, T.B., De Nola, G., Wang, S.S.H., Wang, J., van den Maagdenberg, A.M.J.M., Schneider, T., et al. (2020). Synapse and active zone assembly in the absence of presynaptic Ca<sup>2+</sup> channels and Ca<sup>2+</sup> entry. *Neuron* 107, 667–683.e9.
- Hibino, H., Pironkova, R., Onwumere, O., Vologodskaja, M., Hudspeth, A.J., and Lesage, F. (2002). RIM binding proteins (RBPs) couple Rab3-interacting molecules (RIMs) to voltage-gated Ca(2+) channels. *Neuron* 34, 411–423.
- Honigsmann, A., van den Bogaart, G., Iraheta, E., Risselada, H.J., Milovanovic, D., Mueller, V., Müller, S., Diederichsen, U., Fasshauer, D., Grubmüller, H., et al. (2013). Phosphatidylinositol 4,5-bisphosphate clusters act as molecular beacons for vesicle recruitment. *Nat. Struct. Mol. Biol.* 20, 679–686.
- Hooper, M., Hardy, K., Handyside, A., Hunter, S., and Monk, M. (1987). HPRT-deficient (Lesch-Nyhan) mouse embryos derived from germline colonization by cultured cells. *Nature* 326, 292–295.
- Hoppa, M.B., Lana, B., Margas, W., Dolphin, A.C., and Ryan, T.A. (2012).  $\alpha$ 2 $\delta$  expression sets presynaptic calcium channel abundance and release probability. *Nature* 486, 122–125.
- Howe, M.W., and Dombeck, D.A. (2016). Rapid signalling in distinct dopaminergic axons during locomotion and reward. *Nature* 535, 505–510.
- Imig, C., Min, S.W., Krinner, S., Arancillo, M., Rosenmund, C., Südhof, T.C., Rhee, J., Brose, N., and Cooper, B.H. (2014). The morphological and molecular nature of synaptic vesicle priming at presynaptic active zones. *Neuron* 84, 416–431.
- Jahn, R., and Fasshauer, D. (2012). Molecular machines governing exocytosis of synaptic vesicles. *Nature* 490, 201–207.
- Kaeser, P.S., and Regehr, W.G. (2014). Molecular mechanisms for synchronous, asynchronous, and spontaneous neurotransmitter release. *Annu. Rev. Physiol.* 76, 333–363.
- Kaeser, P.S., and Regehr, W.G. (2017). The readily releasable pool of synaptic vesicles. *Curr. Opin. Neurobiol.* 43, 63–70.
- Kaeser, P.S., Kwon, H.B., Chiu, C.Q., Deng, L., Castillo, P.E., and Südhof, T.C. (2008). RIM1 $\alpha$  and RIM1 $\beta$  are synthesized from distinct promoters of the RIM1 gene to mediate differential but overlapping synaptic functions. *J. Neurosci.* 28, 13435–13447.
- Kaeser, P.S., Deng, L., Wang, Y., Dulubova, I., Liu, X., Rizo, J., and Südhof, T.C. (2011). RIM proteins tether Ca<sup>2+</sup> channels to presynaptic active zones via a direct PDZ-domain interaction. *Cell* 144, 282–295.
- Kaeser, P.S., Deng, L., Fan, M., and Südhof, T.C. (2012). RIM genes differentially contribute to organizing presynaptic release sites. *Proc. Natl. Acad. Sci. U S A* 109, 11830–11835.
- Kalla, S., Stern, M., Basu, J., Varoqueaux, F., Reim, K., Rosenmund, C., Ziv, N.E., and Brose, N. (2006). Molecular dynamics of a presynaptic active zone protein studied in Munc13-1-enhanced yellow fluorescent protein knock-in mutant mice. *J. Neurosci.* 26, 13054–13066.
- Koushika, S.P., Richmond, J.E., Hadwiger, G., Weimer, R.M., Jorgensen, E.M., and Nonet, M.L. (2001). A post-docking role for active zone protein Rim. *Nat. Neurosci.* 4, 997–1005.
- Lakso, M., Pichel, J.G., Gorman, J.R., Sauer, B., Okamoto, Y., Lee, E., Alt, F.W., and Westphal, H. (1996). Efficient *in vivo* manipulation of mouse genomic sequences at the zygote stage. *Proc. Natl. Acad. Sci. U S A* 93, 5860–5865.
- Lein, E.S., Hawrylycz, M.J., Ao, N., Ayres, M., Bensinger, A., Bernard, A., Boe, A.F., Boguski, M.S., Brockway, K.S., Byrnes, E.J., et al. (2007). Genome-wide atlas of gene expression in the adult mouse brain. *Nature* 445, 168–176.
- Lin, J.Y., Lin, M.Z., Steinbach, P., and Tsien, R.Y. (2009). Characterization of engineered channelrhodopsin variants with improved properties and kinetics. *Biophys. J.* 96, 1803–1814.
- Liu, C., and Kaeser, P.S. (2019). Mechanisms and regulation of dopamine release. *Curr. Opin. Neurobiol.* 57, 46–53.
- Liu, Y., Schirra, C., Edelmann, L., Matti, U., Rhee, J., Hof, D., Bruns, D., Brose, N., Rieger, H., Stevens, D.R., and Rettig, J. (2010). Two distinct secretory vesicle-priming steps in adrenal chromaffin cells. *J. Cell Biol.* 190, 1067–1077.
- Liu, K.S.Y., Siebert, M., Mertel, S., Knoche, E., Wegener, S., Wichmann, C., Matkovic, T., Muhammad, K., Depner, H., Mettke, C., et al. (2011). RIM-binding protein, a central part of the active zone, is essential for neurotransmitter release. *Science* 334, 1565–1569.
- Liu, C., Kershberg, L., Wang, J., Schneeberger, S., and Kaeser, P.S. (2018). Dopamine secretion is mediated by sparse active zone-like release sites. *Cell* 172, 706–718.e15.
- Liu, C., Goel, P., and Kaeser, P.S. (2021). Spatial and temporal scales of dopamine transmission. *Nat. Rev. Neurosci.* 22, 345–358.
- Luo, F., Sclip, A., Jiang, M., and Südhof, T.C. (2020). Neurexins cluster Ca<sup>2+</sup> channels within the presynaptic active zone. *EMBO J.* 39, e103208.
- Ma, C., Li, W., Xu, Y., and Rizo, J. (2011). Munc13 mediates the transition from the closed syntaxin-Munc18 complex to the SNARE complex. *Nat. Struct. Mol. Biol.* 18, 542–549.
- Ma, C., Su, L., Seven, A.B., Xu, Y., and Rizo, J. (2013). Reconstitution of the vital functions of Munc18 and Munc13 in neurotransmitter release. *Science* 339, 421–425.
- Man, K.N.M., Imig, C., Walter, A.M., Pinheiro, P.S., Stevens, D.R., Rettig, J., Sørensen, J.B., Cooper, B.H., Brose, N., and Wojcik, S.M. (2015). Identification of a Munc13-sensitive step in chromaffin cell large dense-core vesicle exocytosis. *eLife* 4, e10635.

- Marcott, P.F., Gong, S., Donthamsetti, P., Grinnell, S.G., Nelson, M.N., Newman, A.H., Birnbaumer, L., Martemyanov, K.A., Javitch, J.A., and Ford, C.P. (2018). Regional heterogeneity of D2-receptor signaling in the dorsal striatum and nucleus accumbens. *Neuron* 98, 575–587.e4.
- Matsuda, W., Furuta, T., Nakamura, K.C., Hioki, H., Fujiyama, F., Arai, R., and Kaneko, T. (2009). Single nigrostriatal dopaminergic neurons form widely spread and highly dense axonal arborizations in the neostriatum. *J. Neurosci.* 29, 444–453.
- Menegas, W., Akiti, K., Amo, R., Uchida, N., and Watabe-Uchida, M. (2018). Dopamine neurons projecting to the posterior striatum reinforce avoidance of threatening stimuli. *Nat. Neurosci.* 21, 1421–1430.
- Milosevic, I., Sørensen, J.B., Lang, T., Krauss, M., Nagy, G., Haucke, V., Jahn, R., and Neher, E. (2005). Plasmalemmal phosphatidylinositol-4,5-bisphosphate level regulates the releasable vesicle pool size in chromaffin cells. *J. Neurosci.* 25, 2557–2565.
- Missale, C., Nash, S.R.S., Robinson, S.W., Jaber, M., and Caron, M.G. (1998). Dopamine receptors: from structure to function. *Physiol. Rev.* 78, 189–225.
- Müller, M., Liu, K.S.Y., Sigrist, S.J., and Davis, G.W. (2012). RIM controls homeostatic plasticity through modulation of the readily-releasable vesicle pool. *J. Neurosci.* 32, 16574–16585.
- Patel, M.R., and Shen, K. (2009). RSY-1 is a local inhibitor of presynaptic assembly in *C. elegans*. *Science* 323, 1500–1503.
- Pereira, D.B., Schmitz, Y., Mészáros, J., Merchant, P., Hu, G., Li, S., Henke, A., Lizardi-Ortiz, J.E., Karpowicz, R.J., Jr., Morgenstern, T.J., et al. (2016). Fluorescent false neurotransmitter reveals functionally silent dopamine vesicle clusters in the striatum. *Nat. Neurosci.* 19, 578–586.
- Persoon, C.M., Hoogstraaten, R.I., Nassal, J.P., van Weering, J.R.T., Kaeser, P.S., Toonen, R.F., and Verhage, M. (2019). The RAB3-RIM pathway is essential for the release of neuromodulators. *Neuron* 104, 1065–1080.e12.
- Renden, R., Berwin, B., Davis, W., Ann, K., Chin, C.-T., Kreber, R., Ganetzky, B., Martin, T.F.J., and Broadie, K. (2001). *Drosophila* CAPS is an essential gene that regulates dense-core vesicle release and synaptic vesicle fusion. *Neuron* 31, 421–437.
- Rhee, J.S., Betz, A., Pyott, S., Reim, K., Varoqueaux, F., Augustin, I., Hesse, D., Südhof, T.C., Takahashi, M., Rosenmund, C., and Brose, N. (2002). Beta phorbol ester- and diacylglycerol-induced augmentation of transmitter release is mediated by Munc13s and not by PKCs. *Cell* 108, 121–133.
- Richmond, J.E., Davis, W.S., and Jorgensen, E.M. (1999). UNC-13 is required for synaptic vesicle fusion in *C. elegans*. *Nat. Neurosci.* 2, 959–964.
- Robinson, B.G., Cai, X., Wang, J., Bunzow, J.R., Williams, J.T., and Kaeser, P.S. (2019). RIM is essential for stimulated but not spontaneous somatodendritic dopamine release in the midbrain. *eLife* 8, e47972.
- Sakamoto, H., Ariyoshi, T., Kimpara, N., Sugao, K., Taiko, I., Takikawa, K., Asanuma, D., Namiki, S., and Hirose, K. (2018). Synaptic weight set by Munc13-1 supramolecular assemblies. *Nat. Neurosci.* 21, 41–49.
- Saunders, A., Macosko, E.Z., Wysoker, A., Goldman, M., Krienen, F.M., de Rivera, H., Bien, E., Baum, M., Bortolin, L., Wang, S., et al. (2018). Molecular diversity and specializations among the cells of the adult mouse brain. *Cell* 174, 1015–1030.e16.
- Schindelin, J., Arganda-Carreras, I., Frise, E., Kaynig, V., Longair, M., Pietzsch, T., Preibisch, S., Rueden, C., Saalfeld, S., Schmid, B., et al. (2012). Fiji: an open-source platform for biological-image analysis. *Nat. Methods* 9, 676–682.
- Schoch, S., Castillo, P.E., Jo, T., Mukherjee, K., Geppert, M., Wang, Y., Schmitz, F., Malenka, R.C., and Südhof, T.C. (2002). RIM1alpha forms a protein scaffold for regulating neurotransmitter release at the active zone. *Nature* 415, 321–326.
- Sclip, A., and Südhof, T.C. (2020). LAR receptor phospho-tyrosine phosphatases regulate NMDA-receptor responses. *eLife* 9, e53406.
- Serra-Pagès, C., Kedersha, N.L., Fazikas, L., Medley, Q., Debant, A., and Streuli, M. (1995). The LAR transmembrane protein tyrosine phosphatase and a coiled-coil LAR-interacting protein co-localize at focal adhesions. *EMBO J.* 14, 2827–2838.
- Serra-Pagès, C., Medley, Q.G., Tang, M., Hart, A., and Streuli, M. (1998). Liprins, a family of LAR transmembrane protein-tyrosine phosphatase-interacting proteins. *J. Biol. Chem.* 273, 15611–15620.
- Sigler, A., Oh, W.C., Imig, C., Altas, B., Kawabe, H., Cooper, B.H., Kwon, H.-B., Rhee, J.-S., and Brose, N. (2017). Formation and maintenance of functional spines in the absence of presynaptic glutamate release. *Neuron* 94, 304–311.e4.
- Siksou, L., Varoqueaux, F., Pascual, O., Triller, A., Brose, N., and Marty, S. (2009). A common molecular basis for membrane docking and functional priming of synaptic vesicles. *Eur. J. Neurosci.* 30, 49–56.
- Silm, K., Yang, J., Marcott, P.F., Asensio, C.S., Eriksen, J., Guthrie, D.A., Newman, A.H., Ford, C.P., and Edwards, R.H. (2019). Synaptic vesicle recycling pathway determines neurotransmitter content and release properties. *Neuron* 102, 786–800.e5.
- Südhof, T.C. (2012). The presynaptic active zone. *Neuron* 75, 11–25.
- Sulzer, D., Cragg, S.J., and Rice, M.E. (2016). Striatal dopamine neurotransmission: regulation of release and uptake. *Basal Ganglia* 6, 123–148.
- Tang, A.-H., Chen, H., Li, T.P., Metzbowler, S.R., MacGillavry, H.D., and Blanpied, T.A. (2016). A trans-synaptic nanocolumn aligns neurotransmitter release to receptors. *Nature* 536, 210–214.
- Threlfell, S., Lalic, T., Platt, N.J., Jennings, K.A., Deisseroth, K., and Cragg, S.J. (2012). Striatal dopamine release is triggered by synchronized activity in cholinergic interneurons. *Neuron* 75, 58–64.
- Uchigashima, M., Ohtsuka, T., Kobayashi, K., and Watanabe, M. (2016). Dopamine synapse is a neuroligin-2-mediated contact between dopaminergic presynaptic and GABAergic postsynaptic structures. *Proc. Natl. Acad. Sci. U S A* 113, 4206–4211.
- van de Bospoort, R., Farina, M., Schmitz, S.K., de Jong, A., de Wit, H., Verhage, M., and Toonen, R.F. (2012). Munc13 controls the location and efficiency of dense-core vesicle release in neurons. *J. Cell Biol.* 199, 883–891.
- van den Bogaart, G., Meyenberg, K., Risselada, H.J., Amin, H., Willig, K.I., Hubrich, B.E., Dier, M., Hell, S.W., Grubmüller, H., Diederichsen, U., and Jahn, R. (2011). Membrane protein sequestering by ionic protein-lipid interactions. *Nature* 479, 552–555.
- van Keimpema, L., Kooistra, R., Toonen, R.F., and Verhage, M. (2017). CAPS-1 requires its C2, PH, MHD1 and DCV domains for dense core vesicle exocytosis in mammalian CNS neurons. *Sci. Rep.* 7, 10817.
- Varoqueaux, F., Sigler, A., Rhee, J.S., Brose, N., Enk, C., Reim, K., and Rosenmund, C. (2002). Total arrest of spontaneous and evoked synaptic transmission but normal synaptogenesis in the absence of Munc13-mediated vesicle priming. *Proc. Natl. Acad. Sci. U S A* 99, 9037–9042.
- Varoqueaux, F., Sons, M.S., Plomp, J.J., and Brose, N. (2005). Aberrant morphology and residual transmitter release at the Munc13-deficient mouse neuromuscular synapse. *Mol. Cell Biol.* 25, 5973–5984.
- Verhage, M., Maia, A.S., Plomp, J.J., Brussaard, A.B., Heeroma, J.H., Vermeer, H., Toonen, R.F., Hammer, R.E., van den Berg, T.K., Missler, M., et al. (2000). Synaptic assembly of the brain in the absence of neurotransmitter secretion. *Science* 287, 864–869.
- Wang, S.S.H., Held, R.G., Wong, M.Y., Liu, C., Karakhanyan, A., and Kaeser, P.S. (2016). Fusion competent synaptic vesicles persist upon active zone disruption and loss of vesicle docking. *Neuron* 91, 777–791.
- Wong, M.Y., Liu, C., Wang, S.S.H., Roquas, A.C.F., Fowler, S.C., and Kaeser, P.S. (2018). Liprin- $\alpha$ 3 controls vesicle docking and exocytosis at the active zone of hippocampal synapses. *Proc. Natl. Acad. Sci. U S A* 115, 2234–2239.
- Wu, X., Cai, Q., Shen, Z., Chen, X., Zeng, M., Du, S., and Zhang, M. (2019). RIM and RIM-BP form presynaptic active-zone-like condensates via phase separation. *Mol. Cell* 73, 971–984.e5.

Yagishita, S., Hayashi-Takagi, A., Ellis-Davies, G.C.R., Urakubo, H., Ishii, S., and Kasai, H. (2014). A critical time window for dopamine actions on the structural plasticity of dendritic spines. *Science* 345, 1616–1620.

Zhen, M., and Jin, Y. (1999). The Liprin protein SYD-2 regulates the differentiation of presynaptic termini in *C. elegans*. *Nature* 401, 371–375.

Zhou, F.-M., Liang, Y., and Dani, J.A. (2001). Endogenous nicotinic cholinergic activity regulates dopamine release in the striatum. *Nat. Neurosci.* 4, 1224–1229.

Zürner, M., Mittelstaedt, T., tom Dieck, S., Becker, A., and Schoch, S. (2011). Analyses of the spatiotemporal expression and subcellular localization of liprin- $\alpha$  proteins. *J. Comp. Neurol.* 519, 3019–3039.

STAR★METHODS

KEY RESOURCES TABLE

REAGENT or RESOURCE	SOURCE	IDENTIFIER
<b>Antibodies</b>		
Mouse monoclonal anti- $\beta$ -Tubulin	Sigma-Aldrich	Cat#T4026; RRID:AB_477577
Rabbit polyclonal anti-Munc13-1	Synaptic Systems	Cat# 126 103; RRID:AB_887733
Rabbit polyclonal anti-Munc13-1 (C-terminal #N395)	(Betz et al., 1997)	N/A
Rabbit polyclonal anti-Munc13-1 (N-terminal #40)	(Cooper et al., 2012; Varoqueaux et al., 2005)	N/A
Mouse monoclonal IgG1 anti-synaptophysin-1 (A100)	Synaptic Systems	Cat# 101 011; RRID:AB_887824
Guinea pig polyclonal anti-Tyrosine hydroxylase (A111)	Synaptic Systems	Cat# 213 104, RRID:AB_2619897
Rabbit polyclonal anti-Tyrosine hydroxylase (A66)	Millipore	Cat# AB152; RRID:AB_390204
Rabbit monoclonal anti-GFP (A195)	Thermo Fisher Scientific	Cat# G10362; RRID:AB_2536526
Mouse monoclonal IgG2a anti-Bassoon SAP7F407 (A85)	Enzo Life Sciences	Cat# ADI-VAM-PS003-F; RRID:AB_11181058
Rabbit polyclonal antibody anti-RIM1 (A58)	Synaptic Systems	Cat# 140 003; RRID:AB_887774
Rabbit polyclonal anti-ELKS2 $\alpha$ (1029, A136)	(Held et al., 2016)	E3-1029
Mouse monoclonal anti-HA-tag 6E2 (A250)	Cell Signaling Technology	Cat# 2367; RRID:AB_10691311
<b>Chemicals, peptides, and recombinant proteins</b>		
Tetrodotoxin	Tocris	Cat. No. 1078
Dihydro- $\beta$ -erythroidine hydrobromide	Tocris	Cat. No. 2349
Mammalian Protease Inhibitor Cocktail	Sigma	Cat# P8340
Image-iT FX Signal Enhancer	Thermo Fisher Scientific	Cat# I36933
<b>Experimental models: Cell lines</b>		
Derivate of 129/Ola mouse embryonic stem cell line E14	(Hooper et al., 1987)	RRID:CVCL_9108
Mouse embryonic fibroblasts (MEF feeder cells)	Xenogen, Alameda, CA, USA	N/A
HEK293T	ATCC	Cat#: CRL-3216; RRID:CVCL_0063
<b>Experimental models: Organisms/strains</b>		
Mouse: Munc13-1 <sup>fl/fl</sup>	This study	N/A
Mouse: Munc13-1 cKO <sup>fl</sup>	This study	N/A
Mouse: Munc13-1 <sup>-/-</sup> ; Unc13a <sup>tm1Bros</sup>	(Augustin et al., 1999)	MGI:2449468
Mouse: Munc13-1 <sup>mNeo/mNeo</sup>	(Rhee et al., 2002)	N/A; mutated <i>Unc13a</i> gene containing a neomycin cassette
Mouse: Munc13-2 <sup>-/-</sup> ; Unc13b <sup>tm1Rmnd</sup>	(Varoqueaux et al., 2002)	MGI:2449706
Mouse: Munc13-3 <sup>-/-</sup> ; Unc13c <sup>tm1Bros</sup>	(Augustin et al., 2001)	MGI:2449467
Mouse: FLP deleter; Gt(ROSA)26Sor <sup>tm1(FLP1)Dym</sup>	(Farley et al., 2000)	MGI:2429412
Mouse: Ella-Cre; Tg(Ella-cre)C5379Lmgd	(Lakso et al., 1996)	MGI:2137691
Mouse: DAT <sup>ires-cre</sup> ; B6.SJL-Slc6a3 <sup>tm1.1(cre)Bkmm/J</sup>	(Bäckman et al., 2006)	JAX 006660
Mouse: Munc13-1-EYFP; Unc13a <sup>tm3Bros</sup>	(Kalla et al., 2006)	MGI:3695486
Mouse: Liprin- $\alpha$ 3 <sup>-/-</sup>	(Wong et al., 2018)	N/A
Mouse: Liprin- $\alpha$ 2 <sup>fl/fl</sup>	(Emperador-Melero et al., 2021a)	MGI:2443834
Mouse: RIM-BP1 <sup>fl/fl</sup> ; Tspoap1 <sup>tm1Sud/J</sup>	(Acuna et al., 2015)	JAX: 023643
Mouse: RIM-BP2 <sup>fl/fl</sup> ; Rimpb2 <sup>tm1Sud/J</sup>	(Acuna et al., 2015)	JAX: 023644
Mouse: RIM1 <sup>fl/fl</sup> ; Rims1 <sup>tm3Sud/J</sup>	(Kaesler et al., 2008)	JAX:015832
Mouse: RIM2 <sup>fl/fl</sup> ; Rims2 <sup>tm1.1Sud/J</sup>	(Kaesler et al., 2011)	JAX:015833

(Continued on next page)

REAGENT or RESOURCE	SOURCE	IDENTIFIER
<b>Continued</b>		
<b>Recombinant DNA</b>		
BAC: BMQ-441L13 (pBACe3.6 backbone)	(Adams et al., 2005)	N/A
Targeting vector: PL253-M13-1 <sup>loxP-e21-FRT-Neo-FRT-loxP-HSV-TK</sup>	This study	N/A
pAAV-hSyn-flex-RIM1-Zn-HA (p866)	This study	N/A
pAAV-hSyn-flex-RIM1-ΔZn-HA (p865)	This study	N/A
pAAV-hSyn-flex-RIM1-Zn-HA-C <sub>2</sub> B (p902)	This study	N/A
pAAV-hSyn-flex-RIM1-Zn-HA- Zn-C <sub>2</sub> B <sup>KE</sup> (p903)	This study	N/A
pAAV-hSyn-flex-RIM1-Zn-HA-PCP (p968)	This study	N/A
pAAV-hSyn-flex-oChIEF-citrine (p901)	Addgene, (Lin et al., 2009)	Plasmid# 50973; RRID:Addgene_50973
pAAV-hSyn-flex-citrine (p906)	This study	N/A
<b>Oligonucleotides</b>		
Munc13-1 genotyping: 5'-CTCTATGGCTTCTGAGCGGAAA-3'	This study	LabID:27121
Munc13-1 genotyping: 5'-AGTTTTTCATCTGTAGCCCGAT-3'	This study	LabID:27122
Munc13-1 genotyping: 5'-CAACTGGCCAAGAAGACTAGAGGA-3'	This study	LabID:27123
Munc13-1 genotyping: 5'-GCACGGGAATGTTGAATGGTCTT -3'	This study	LabID:27124
Munc13-1 splice variants, exon 20; sense: 5'-CCATCCGGCTTCACATCAGT-3'	This study	LabID:24609
Munc13-1 splice variants, exon 23; antisense: 5'-CGATCCGCAGAGAATTGTGTAGC-3'	This study	LabID:34504
Munc13-1 splice variants, exon 25; antisense: 5'-TACTCCCGCCATAGAGCTCA-3'	This study	LabID:34505
<b>Software and algorithms</b>		
Custom machine learning code for TH morphology	This study	<a href="https://doi.org/10.5281/zenodo.5576622">https://doi.org/10.5281/zenodo.5576622</a>
Custom MATLAB code	(Liu et al., 2018)	<a href="https://doi.org/10.5281/zenodo.5576635">https://doi.org/10.5281/zenodo.5576635</a>
DNASTAR Lasergene 13	DNASTAR	RRID:SCR_011854; <a href="https://www.dnastar.com/software/lasergene/">https://www.dnastar.com/software/lasergene/</a>
GraphPad Prism	GraphPad	RRID:SCR_002798; <a href="https://www.graphpad.com/">https://www.graphpad.com/</a>
Fiji	(Schindelin et al., 2012)	RRID:SCR_002285; <a href="https://imagej.net/software/fiji/downloads">https://imagej.net/software/fiji/downloads</a>
DeltaVision OMX imaging system	GE Healthcare	RRID: SCR_019956; <a href="https://scicrunch.org/resources/Tools/record/nlx_144509-1/SCR_019956/resolver?q=SCR_019956&amp;l=SCR_019956">https://scicrunch.org/resources/Tools/record/nlx_144509-1/SCR_019956/resolver?q=SCR_019956&amp;l=SCR_019956</a>
Olympus Fluoview FV10-ASW	Olympus Fluoview	RRID:SCR_014215; <a href="https://www.photonics.com/Product.aspx?PRID=47380">https://www.photonics.com/Product.aspx?PRID=47380</a>
pClamp	Molecular Devices	RRID:SCR_011323; <a href="https://www.moleculardevices.com/products/software/pclamp.html">https://www.moleculardevices.com/products/software/pclamp.html</a>
Imaris 9.0.2	Oxford Instruments	RRID:SCR_007370; <a href="https://imaris.oxinst.com/packages">https://imaris.oxinst.com/packages</a>

## RESOURCE AVAILABILITY

### Lead contact

Further information and requests for resources and reagents should be directed to and will be fulfilled by the Lead Contact, Pascal S. Kaeser ([kaeser@hms.harvard.edu](mailto:kaeser@hms.harvard.edu)).

### Materials availability

Plasmids generated for this study will be shared without restrictions. Antibodies and recombinant viruses generated for this study are exhaustible and will be shared as long as they are available. Mouse lines will be shared upon request within the limits of the respective material transfer agreements.

**Data and code availability**

The original code has been deposited to Zenodo and is publicly available as listed in the key resources table. Data reported in this paper are available from the lead contact upon reasonable request. Any additional information required to reanalyze the data reported in this paper is available from the lead contact upon request.

**EXPERIMENTAL MODEL AND SUBJECT DETAILS**

All animal experiments were done in accordance with approved protocols of either the Harvard University Animal Care and Use Committee, or the Niedersächsisches Landesamt für Verbraucherschutz und Lebensmittelsicherheit (LAVES; 33.19.42502-04-15/1817) and according to the European Union Directive 63/2010/EU and ETS 123. Conditional deletion of active zone proteins in dopamine neurons was performed using DAT<sup>IRES-cre</sup> mice (JAX: 006660, B6.SJL-Slc6a3<sup>tm1.1(cre)Bkmm/J</sup>, [Bäckman et al., 2006](#)). Unless noted otherwise, cKO<sup>DA</sup> mice are mice that have two floxed alleles for active zone genes and one DAT<sup>IRES-cre</sup> allele, and corresponding control mice are either siblings or age-matched mice from the same breeding colony with one floxed allele per gene and one DAT<sup>IRES-cre</sup> allele. Given that dopamine release in control mice across experiments in various mutants is similar, we conclude that heterozygosity in any of these alleles has no strong effects on dopamine release.

**RIM cKO<sup>DA</sup> mice** were generated previously ([Liu et al., 2018](#)) by breeding DAT<sup>IRES-cre</sup> mice to RIM1 $\alpha\beta$  (JAX:015832, Rims1<sup>tm3Sud/J</sup>, [Kaeser et al., 2008](#)) and RIM2 $\alpha\beta\gamma$  (JAX:015833, Rims2<sup>tm1.1Sud/J</sup>, [Kaeser et al., 2011](#)) floxed mice. RIM cKO<sup>DA</sup> were born in numbers following approximately Mendelian ratios (assessed in breeding pairs with 12.5% expected RIM cKO<sup>DA</sup> mice: 38 of 407 pups, 9.3%), did not display any obvious developmental phenotypes, and their body weight was normal at the time of stereotaxic surgery (18 RIM cKO<sup>DA</sup> mice, 19.0  $\pm$  0.6 g; 18 unrelated control mice, 19.5  $\pm$  1.0 g,  $p = 0.6$ , Mann-Whitney test).

**Munc13 cKO<sup>DA</sup> mice** were produced with newly generated floxed Munc13-1 mice (after crossing to flp deleter mice, [Farley et al., 2000](#)) that were crossed to constitutive knockout mice for Munc13-2 (Unc13b<sup>tm1Rmnd</sup>, RRID\_MGI:2449706, [Varoqueaux et al., 2002](#)) and Munc13-3 (Unc13c<sup>tm1Bros</sup>, RRID\_MGI:2449467, [Augustin et al., 2001](#)) and DAT<sup>IRES-cre</sup> mice. Munc13 cKO<sup>DA</sup> were Munc13-1<sup>+/+</sup> x Munc13-2<sup>-/-</sup> x Munc13-3<sup>-/-</sup> x DAT<sup>IRES-cre +/cre</sup>. Munc13 control mice were littermate mice with Munc13-1<sup>+/+</sup> x Munc13-2<sup>+/-</sup> x Munc13-3<sup>-/-</sup> x DAT<sup>IRES-cre +/cre</sup>. The Munc13-3 allele was maintained at homozygosity in breeding pairs to enable the generation of Munc13 control and Munc13 cKO<sup>DA</sup> siblings from the same litters/breedings. Munc13 cKO<sup>DA</sup> mice were born in numbers following approximately expected numbers from Mendelian ratios (assessed in breeding pairs with 12.5% expected Munc13 cKO<sup>DA</sup> mice: 26 of 179 pups, 14.5%), but were smaller than Munc13 control mice at the time of stereotaxic surgery (21 Munc13 cKO<sup>DA</sup> mice, 14.0  $\pm$  1.0 g; 21 Munc13 control mice, 22.1  $\pm$  1.4 g,  $p < 0.001$ , Mann-Whitney test), likely due to constitutive double knockout of Munc13-2 and Munc13-3. For assessment of protein content and autaptic phenotypes, Munc13-1 floxed mice were cre-recombined in the germline using Ella-cre mice ([Lakso et al., 1996](#)), and protein content was compared to two previously established Munc13-1 knockout mouse lines ([Augustin et al., 1999](#); [Rhee et al., 2002](#)).

**RIM-BP cKO<sup>DA</sup> mice** were generated by crossing RIM-BP1<sup>+/+</sup> x RIM-BP2<sup>+/+</sup> mice (RIM-BP1: JAX: 023643; Tsopap1<sup>tm1Sud</sup>, RIM-BP2: JAX: 023644; Rimbpb2<sup>tm1Sud/J</sup>, [Acuna et al., 2015](#)), obtained from Dr. T. C. Südhof, to DAT<sup>IRES-cre</sup> mice. RIM-BP cKO<sup>DA</sup> mice were born in numbers following approximately expected numbers from Mendelian ratios (assessed in breeding pairs with 12.5% expected RIM-BP cKO<sup>DA</sup> mice: 36 of 257 pups, 14.0%), did not display any obvious developmental phenotypes and their body weight was normal at the time of stereotaxic surgery (15 RIM-BP cKO<sup>DA</sup> mice, 19.6  $\pm$  1.0 g; 15 RIM-BP control mice, 20.1  $\pm$  0.9 g,  $p = 0.7$ , Mann-Whitney test).

**Liprin- $\alpha$  cKO<sup>DA</sup> mice** were produced by crossing recently generated Liprin- $\alpha$ 2<sup>+/+</sup> mice ([Emperador-Melero et al., 2021a](#)) to constitutive Liprin- $\alpha$ 3 knockout mice ([Wong et al., 2018](#)) and DAT<sup>IRES-cre</sup> mice. Liprin- $\alpha$  cKO<sup>DA</sup> were Liprin- $\alpha$ 2<sup>+/+</sup> x Liprin- $\alpha$ 3<sup>-/-</sup> x DAT<sup>IRES-cre +/cre</sup>, and Liprin- $\alpha$  control mice were littermates with Liprin- $\alpha$ 2<sup>+/+</sup> x Liprin- $\alpha$ 3<sup>+/-</sup> x DAT<sup>IRES-cre +/cre</sup>. Liprin- $\alpha$  cKO<sup>DA</sup> mice were born in numbers following approximately expected numbers from Mendelian ratios (assessed in breeding pairs with 12.5% expected Liprin- $\alpha$  cKO<sup>DA</sup> mice: 15 of 168 pups, 8.9%), did not display any obvious developmental phenotypes and their body weight was normal at the time of stereotaxic surgery (25 Liprin- $\alpha$  cKO<sup>DA</sup> mice, 20.5  $\pm$  1.0 g; 25 Liprin- $\alpha$  control mice, 22.0  $\pm$  1.1 g,  $p = 0.2$ , Mann-Whitney test).

**Munc13-1-EYFP mice** were previously described (RRID\_MGI:3695486; Unc13a<sup>tm3Bros</sup>, [Kalla et al., 2006](#)), and homozygote Munc13-1-EYFP mice and unrelated age-matched control mice were used for all experiments.

All mice were group housed in a 12 h light-dark cycle with free access to water and food. All experiments with genotype comparisons were done in male and female mice, and the experimenter was blind to genotype throughout data acquisition and analysis.

**METHOD DETAILS****Rescue constructs and production of AAV viruses**

AAVs were used to either deliver domains of active zone proteins to dopamine neurons or to stimulate dopamine neurons by inducing expression of the fast channelrhodopsin oChIEF. The RIM rescue AAVs contained the following residues (residue numbering according to Uniprot ID Q9JIR4, all clones missing splice inserts <sub>83</sub>NI...DW<sub>105</sub>, <sub>1084</sub>HS...TR<sub>1169</sub>, <sub>1207</sub>AS...QT<sub>1378</sub>, identical to previous RIM expression and rescue experiments ([Deng et al., 2011](#); [de Jong et al., 2018](#); [Kaeser et al., 2011](#); [Tang et al., 2016](#)): AAV5-hSyn-FLEX-RIM1-Zn-HA/p866<sub>1</sub>MS...QD<sub>213</sub> (HA-tag inserted at C terminus), AAV5-hSyn-flex-RIM1- $\Delta$ Zn-HA/p865

MSSAVAG<sup>-597HP</sup>....RS<sub>1615</sub> (HA-tag inserted between residues <sub>1379</sub>E-S<sub>1380</sub>), and AAV5-hSyn-flex-RIM1-Zn-HA-C<sub>2</sub>B/p902 <sub>1</sub>MS....SS<sub>596</sub>-AAAGYPYDVPDYAAGAP<sup>-1379SG</sup>....RS<sub>1615</sub> (HA-tag inserted in the linker between SS<sub>596</sub> and <sub>1379</sub>SG as indicated in *italic*), AAV5-hSyn-flex-RIM1-Zn-HA-C<sub>2</sub>B<sup>KE</sup>/p903 (identical to AAV5-hSyn-flex-RIM1-Zn-HA-C<sub>2</sub>B/p902 except for E1513K and E1515K point mutations), AAV5-hSyn-flex-RIM1-Zn-HA-PCP/p968 <sub>1</sub>MS....QD<sub>213</sub>-AAAGYPYDVPDYAAGAP<sup>-597HP</sup>....EQ<sub>1256</sub> (HA-tag inserted in the linker between QD<sub>213</sub> and <sub>597</sub>HP as indicated in *italic*). AAV5-hSyn-flex-citrine/p906 was used as a control. For optogenetic activation of striatal dopamine fibers, AAV5-hSyn-flex-oChIEF-citrine/p901 was used to drive cre-dependent expression of oChIEF-citrine (RRID:Addgene\_50973, Lin et al., 2009). All AAVs were generated using Ca<sup>2+</sup>-phosphate transfection in HEK293T cells (mycoplasma free cell line from ATCC, Cat#: CRL-3216, RRID:CVCL\_0063) as AAV2/5 serotypes. 72 h after transfection, cells were collected, lysed, and viral particles were extracted and purified from the 40% layer after iodixanol gradient ultracentrifugation. Quantitative rtPCR was used to estimate the viral genomic titers (10<sup>12</sup> to 10<sup>14</sup> viral genome copies/ml).

### Stereotaxic surgery

Mice (P24–P54) were anesthetized using 5% isoflurane and mounted on a stereotaxic frame. Stable anesthesia was maintained during surgery with 1.5%–2% isoflurane. 1  $\mu$ l of AAV viral solution was injected unilaterally into the right substantia nigra pars compacta (SNc – 0.6 mm anterior, 1.3 mm lateral of Lambda and 4.2 mm below pia) using a microinjector (PHD ULTRA syringe pump, Harvard Apparatus) at 100 nl/min. Mice were treated with post-surgical analgesia and were allowed to recover for at least 21 d prior to electrophysiology. Stereotaxic procedures were performed according to protocols approved by the Harvard University Animal Care and Use Committee.

### Electrophysiology in brain slices

Recordings in acute brain slices were performed in the dorsolateral striatum as described before (Banerjee et al., 2020; Liu et al., 2018). Male and female mice at 42–191 d of age were anesthetized with isoflurane and decapitated. 250  $\mu$ m thick sagittal brain sections containing dorsal striatum were cut on a vibratome (Leica, VT1200s) using ice-cold sucrose-based cutting solution with (in mM): 75 sucrose, 75 NaCl, 26.2 NaHCO<sub>3</sub>, 1 NaH<sub>2</sub>PO<sub>4</sub>, 1 sodium ascorbate, 2.5 KCl, 7.5 MgSO<sub>4</sub>, 12 glucose, 1 myo-inositol, 3 sodium pyruvate, pH 7.4, 300–310 mOsm. Slices were incubated in incubation solution bubbled with 95% O<sub>2</sub> and 5% CO<sub>2</sub> containing (in mM): 126 NaCl, 26.2 NaHCO<sub>3</sub>, 1 NaH<sub>2</sub>PO<sub>4</sub>, 2.5 KCl, 1 sodium ascorbate, 3 sodium pyruvate, 1.3 MgSO<sub>4</sub>, 2 CaCl<sub>2</sub>, 12 glucose, 1 myo-inositol (pH 7.4, 305–310 mOsm) at room temperature for 1 h. All recordings were done at 34–36°C, and slices were continuously perfused with artificial cerebrospinal fluid (ACSF) at 3–4 ml/min bubbled with 95% O<sub>2</sub> and 5% CO<sub>2</sub>. ACSF contained (in mM): 126 NaCl, 26.2 NaHCO<sub>3</sub>, 2.5 KCl, 2 CaCl<sub>2</sub> (unless noted otherwise), 1.3 MgSO<sub>4</sub>, 1 NaH<sub>2</sub>PO<sub>4</sub>, 12 glucose, pH 7.4, 300–310 mOsm. Recordings were completed within 5 h of slicing. The experimenter was blind to genotype throughout recording and data analyses. All data acquisition and analyses for electrophysiology were done using pClamp10 (Clampex, Axon Instruments).

For carbon fiber amperometry, carbon fiber microelectrodes (CFEs, 7  $\mu$ m diameter, 200–350  $\mu$ m long) were custom-made by inserting carbon fiber filaments (Goodfellow) into glass capillaries. On the day of recording, each new CFE was calibrated before use by puffing freshly made dopamine solutions of increasing concentrations (0, 1, 5, 10, 20  $\mu$ M) in ACSF for 10 s. The currents for each concentration of dopamine were plotted against the dopamine concentration and only CFEs with a linear relationship were used. For all genotype comparisons, each control and cKO<sup>DA</sup> littermate pair was recorded in an interleaved manner on the same day using the same carbon fiber. For RIM cKO<sup>DA</sup> rescue experiments, an uninjected, unrelated control mouse was first recorded to establish stable carbon fiber recordings followed by inter-leafed recordings from two injected littermate RIM cKO<sup>DA</sup> mice. CFEs were slowly inserted at 20–60  $\mu$ m below the slice surface in the dorsolateral striatum and were held at 600 mV to record dopamine release. Signals were sampled at 10 kHz and low-pass filtered at 400 Hz. Dopamine release was evoked by electrical or optogenetic stimulation every 2 min. Dopamine release phenotypes in Munc13 cKO<sup>DA</sup>, Liprin- $\alpha$  cKO<sup>DA</sup> and RIM-BP cKO<sup>DA</sup> mice were performed with electrical stimulation, optogenetic stimulation after expression of oChIEF, or KCl stimulation. All rescue experiments were performed with electrical or KCl stimulation only because efficient co-expression of optogenetic actuators and rescue cDNAs was not possible due to packaging limits of the AAV system.

Electrical stimulation was applied through an ACSF-filled glass pipette (tip diameter 3–5  $\mu$ m) connected to a linear stimulus isolator (A395, World Precision Instruments) and was used to deliver a monopolar electrical stimulus (10–90  $\mu$ A) to striatal slices. The stimulation pipette was kept at 20–30  $\mu$ m below the slice surface in dorsolateral striatum and 100–120  $\mu$ m away from the tip of CFE. A biphasic wave (0.25  $\mu$ s in each phase) was applied to evoke dopamine release. Electrical stimulation was delivered either as a single stimulus or 10 Hz trains of 90  $\mu$ A or single stimuli of increasing intensities (10–90  $\mu$ A). To assess the magnitude of cholinergically triggered dopamine release, the response to a single electrical pulse at 90  $\mu$ A before and after application of 1  $\mu$ M DH $\beta$ E (Tocris, Catalogue No.# 2349) to block  $\beta$ 2-containing nAChRs was measured.

Optogenetic stimulation was used to evoke dopamine release in areas in the dorsolateral striatum with uniform citrine fluorescence. Optogenetic stimulation was applied as ten pulses of 470 nm light (each of 1 ms duration) as a 10 Hz train at the recording site through a 60x objective by a light-emitting diode (Cool LED pE4000). PPRs (peak amplitude evoked by 2<sup>nd</sup> stimulus/peak amplitude evoked by 1<sup>st</sup> stimulus) were calculated from an average of 4 sweeps and only for dopamine responses > 25 pA. Optogenetic stimulation was applied every 2 min for all dopamine release measurements or every 10 s for extracellular field recordings. The 1<sup>st</sup> peak of the 1<sup>st</sup> response evoked by a 10 Hz train of optogenetic stimulation was used to calculate 20%–80% rise times, and only amplitudes > 25 pA were used for rise time measurements. For extracellular field recordings, optogenetic stimulation was either

applied as 10 pulses of 470 nm light at 10 Hz or as 40 pulses at 40 Hz. 1  $\mu$ M TTX (Tocris, Catalogue No.# 1078) was used to inhibit sodium channels and action potential firing.

**KCl stimulation** was done using a solution containing (in mM) 100 KCl, 1.3 MgSO<sub>4</sub>, 50 NaCl, 2 CaCl<sub>2</sub> (unless mentioned otherwise), 12 glucose, 10 HEPES (pH 7.3, 300–310 mOsm). KCl was puffed onto the dorsolateral striatum for 10 s at 9  $\mu$ l/s using a syringe pump (World Precision Instruments) and recordings were done in ACSF (unless mentioned otherwise). The peak amplitude of the dopamine response was quantified, and the area under the curve was measured from the start of the KCl puff for 50 s. Only one KCl puff was applied per slice except for [Figures S1I](#) and [S1J](#). For assessing the Ca<sup>2+</sup>-dependence of KCl-evoked dopamine release ([Figures S1I](#) and [S1J](#)), the 0 mM Ca<sup>2+</sup> KCl puff solution contained (in mM): 100 KCl, 3.3 MgSO<sub>4</sub>, 50 NaCl, 1 mM EGTA, 12 glucose, 10 HEPES (pH 7.3, 300–310 mOsm), and was puffed onto the recording site. Slices were perfused with 0 mM Ca<sup>2+</sup> ACSF containing (in mM): 126 NaCl, 3.3 MgSO<sub>4</sub>, 26.2 NaHCO<sub>3</sub>, 2.5 KCl, 1 EGTA, 1 NaH<sub>2</sub>PO<sub>4</sub>, 12 glucose, (pH 7.4, 300–310 mOsm) during recording. Slices were either incubated in 2 mM Ca<sup>2+</sup> (regular) ACSF or 0 mM Ca<sup>2+</sup> ACSF for at least 1 h prior to the start of the recordings. Slices incubated in 2 mM Ca<sup>2+</sup> containing ACSF received two 2 KCl puffs separated by an interval of 15 min, and both KCl puff solutions contained 2 mM Ca<sup>2+</sup> and no EGTA. Slices incubated in 0 mM Ca<sup>2+</sup> ACSF, the first KCl puff was done with 0 mM Ca<sup>2+</sup> KCl puff and recording was done in 0 mM Ca<sup>2+</sup> ACSF. Slices were then perfused for 15 min with 2 mM Ca<sup>2+</sup> ACSF and a second KCl puff with 2 mM Ca<sup>2+</sup> followed. To assess whether cholinergic triggering contributes to KCl-induced release, the response to a single puff of 100 mM KCl in slices incubated in ACSF, slices incubated with 1  $\mu$ M DH $\beta$ E, or slices incubated with 1  $\mu$ M DH $\beta$ E + 1  $\mu$ M TTX (Tocris, Catalogue No.# 1078) for at least 15 min was measured.

**Extracellular field potential recordings** were used to record dopamine axon action potential firing as described before ([Banerjee et al., 2020](#); [Liu et al., 2018](#)) and were performed with ACSF filled glass pipettes (2–3  $\mu$ m tip diameter) placed 20–60  $\mu$ m below the slice surface in areas of dorsolateral striatum with uniform citrine fluorescence. Optogenetic stimulation was applied as a 10 Hz train or a 40 Hz train every 10 s and 100 sweeps were averaged for quantification. Sodium channels were blocked using 1  $\mu$ M TTX (Tocris, Catalogue No.# 1078) and extracellular potentials evoked by 10 Hz trains were recorded before and after TTX. To quantify the reduction by TTX, the amplitude evoked by the first stimulus of the 10 Hz train before and after TTX was analyzed.

### Immunostaining of brain sections

Male and female mice (104–205 d old) were deeply anesthetized with 5% isoflurane. Transcardial perfusion was performed with ice-cold 30–50 mL phosphate buffer saline (PBS) and brains were fixed by perfusion with 50 mL of 4% paraformaldehyde in PBS (4% PFA) at 4°C. Brains were dissected out and incubated in 4% PFA for 12–16 h followed by dehydration in 30% sucrose + 0.1% sodium azide in PBS overnight or until they sank to the bottom of the tube. 20  $\mu$ m thick coronal striatal sections were cut using a vibratome (Leica, VT1000s) in ice-cold PBS. Next, antigen retrieval was performed by incubating slices overnight at 60°C in 150 mM NaCl, 0.05% Tween 20, 1 mM EDTA, 10 mM Tris Base, pH 9.0. Slices were washed in PBS for 10 min and incubated in PBS containing 10% goat serum and 0.25% Triton X-100 (PBST) for 1 h at room temperature. For ELKS2 staining only, coronal striatal sections were incubated in Image-iT FX Signal Enhancer (Thermo Fisher Scientific, Catalogue No. I36933) for 30 min at room temperature, followed by washing twice with PBST (each for 10 min) before blocking. Slices were incubated with primary antibodies for 8–12 h at 4°C, and the following primary antibodies were used in PBST: mouse monoclonal IgG2a anti-Bassoon (1:500, A85, RRID: AB\_11181058), guinea pig polyclonal anti-TH (1:1000, A111, RRID:AB\_2619897), rabbit polyclonal anti-TH (1:1,000, A66, RRID: AB\_390204), rabbit polyclonal anti-ELKS2 $\alpha$  (1:50, A136, custom made, bleed 5 of serum E3-1029, [Held et al., 2016](#)) and rabbit monoclonal anti-GFP (1:2,000, A195, RRID:AB\_2536526). Slices were washed thrice in PBST each for 10 min and incubated in secondary antibodies for 2 h at room temperature in PBST. Secondary antibodies used were goat anti-mouse IgG2a Alexa 488 (1:500, S8, RRID:AB\_2535771), goat-anti guinea pig Alexa 568 (1:500, S27, RRID:AB\_2534119) and goat anti-rabbit Alexa 488 (1:500, S5, RRID:AB\_2576217). Sections were washed thrice in PBST each for 10 min to wash off excess secondary antibodies and mounted on Poly-D-lysine coated #1.5 cover glasses (GG-18–1.5-pdl, neuVITro) with H-1000 mounting medium (Vectashield). At all times during perfusion, staining and mounting, the experimenter was blind to the genotype of the mice.

### 3D-SIM image acquisition and analysis

Image acquisition and analyses were done essentially as described before ([Banerjee et al., 2020](#); [Liu et al., 2018](#); [Gustafsson et al., 2008](#)) using a DeltaVision OMX V4 Blaze structured illumination microscope (GE Healthcare) with a 60X oil immersion objective (PLAN APO, NA 1.42) and Edge 5.5 sCMOS cameras (PCO) for each channel. 488 nm and 568 nm lasers were used for sequential imaging where each laser was controlled with high-speed galvo shutters (200  $\mu$ s switching time). The filter sets used were: 477  $\pm$  2 nm excitation (bandwidth 32  $\pm$  2 nm)/528  $\pm$  2 nm emission (bandwidth 48  $\pm$  2 nm); 571  $\pm$  2 nm excitation (bandwidth 19  $\pm$  2 nm)/609  $\pm$  2 nm emission (bandwidth 37  $\pm$  2 nm) filters. The DeltaVision OMX software was used for image acquisition. Z stacks were acquired in the dorsolateral striatum with a 125 nm step size and 15 raw images were obtained per plane (five phases, three angles). Immersion oil matching was used to minimize spherical aberration. A control slide with TH axonal staining in red and green fluorophores was used to measure lateral shift between green and red channels. A calibration image was generated from this control slide and all images were reconstructed using this calibration to reduce lateral shifts between fluorophores. All 3D-SIM raw images were aligned and reconstructed to obtain superresolved images. Image volumes (40  $\times$  40  $\times$  6  $\mu$ m<sup>3</sup>) were acquired from 7 to 8 regions within the dorsolateral striatum in 4–5 coronal sections for each animal. For detection of Munc13-1 within TH axons, anti-GFP antibodies were used to visualize Munc13-1 in homozygote mice in which Munc13-1 is endogenously tagged with EYFP mice ([Kalla et al., 2006](#)), and



age-matched wild-type mice were used as negative controls. The intensity range for Munc13-1 puncta was determined from reconstructed images, and multiple intensity thresholds within this range were used to generate masks of Munc13-1 puncta, and settings in which Munc13-1 masks best matched original images irrespective of their relationship to TH were chosen for quantification by an investigator blind to the genotype of the mice, and the same thresholds were then used for the full dataset. For image analyses, regions of interest (ROIs) ranging from  $20 \times 20 \times 2.5 \mu\text{m}^3$  to  $36 \times 36 \times 3.6 \mu\text{m}^3$  were selected manually in each z stack of Munc13-1-EYFP and wild-type images. To characterize TH and Munc13-1 signals, size thresholds ( $0.04\text{--}20 \mu\text{m}^3$  for TH axons,  $0.003\text{--}0.04 \mu\text{m}^3$  for Munc13-1) were applied. For detection of Bassoon and ELKS2 within TH axons in Munc13 control and Munc13 cKO<sup>DA</sup> mice and detection of Bassoon within TH axons in Liprin- $\alpha$  control and Liprin- $\alpha$  cKO<sup>DA</sup> mice, ROIs were generated using Otsu intensity and size thresholding parameters ( $0.04\text{--}20 \mu\text{m}^3$  for TH axons,  $0.003\text{--}0.04 \mu\text{m}^3$  for Bassoon and ELKS2). The overlap of Munc13-1, Bassoon and ELKS2 with TH axon was quantified using a custom written MATLAB code (Liu et al., 2018), available at <https://zenodo.org/record/5576635>. The volume occupied by TH for each image was quantified and divided by the total image volume. This was followed by skeletonization of TH signals using 3D Gaussian filtering and a homotypic thinning algorithm to calculate TH axon length. Munc13-1, Bassoon and ELKS2 objects were considered to be within TH when there was > 40% overlap, as established before (Liu et al., 2018). For quantification of Munc13-1 clusters, density and volume occupied by Munc13-1 objects per image volume were calculated. Density and volume of Munc13-1 objects within TH was quantified, and compared to the average of the same parameters after shuffling each object within  $1 \times 1 \times 1 \mu\text{m}^3$  for 1000 times. For quantitative assessment of TH axon shape, a custom code was generated (available at <https://zenodo.org/record/5576622>). A machine learning model was trained with annotation of 15 images per genotype for detection of TH positive objects versus background. All images were next processed in a 3D-smoothing operation followed by thresholding on blurred probability maps. The central axis, the radius and total surface area for each axonal segment was computed. The proportion of surface area at a specific distance from the central axis, in  $0.04 \mu\text{m}$  increments, were compared between Munc13 control and Munc13 cKO<sup>DA</sup>, and Liprin- $\alpha$  control and Liprin- $\alpha$  cKO<sup>DA</sup> mice. Sample images were generated using Imaris 9.0.2 (Oxford Instruments) from masked images obtained from the custom analysis code. Adjustments of contrast, intensity and surface rendering were done identically for each condition for illustration, but after quantification. For all 3D-SIM data acquisition and analyses, the experimenter was blind to the genotype of the mice.

### Generation of conditional Munc13-1 knockout mice

Mice with a floxed exon 21 of the Munc13-1 gene were generated by homologous recombination in 129/Ola embryonic stem (ES) cells according to standard protocols. The targeting vector was generated by recombineering and subcloning from a bacterial artificial chromosome (BAC; BMQ-441L13) of a 129SV ES cell DNA BAC library, and a Herpes Simplex Virus Thymidine kinase (HSV-TK) and a neomycin resistance cassette were used as negative and positive selection markers, respectively. ES cell clones were analyzed by Southern blotting of HindIII-digested genomic DNA, and positive ES cell clones were injected into blastocysts to obtain chimeric mice. Flp deleter-mice (Farley et al., 2000) were used to generate the Munc13-1 floxed mice. Genotyping was performed by PCR using the following reactions: Munc13-1 wild type allele with 27123 + 27122 yielding a 149 bp band; Munc13-1 knock-in allele (ki) after homologous recombination with 27121 + 27122 yielding a 196 bp band; Munc13-1 floxed allele after flp-mediated excision of the neomycin resistance cassette with 27123 + 27122 yielding a 253 bp band; Munc13-1 cKO allele after cre-mediated recombination with 27124 + 27122 yielding a 209 bp band. For whole brain western blotting and electrophysiological assessment of synaptic transmission in autaptic neurons, Munc13-1 floxed mice were crossed to Ella-cre mice for germline recombination (Lakso et al., 1996) to produce constitutive Munc13-1 cKO<sup>gl</sup> mice. For rtPCR, total RNA was isolated from wild-type and Munc13-1 cKO<sup>gl</sup> P0 mouse brains using the Direct-zol RNA Miniprep Kit and reverse transcribed into double-stranded-cDNA by the SuperScript Double-Stranded cDNA Synthesis Kit. PCR reactions were performed using the proofreading VELOCITY DNA polymerase and the primer pairs 24609/34504 (exon 20-23: wt: 486 bp;  $\Delta$ e21: 286 bp;  $\Delta$ e21+22: 135 bp) and 24609/34505 (exon 20-25: wt: 679 bp;  $\Delta$ e21: 515 bp;  $\Delta$ e21+22: 364 bp). The sequences of the PCR products obtained from the different splice variants were verified by directly sequencing the purified PCR products and after cloning them into a TOPO TA cloning vector.

### Immunoblotting

To estimate Munc13-1 levels after gene targeting of Munc13-1, western blots were performed from whole brain homogenates of P0 Munc13-1 wild-type Munc13-1<sup>fl/fl</sup> littermates, and 5  $\mu\text{g}$  from each sample were loaded onto a 3%–8% Tris-acetate gradient gel. To compare Munc13 expression in whole brain homogenates of different Munc13 mouse mutants, 20  $\mu\text{g}$  protein per sample was separated on a 7.5% gel. Residual Munc13-1 expression was estimated in whole brain homogenates from Munc13-1 cKO<sup>gl</sup> animals and Munc13-1 wild-type littermates. 20  $\mu\text{g}$  of total protein from Munc13-1 cKO<sup>gl</sup> and varying amounts (0.7  $\mu\text{g}$ , 1.3  $\mu\text{g}$ , 2  $\mu\text{g}$ ) from Munc13-1 wild-type homogenates were loaded into separate lanes of a 3%–8% Tris-acetate gel. After the transfer, protein bound to nitrocellulose membranes was visualized with MemCode. Membranes were destained and then washed with TBS buffer (10 mM Tris-HCl, 150 mM NaCl, pH 7.5), incubated with blocking buffer (TBS, 5% (w/v) milk powder, 5% (v/v) goat serum, 0.1% (v/v) Tween-20) for 30 min, incubated with primary antibodies for 1 h at room temperature, washed in TBST buffer (Tris-Buffered Saline with 0.1% v/v Tween 20), and incubated with secondary antibodies conjugated to horseradish peroxidase (goat anti-Mouse IgG (H+L), Jackson ImmunoResearch, Cat#115-035-146, RRID:AB\_2307392; goat anti-Rabbit IgG (H+L), Jackson ImmunoResearch, Cat#111-035-144, RRID: AB\_2307391). After several washing steps in TBST and TBS, immunoreactive bands were visualized with an enhanced chemiluminescence (ECL) detection system on film. The following primary antibodies were used: rabbit polyclonal anti-Munc13-1

(1:1000, N-terminal #40, Cooper et al., 2012; Varoquaux et al., 2005); rabbit polyclonal anti-Munc13-1 (1:250, C-terminal #N395, Betz et al., 1997); rabbit polyclonal anti-Munc13-1 (1:1,000, SySy #126103, N-terminal RRID:AB\_887733), mouse monoclonal anti- $\beta$ -Tubulin (1:5,000, Sigma-Aldrich #T4026, RRID:AB\_477577). For estimation of protein amounts, films and stained nitrocellulose membranes were scanned and analyzed using ImageJ (Schindelin et al., 2012). Protein levels were normalized to the total protein amount in the sample as measured by the MemCode stain using the tracing tool. Protein bands from films were manually outlined and the signal intensity was measured. The signal intensity of the band was normalized to the total protein in the respective lane. For experiments estimating residual Munc13-1 expression, the normalized averages of the 0.7  $\mu$ g/lane and 1.3  $\mu$ g/lane Munc13-1 wild-type samples were compared to 20  $\mu$ g/lane Munc13-1 cKO<sup>fl</sup> samples.

For assessment of expression of RIM1 rescue constructs, a separate cohort of 18 RIM cKO<sup>DA</sup> mice (postnatal d 33–54) were bilaterally injected with AAV5 expressing RIM1-Zn, RIM1- $\Delta$ Zn, RIM1-Zn + RIM1- $\Delta$ Zn, RIM1-ZnC<sub>2</sub>B, RIM1-ZnC<sub>2</sub>B<sup>KE</sup> or RIM1-ZnPCP in the SNc midbrain. 3 RIM cKO<sup>DA</sup> mice were bilaterally injected for each RIM1 rescue condition and 3 uninjected littermate RIM cKO<sup>DA</sup> were used as controls. 35–66 d after surgery, mice were deeply anesthetized with isoflurane, decapitated, and both striata of each mouse were dissected in ice cold phosphate-buffered saline (PBS). After dissection, the striata were flash-frozen in dry ice and ethanol and stored in  $-80^{\circ}\text{C}$ . For each condition, the 6 dissected striata were pooled and homogenized with a glass-Teflon homogenizer in 1 mL of homogenizing buffer (50 mM HEPES, 150 mM NaCl, 1 mM EDTA + mammalian protease inhibitor cocktail (Sigma CAT# P8340)) with 30 slow strokes on ice. The homogenized tissue was incubated in lysis buffer (0.2% SDS, 1% Triton X-100, 1% deoxycholate) at  $4^{\circ}\text{C}$  for 1 h and then sonicated twice at  $4^{\circ}\text{C}$  (each for 10 s). Next, sonicated samples were centrifuged at 15,000  $\times$  g for 15 min at  $4^{\circ}\text{C}$  and afterward the clear supernatant was collected into open-top polycarbonate tubes (Beckman Catalogue# 343778). Each supernatant was further ultracentrifuged at 55,000 rpm for 1 h (Beckman rotor), followed by addition of SDS to a final concentration of 1% and a final volume of 1.5 ml. The lysate was then boiled at  $95^{\circ}\text{C}$  for 5 min, allowed to cool to room temperature and later run on 10% SDS-PAGE gels using standard protocols. Equal volumes of each sample were loaded (65  $\mu$ l) for HA staining. For synaptophysin, a separate gel was run with 6.5 times less material (10  $\mu$ l). Proteins were transferred to nitrocellulose membranes at 80 V for 6.5 h and checked for transfer efficiency using Ponceau staining. Membranes were blocked for 1 h at room temperature in filtered blocking solution containing 10% non-fat milk/5% goat serum in TBST. Primary antibodies were dissolved in TBST containing 5% non-fat milk/2.5% goat serum. Membranes were incubated with primary antibody overnight at  $4^{\circ}\text{C}$ . The following primary antibodies were used: mouse monoclonal anti-HA (1:500, AB\_10691311, A250) to visualize HA-tag within RIM1 rescue constructs and mouse anti-synaptophysin 1 (1:5,000, A100, RRID: AB\_887824) as a loading control. Next, membranes were washed with TBST (5 washes, each wash for 5 min) and then incubated for 2 h at room temperature with anti-mouse HRP-conjugated secondary antibodies (1:10,000 in TBST containing 5% non-fat milk/2.5% goat serum). After secondary antibody incubation, membranes were washed with TBST (5 washes, each wash for 5 min), and protein bands were visualized using a standard chemiluminescent reagent and exposure to film. Scans of films were adjusted for brightness and contrast with the same settings applied to the entire scan of a given protein of interest for display.

### Generation of autaptic mouse hippocampal neuron cultures

Astroglial feeder monolayer cell cultures were generated from wild-type (C57/N) postnatal day (P0) mouse cortices according to a previously published protocol (Burgalossi et al., 2012). Primary neuron cultures were prepared from neonatal mouse brains that were dissected at P0 in ice-cold Hank's Balanced Salt Solution (HBSS). Both hippocampi were removed and transferred into 500  $\mu$ l of prewarmed Papain solution (DMEM supplemented with 20 units/ml papain; 0.2 mg/ml cysteine; 1 mM CaCl<sub>2</sub>; 0.5 mM EDTA) and incubated for 60 min at  $37^{\circ}\text{C}$ . The digestion of the hippocampi was terminated by incubating the tissue for 15 min in inactivation solution (DMEM supplemented with 2.5 mg/ml BSA; 2.5 mg/ml trypsin inhibitor; and 10% (v/v) FBS). After two medium washes, neurons were dissociated and seeded onto microdot astrocyte feeder islands on glass coverslips (4,000 cells/6 well for electrophysiology, S2E-M). Neurons were maintained in culture medium (Neurobasal-A medium supplemented with 1 $\times$  B27, 2 mM Glutamax, and 100 units/ml penicillin/streptomycin) at  $37^{\circ}\text{C}$  and 5% CO<sub>2</sub>.

### Electrophysiology on neurons in autaptic hippocampal cultures

Autaptic hippocampal neurons from Munc13-1 wild-type and Munc13-1 cKO<sup>fl</sup> littermate mice were whole-cell voltage clamped at *d in vitro* (DIV) 13–16. Neurons were recorded at room temperature in an external bath solution containing (in mM): 140 mM NaCl, 2.4 mM KCl, 10 mM HEPES, 10 mM glucose, 4 mM CaCl<sub>2</sub>, and 4 mM MgCl<sub>2</sub> (320 mOsm/l) pH 7.4. Patch pipettes (2.5–3.8 M $\Omega$ ) were filled with internal solution containing (in mM): 136 mM KCl, 17.8 mM HEPES, 1 mM EGTA, 4.6 mM MgCl<sub>2</sub>, 4 mM NaATP, 0.3 mM Na<sub>2</sub>GTP, 15 mM creatine phosphate, and 5 U/ml phosphocreatine kinase, pH 7.4, 315–320 mOsm. Excitatory postsynaptic currents (EPSCs) were evoked in patched neurons by a 2 ms depolarization to 0 mV. The peak amplitudes for all responses recorded in 10 Hz train across both genotypes was normalized to the mean initial EPSC amplitude of Munc13-1 control. Miniature EPSCs (mEPSCs) were recorded in presence of 300 nM TTX to inhibit action potential firing. 500 mM sucrose was puffed for 7 s to estimate the readily-releasable pool of synaptic vesicles.

### Microdialysis

Microdialysis was performed as described before (Banerjee et al., 2020; Liu et al., 2018). The microdialysis probes (6 kDa MW cut-off, CMA 11, Harvard Apparatus, Catalogue# CMA8309581) were calibrated with freshly made dopamine solutions (0, 100 and 200 nM) dissolved in ACSF before each experiment. After probe calibration, male and female Munc13 control and cKO<sup>DA</sup> mice (55–96 d old)

were anesthetized using 1.5% isoflurane and the probe was inserted into dorsal striatum (coordinates: 1.0 mm anterior, 2.0 mm lateral of bregma, and 3.3 mm below pia) using stereotaxy. A fresh probe was used for each Munc13 control and cKO<sup>DA</sup> mouse. The microdialysis probe was continuously perfused with ACSF containing (in mM): 155 NaCl, 1.2 CaCl<sub>2</sub>, 1.2 MgCl<sub>2</sub>, 2.5 KCl and 5 glucose at a speed of 1  $\mu$ l/min. Dialysates were collected every 15 min and the extracellular dopamine concentration was measured using HPLC (HTEC-510, Amuza Inc) connected to an electrochemical detector (Eicom). Data during the first 75 min were not plotted because during this time window dopamine levels stabilize after surgery. Average dopamine levels from the 76th - 120th min of Munc13 control mice were used to normalize all dopamine values for both genotypes. 10  $\mu$ M TTX dissolved in ACSF was applied using reverse dialysis starting at 121 min to inhibit firing of dopamine axons as described before (Banerjee et al., 2020; Liu et al., 2018). For all microdialysis data acquisition and analyses, the experimenter was blind to the genotype of the mice, and experiments were performed according to approved protocols of the Harvard University Animal Care and Use Committee.

### Striatal synaptosome preparation and immunostaining

Striatal synaptosome preparations were performed as previously described (Banerjee et al., 2020; Liu et al., 2018). Munc13 control and cKO<sup>DA</sup> mice (P42-73) were deeply anesthetized using isoflurane, decapitated, and the brains were harvested into ice-cold PBS. Dorsal striata were dissected out and placed into a pre-cooled, detergent-free glass-Teflon homogenizer filled with 1 mL of ice-cold homogenizing buffer containing (in mM): 4 4-(2-hydroxyethyl)-1-piperazineethanesulfonic acid (HEPES), 320 sucrose, pH 7.4, and 1x of a mammalian protease inhibitor cocktail. The tissue was homogenized with 12 strokes with a detergent-free ice-cold glass-teflon homogenizer. Next, 1 mL of homogenizing buffer was added to the striatal homogenate and it was centrifuged at 1,000 x g for 10 min at 4°C. The supernatant (S1) was collected and centrifuged at 12,500 x g for 15 min at 4°C. The supernatant (S2) was removed and the pellet (P2) was re-homogenized in 1 mL homogenizing buffer with 6 strokes. A sucrose density gradient was prepared with 5 mL of 0.8 M and 1.2 M sucrose in thin wall ultracentrifugation tubes (Beckman Coulter, Cat # 344059). The P2 homogenate was mixed with 1 mL of homogenizing buffer, and 1.5 mL of this was added to the top of the sucrose gradient and was centrifuged at 69,150 x g for 70 min at 4°C (SW 41 Ti Swinging-Bucket Rotor, Beckman Coulter, Cat. # 331362). 1–1.5 mL of the synaptosome layer was collected from the interface of the two sucrose layers. Synaptosomes were diluted 20–30 times in homogenizing buffer and spun (4,000 x g, 10 min) onto Poly-D-lysine coated #1.5 coverslips at 4°C. Excess homogenizing buffer was pipetted out and synaptosomes were fixed using 4% PFA in PBS for 20 min at 4°C. Coverslips were incubated in 3% bovine serum albumin + 0.1% Triton X-100 in PBS at room temperature for 45 min to block non-specific binding and allow for permeabilization. Primary antibody staining was done for 12 h at 4°C, followed by three washes for 15 min each. The primary antibodies used were: mouse monoclonal IgG2a anti-Bassoon (1:1,000, A85, RRID:AB\_11181058), mouse monoclonal IgG1 anti-synaptophysin-1 (1:500, A100, RRID:AB\_887824), rabbit polyclonal anti-RIM1 (1:500, A58, RRID:AB\_887774) and guinea pig polyclonal anti-TH (1:1,000, A111, RRID:AB\_2619897). Secondary antibody staining was done for 2 h at room temperature in blocking solution followed by three washes each for 15 min. The secondary antibodies were: goat anti-mouse IgG2a Alexa 488 (1:500, S8, RRID:AB\_2535771), goat anti-rabbit Alexa 555 (1:500, S22, RRID:AB\_2535849), and goat anti-guinea pig Alexa 633 (1:500, S34, RRID:AB\_2535757).

### Confocal microscopy and image analysis of striatal synaptosomes

Single optical sections of striatal synaptosomes plated on coverslips (105  $\times$  105  $\mu$ m<sup>2</sup>) stained for Bassoon (detected via Alexa 488), RIM1 (detected via Alexa 488 secondaries), synaptophysin-1 (detected via Alexa-555 secondaries) and TH (detected via Alexa 633 secondaries) were imaged with an oil immersion 60X objective and 1.5X optical zoom using an Olympus FV1000 confocal microscope equipped with 488 nm, 559 nm and 635 nm lasers. The filter sets used for confocal imaging were: 488 nm excitation/500-525 nm emission, 561 nm excitation/560-620 nm emission and 635 nm long pass excitation/650 nm emission. Signals were acquired using PMT detectors and Olympus FV-ASW software. For quantification, raw confocal images were analyzed in a custom MATLAB program (Liu et al., 2018) available at <https://doi.org/10.5281/zenodo.5576635>. A total of 300-700 synaptosomes were detected per image using Otsu intensity thresholds and size thresholds (0.2 - 1  $\mu$ m<sup>2</sup> for TH and 0.15 - 2  $\mu$ m<sup>2</sup> for synaptic markers). These threshold settings were identical for each image across Munc13 control and cKO<sup>DA</sup> for detection of synaptophysin-positive (Syp<sup>+</sup>) and TH-positive (TH<sup>+</sup>) ROIs in each image, which was used to generate single and double positive ROIs (Syp<sup>+</sup>TH<sup>+</sup>). For synaptophysin-positive TH-negative ROIs (Syp<sup>+</sup>TH<sup>-</sup>), synaptophysin<sup>+</sup> ROIs which had a TH signal less than the average intensity of all pixels in the image were designated as TH-negative (TH<sup>-</sup>) and were marked as (Syp<sup>+</sup>TH<sup>-</sup>) ROIs. Bassoon intensities within Syp<sup>+</sup>TH<sup>-</sup>, Syp<sup>+</sup>TH<sup>+</sup> ROIs or within all TH<sup>+</sup> ROIs, and RIM1 intensities within all TH<sup>+</sup> ROIs were quantified and frequency distribution histograms were plotted, and synaptophysin intensity within all TH<sup>+</sup> ROIs was quantified. Sample images were generated in Fiji with identical adjustments of brightness and contrast for Munc13 control and cKO<sup>DA</sup>, but image quantification was performed before these adjustments. Image acquisition and quantification were performed by an experimenter blind to the genotype.

### QUANTIFICATION AND STATISTICAL ANALYSIS

Data are shown as mean  $\pm$  SEM (except for mean  $\pm$  SD in Figures 5J and 7E) and all statistics were performed in Graphpad Prism 9. Sample sizes, numerical values of means, medians (where appropriate) and errors, statistical tests, F-ratios of ANOVAs, and exact p values are provided for each experiment in Tables S1–S8, and key information is also included in the figure legends. The number of recorded slices was used as sample size for all slice amperometry data. For electrophysiology in autaptic hippocampal cultures,

sample size was number of recorded cells. For all image data, sample size was the number of images except for frequency histograms in [Figures 5E, S5C, and S5F](#), where sample size was the number of analyzed ROIs. Image data are presented as violin plots with superimposed mean  $\pm$  SEM throughout, except for datasets with  $\leq 40$  images. Wild-type controls in [Figures 2C, 2D, and 2G](#) (in which all values are close to 0) are shown as scatterplots because violin plots would be non-informative. For microdialysis data, sample size was the number of mice. Datasets with sample size  $\geq 30$  were analyzed using parametric statistical tests. For datasets with sample size  $< 30$ , normality was determined with Anderson-Darling, D'Agostino-Pearson, Shapiro-Wilk, or one sample Kolmogorov-Smirnov tests and statistics were performed using non-parametric tests for datasets that did not follow a normal distribution. In all figures, statistical significance is presented as \*  $p < 0.05$ , \*\*  $p < 0.01$ , \*\*\*  $p < 0.001$ .

**Neuron, Volume 110**

**Supplemental information**

**Molecular and functional architecture  
of striatal dopamine release sites**

**Aditi Banerjee, Cordelia Imig, Karthik Balakrishnan, Lauren Kershberg, Noa Lipstein, Riikka-Liisa Uronen, Jiexin Wang, Xintong Cai, Fritz Benseler, Jeong Seop Rhee, Benjamin H. Cooper, Changliang Liu, Sonja M. Wojcik, Nils Brose, and Pascal S. Kaeser**

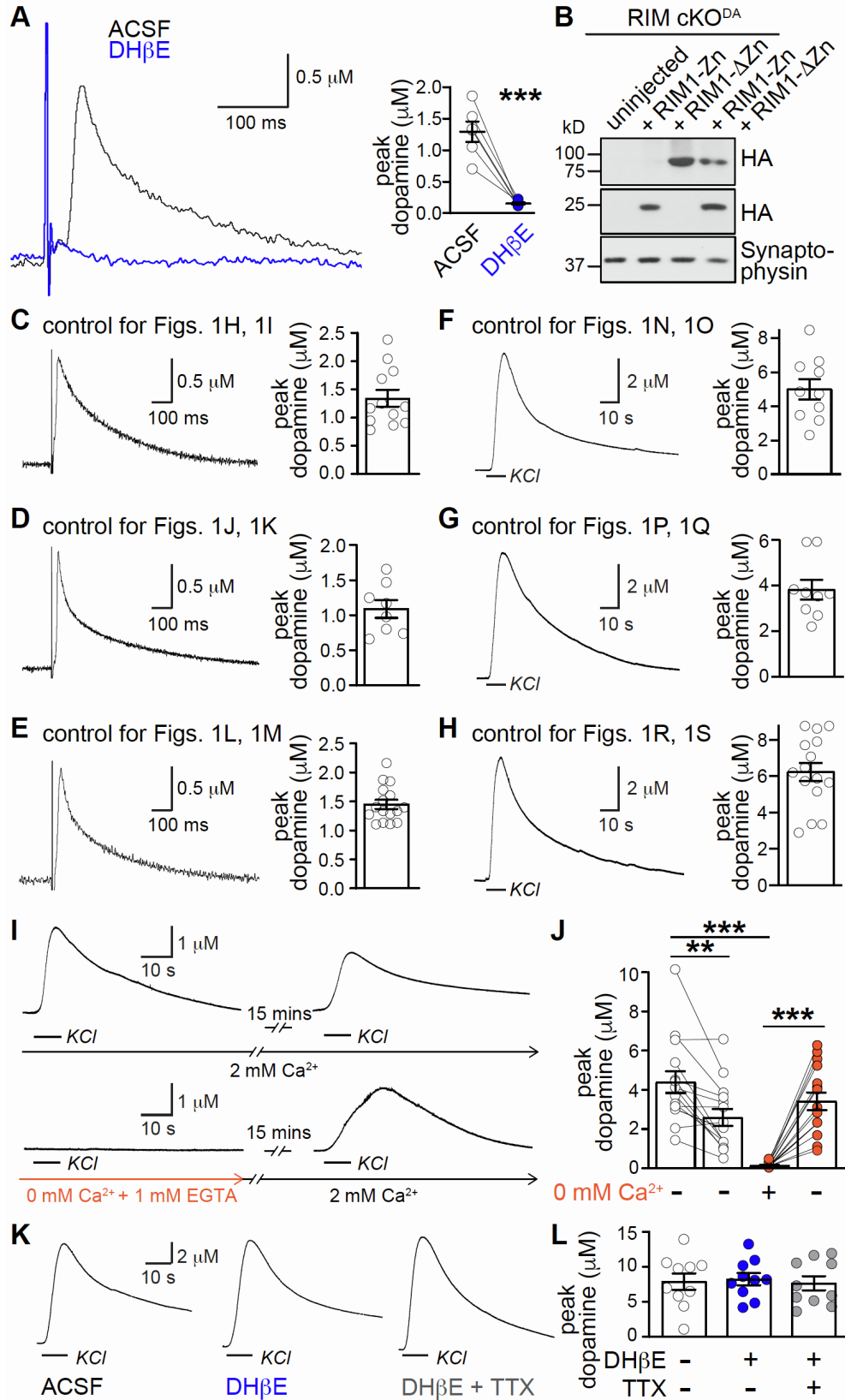


Figure S1. Additional data for RIM rescue experiments and for KCl-triggered release,

**related to Fig. 1**

**(A)** Sample traces (single sweeps) and quantification of dopamine release evoked by a 90  $\mu$ A electrical stimulus in wild type slices before and after application of DH $\beta$ E, 6 slices/3 mice.

**(B)** Western blot of striatal lysates from RIM cKO<sup>DA</sup> mice injected with cre-dependent AAV viruses into the midbrain to assess expression of RIM1-Zn, RIM1- $\Delta$ Zn, or RIM1-Zn + RIM1- $\Delta$ Zn. HA antibodies were used to assess expression of rescue constructs, and synaptophysin antibodies were used to blot for loading on separate gels (with 6.5 times less material).

**(C-E)** Sample traces (single sweeps) and quantification of dopamine release in the dorsolateral striatum evoked by a 90  $\mu$ A electrical stimulus in brain slices of unrelated control mice. For rescue experiments shown in Figs. 1 and 8, stable amperometric recordings were established with unrelated control slices first (using the same carbon fiber) on each day before proceeding with assessment of rescue, C: 12/4; D: 8/3; E: 16/4.

**(F-H)** Same as A-C but for a local 100 mM puff of KCl, F: 10/4; G: 9/3; H: 15/4.

**(I-J)** Sample traces (I) and quantification of peak dopamine amplitudes (J) evoked by 2 consecutive 100 mM KCl-puffs at an interval of 15 min. Slices were incubated either in 2 mM Ca<sup>2+</sup> throughout the experiment or in 0 mM Ca<sup>2+</sup> + 1 mM EGTA containing ACSF for the first pulse and then in 2 mM Ca<sup>2+</sup> for the second pulse, 2/2 mM Ca<sup>2+</sup> 15/4; 0/2 mM Ca<sup>2+</sup> 15/4.

**(K-L)** Sample traces (K) and quantification of peak dopamine (L) evoked by a 100 mM KCl puff in slices of control mice in ACSF, DH $\beta$ E, or DH $\beta$ E + TTX, 10/4 each.

Data are mean  $\pm$  SEM, \*\* p < 0.01, \*\*\* p < 0.001 as assessed by paired t-test in A, repeated measures one-way ANOVA followed Sidak's multiple comparisons tests in J and one-way ANOVA followed Sidak's multiple comparisons tests in L. For numerical values of means and errors, exact p-values and the number of observations used for statistics for this and all following supplementary figures, see corresponding Tables S1-S8.

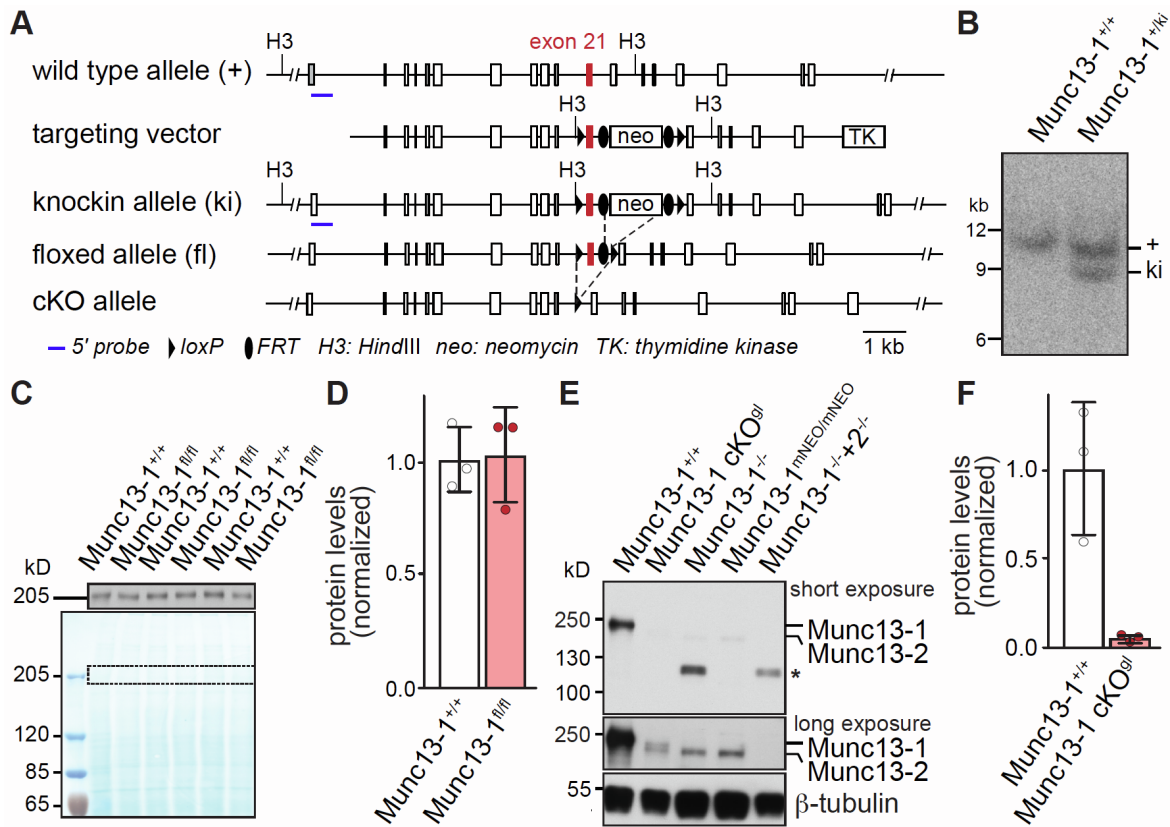


**Figure S2. Generation of Munc13-1 floxed mice, related to Fig. 3**

**(A)** Schematic of the Munc13-1 wild type allele, the targeting vector, the knock-in allele (ki) after homologous recombination, the floxed allele after flp recombinase-mediated excision of the neomycin resistance cassette (neo), and the Munc13-1 cKO allele after cre-mediated recombination. The targeted exon 21 is shown in red. A 5' probe (blue bar) was used for Southern blot in B.

**(B)** Southern blotting after *HindIII* digest of genomic DNA purified from a positive embryonic stem (ES) cell clone produced 9.8 kb Munc13-1 wild type and 8.4 kb Munc13-1 ki band.

**(C, D)** Western blot (C) and estimation of Munc13-1 levels (D) in P0 whole brain homogenates from wild type (*Munc13-1<sup>+/+</sup>*) and homozygote floxed (*Munc13-1<sup>fl/fl</sup>*) littermate mice, 5  $\mu$ g of protein were loaded per lane of a 3-8% gradient Tris-Acetate gel and bands were detected by chemiluminescence. The scanned Western blot (top) and a protein stain of the nitrocellulose membrane (bottom, dotted rectangle indicates the region represented in the upper panel in C),



and estimated Munc13-1 protein levels normalized to total measured protein are shown in D, 3 mice each.

**(E)** Western blot analysis of Munc13-1 levels from E18 or P0 whole brain tissue homogenates from different Munc13-1 knockout mouse lines. Lane 1, wild type (Munc13-1<sup>+/+</sup>); lane 2, homozygote germline recombined allele of the new Munc13-1 floxed (Munc13-1 cKO<sup>gl</sup>) mice; lane 3, Munc13-1 constitutive knockout (Munc13-1<sup>-/-</sup>) published in (Augustin et al., 1999); lane 4, Munc13-1 constitutive knockout (Munc13-1<sup>mNeo/mNeo</sup>) published in (Rhee et al., 2002); lane 5, Munc13-1/Munc13-2 double knockout (Munc13-1<sup>-/-</sup>+2<sup>-/-</sup>) published in (Varoqueaux et al., 2002). Munc13-1 cKO<sup>gl</sup> exhibit a severe reduction of Munc13-1 protein levels comparable to that in well-characterized constitutive Munc13-1 knockout lines. Note that the Munc13-1<sup>-/-</sup> (Augustin et al., 1999) mice express a truncated Munc13-1 protein product (\*) that is detected by antibodies that bind N-terminal epitopes as discussed in Fig. 1 of (Man et al., 2015). A long exposure (middle) reveals that the anti-Munc13 antibody detects a protein band with slightly lower molecular weight in Munc13-1 knockout samples, which corresponds to ubMunc13-2 (Munc13-2) and is absent in the Munc13-1<sup>-/-</sup>+2<sup>-/-</sup> sample. Munc13-1 cKO<sup>gl</sup> animals express very low levels of a Munc13-1 protein product, likely corresponding to a protein lacking both exon 21 and 22, for which transcripts could be detected in brains of Munc13-1 cKO<sup>gl</sup> mice using reverse transcriptase PCR (not shown, see methods).

**(F)** Estimation of Munc13-1 levels in P0 whole brain homogenates from Munc13-1<sup>+/+</sup> and littermate Munc13-1 cKO<sup>gl</sup> mice indicates that the residual Munc13-1 protein is reduced to at most a few % of Munc13-1<sup>+/+</sup> levels, 3 mice each.

Estimated protein levels in D and F are mean ± SEM.

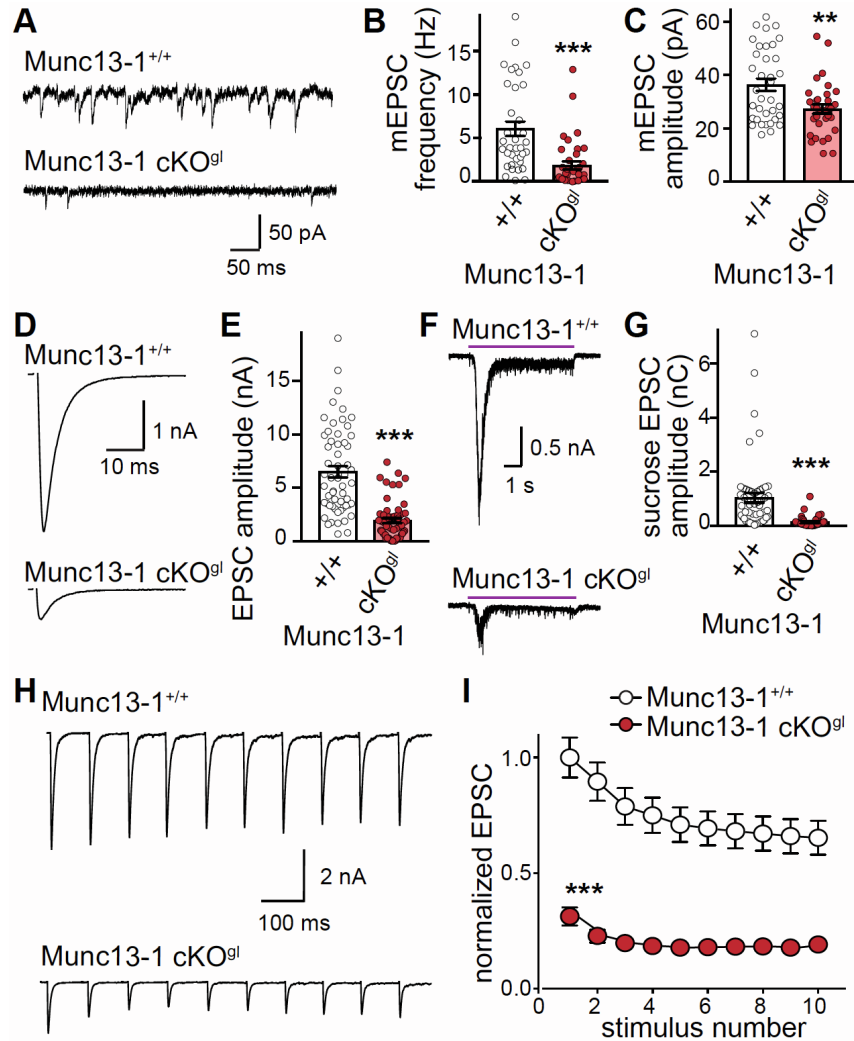


**Figure S3. Munc13-1 deletion strongly impairs neurotransmitter release in autaptic hippocampal cultures, related to Fig. 3**

**(A-C)** Sample traces (A) and quantification of miniature EPSC (mEPSC) frequency (B) and amplitude (C) recorded in presence of tetrodotoxin (TTX). B: Munc13-1<sup>+/+</sup>, 36 neurons/3 independent cultures; Munc13-1 cKO<sup>gl</sup> (homozygote germline recombined mice generated from the new Munc13-1 floxed mice), 39/3; C: Munc13-1<sup>+/+</sup> 36/3; Munc13-1 cKO<sup>gl</sup> 33/3.

**(D, E)** Sample traces (D) and quantification of average EPSC amplitudes (E) evoked by a 2-ms depolarization to 0 mV, Munc13-1<sup>+/+</sup> 57/3; Munc13-1 cKO<sup>gl</sup> 56/3.

**(F, G)** Sample traces (F) and quantification of EPSCs (G) evoked by application of 500 mM sucrose, Munc13-1<sup>+/+</sup> 54/3; Munc13-1 cKO<sup>gl</sup> 53/3.

**(H, I)** Sample traces (H) and quantification (I) of EPSCs triggered by 10 stimuli at 10 Hz.

Quantification in I is shown normalized to the mean of the first EPSC of Munc13-1<sup>+/+</sup>, Munc13-1<sup>+/+</sup> 40/3; Munc13-1 cKO<sup>gl</sup> 44/3.

Data are mean  $\pm$  SEM, \*  $p < 0.05$ , \*\*  $p < 0.01$ , \*\*\*  $p < 0.001$  as assessed by Mann-Whitney tests in B, C, E, G; two-way ANOVA (\*\*\*  $p < 0.001$  for genotype and stimulus number, n.s. for interaction) followed by Sidak's multiple comparisons tests in I (\*\*\*  $p < 0.001$  for all stimuli).

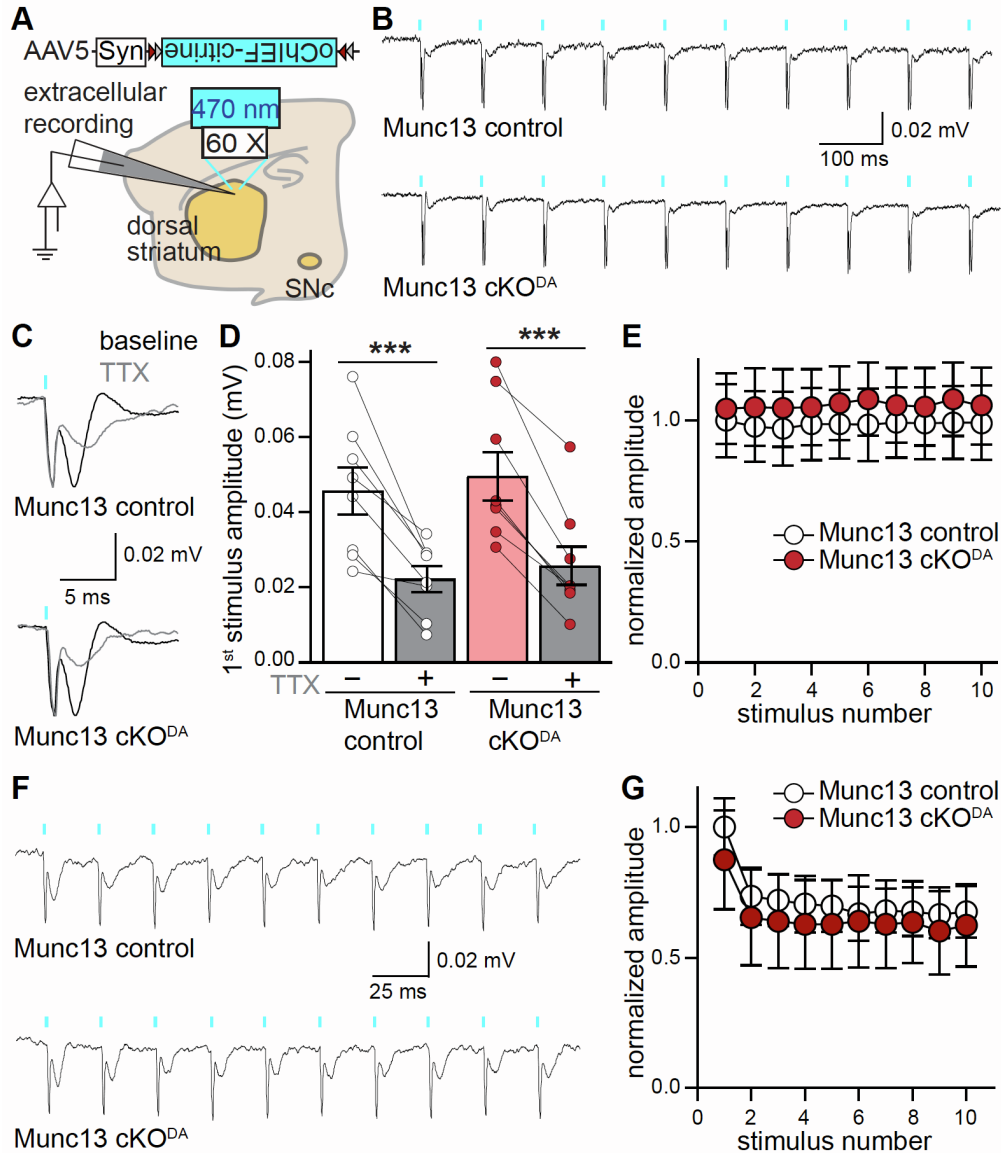


**Figure S4. Dopamine axons of Munc13 cKO<sup>DA</sup> mice fire action potentials, related to Fig. 3**

**(A)** Schematic outlining cre-dependent expression of oChIEF for dopamine neuron activation and recording of extracellular field potentials in dorsolateral striatum.

**(B-E)** Sample traces (B, C, average of 100 sweeps) and quantification (D, E) of extracellular potentials evoked by ten optogenetic stimuli at 10 Hz. In C, the extracellular potential for the first stimulus of a 10-Hz train before (black) and after 1  $\mu$ M TTX (grey) is magnified (the full train in B and the first response in C are from different slices). Quantification of extracellular potential amplitudes evoked by the 1<sup>st</sup> stimulus of a 10 Hz train before and after TTX is shown in D, and

the extent of TTX inhibition is similar between Munc13 control and cKO<sup>DA</sup>. The normalized extracellular potential amplitudes for 10 Hz after normalization to the mean first response amplitude of Munc13 control are shown in E, 8 slices/6 mice each.

**(F, G)** Same as B and E but for the first 10 stimuli of a 40 Hz train. The amplitudes are decreased after the first stimulus because dopamine axons do not reliably follow optogenetic activation at frequencies above 20 Hz (Liu et al., 2018), 6/5 each.

Data are mean  $\pm$  SEM, \*\*\*  $p < 0.001$  as assessed by repeated measures one-way ANOVA followed by Sidak's multiple comparisons tests in D; two-way ANOVA (n.s. for genotype, stimulus number and interaction) in E; two-way ANOVA (\*\*\*  $p < 0.001$  for stimulus number, n.s. for genotype and interaction) in G.

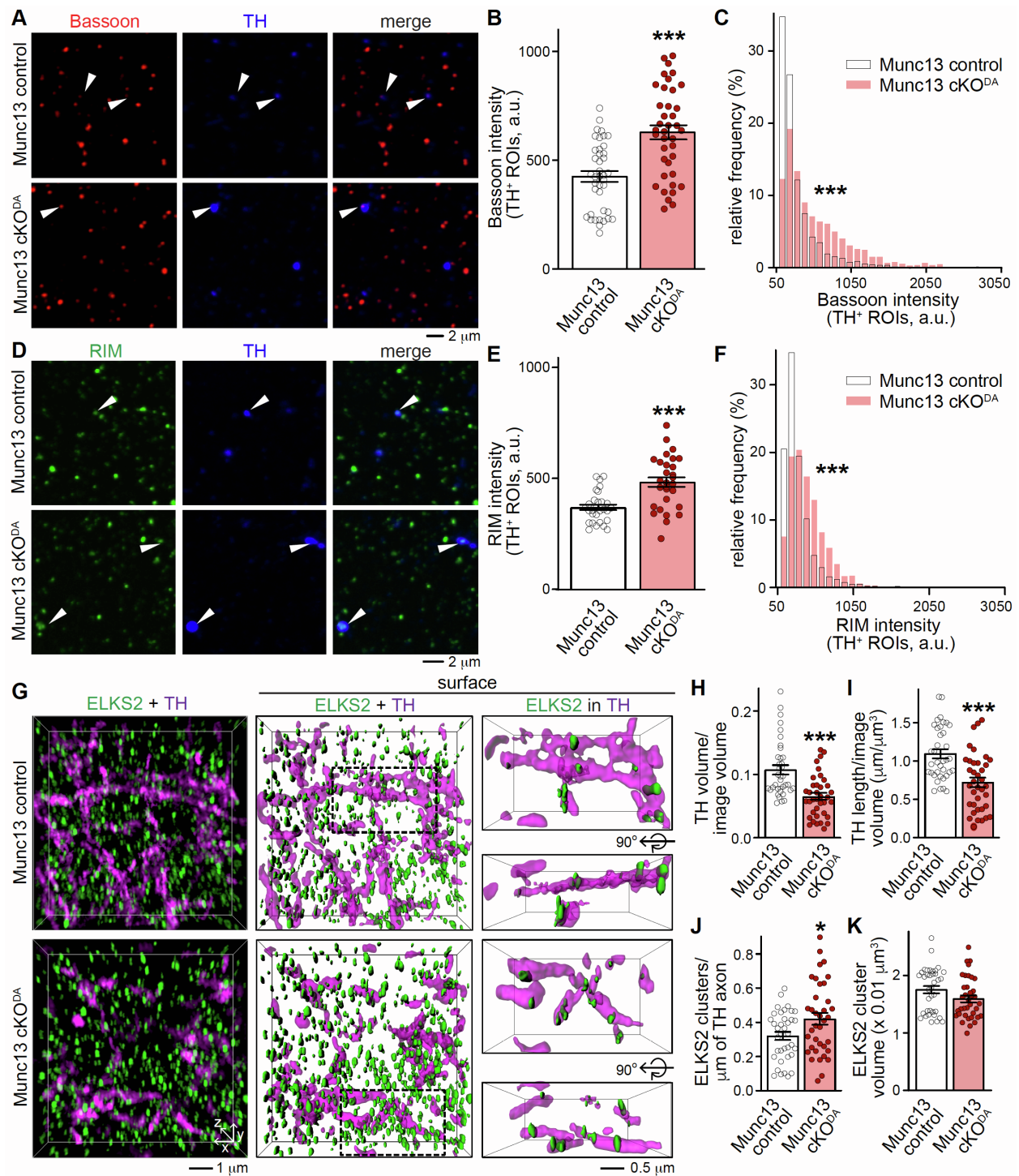


**Figure S5. Dopamine axon and release site structure after Munc13 ablation, related to**

**Fig. 5**

(A-C) Sample confocal images (A) and quantification (B, C) of striatal synaptosomes stained for the active zone marker Bassoon and the dopamine axon marker TH. Quantification of Bassoon

intensity within TH<sup>+</sup> ROIs pooled by images (B) and frequency distribution histogram for all Bassoon intensities within TH<sup>+</sup> ROIs (C) are shown, B: Munc13 control 40 images/4 mice; Munc13 cKO<sup>DA</sup> 39/4; C: Munc13 control 3035 ROIs/40 images/4 mice, Munc13 cKO<sup>DA</sup> 1745/39/4.

**(D-F)** Sample confocal images (D) and quantification (E, F) of striatal synaptosomes stained for the active zone scaffold RIM (green) and the dopamine axon marker TH (blue). Quantification of RIM intensity within TH<sup>+</sup> ROIs pooled by images (E) and frequency distribution histogram for RIM intensities within TH<sup>+</sup> ROIs (F) are shown, E: 29 images/3 mice each; F: Munc13 control 4766 ROIs/29 images/3 mice, Munc13 cKO<sup>DA</sup> 1639/29/3.

**(G)** Sample 3D-SIM images of dorsolateral striatum stained for ELKS2 and TH. Volume rendered images (left, 10 x 10 x 2  $\mu\text{m}^3$ ) with all ELKS2; surface rendering of the same images with all ELKS2 (middle) and magnified views (right, 5 x 3 x 2  $\mu\text{m}^3$ , frontal view and rotated by +90° along the x axis) of only ELKS2 within TH (> 40% volume overlap) are shown.

**(H-K)** Quantification of the experiment shown in G displaying TH volume per image (H), TH axon length per image volume (I), density (J) and volume (K) of ELKS2 clusters (J) localized within TH axons (> 40% volume overlap), 37 images/3 mice each.

Data are mean  $\pm$  SEM, \*  $p < 0.05$ , \*\*\*  $p < 0.001$  as assessed by unpaired t-tests in B, E, H, I, J, K and Kolmogorov-Smirnov tests in C, F.

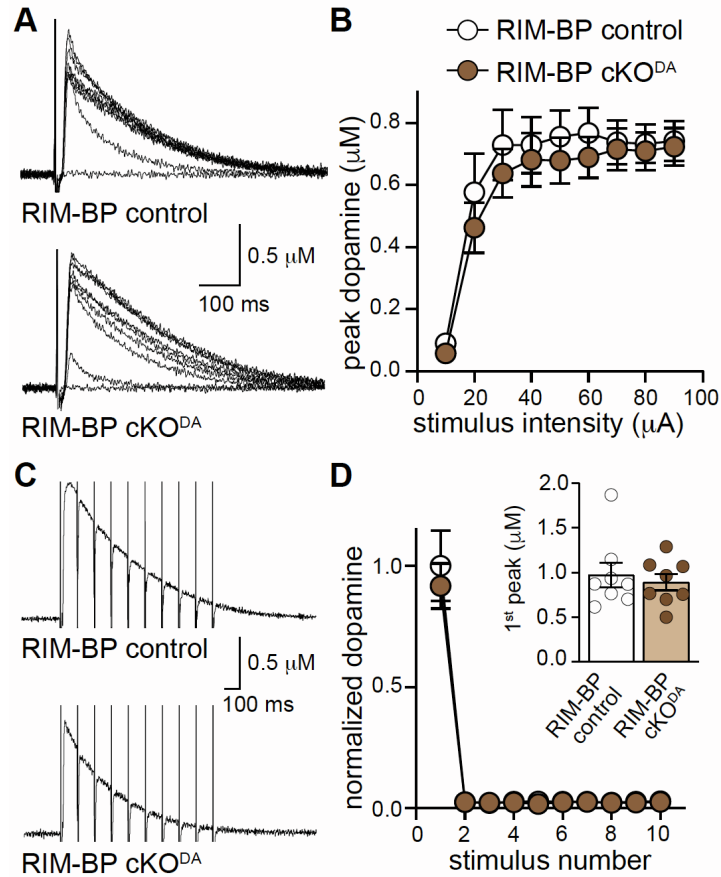


**Figure S6. Ablation of RIM-BP1 and RIM-BP2 does not detectably impair electrically evoked dopamine release, related to Fig. 6**

**(A, B)** Sample traces (A, single sweeps) and quantification of peak amplitudes (B) of dopamine release evoked by electrical stimulation (10-90  $\mu$ A single electrical pulses at increasing stimulation intensities), 16 slices/5 mice each.

**(C, D)** Sample traces (C, average of 4 sweeps) and quantification of peak amplitudes (D) of dopamine release normalized to the first peak amplitude of RIM-BP control in response to 10 stimuli at 10 Hz train, inset in D shows the peak dopamine amplitude for 1<sup>st</sup> stimulus, 8/4 each. Data are mean  $\pm$  SEM, \*\*\*  $p < 0.001$  as assessed by two-way ANOVA (\*\*\* for stimulus, n.s. for genotype and interaction) followed by Sidak's multiple comparisons tests in B, D and Mann-Whitney test for inset in D.



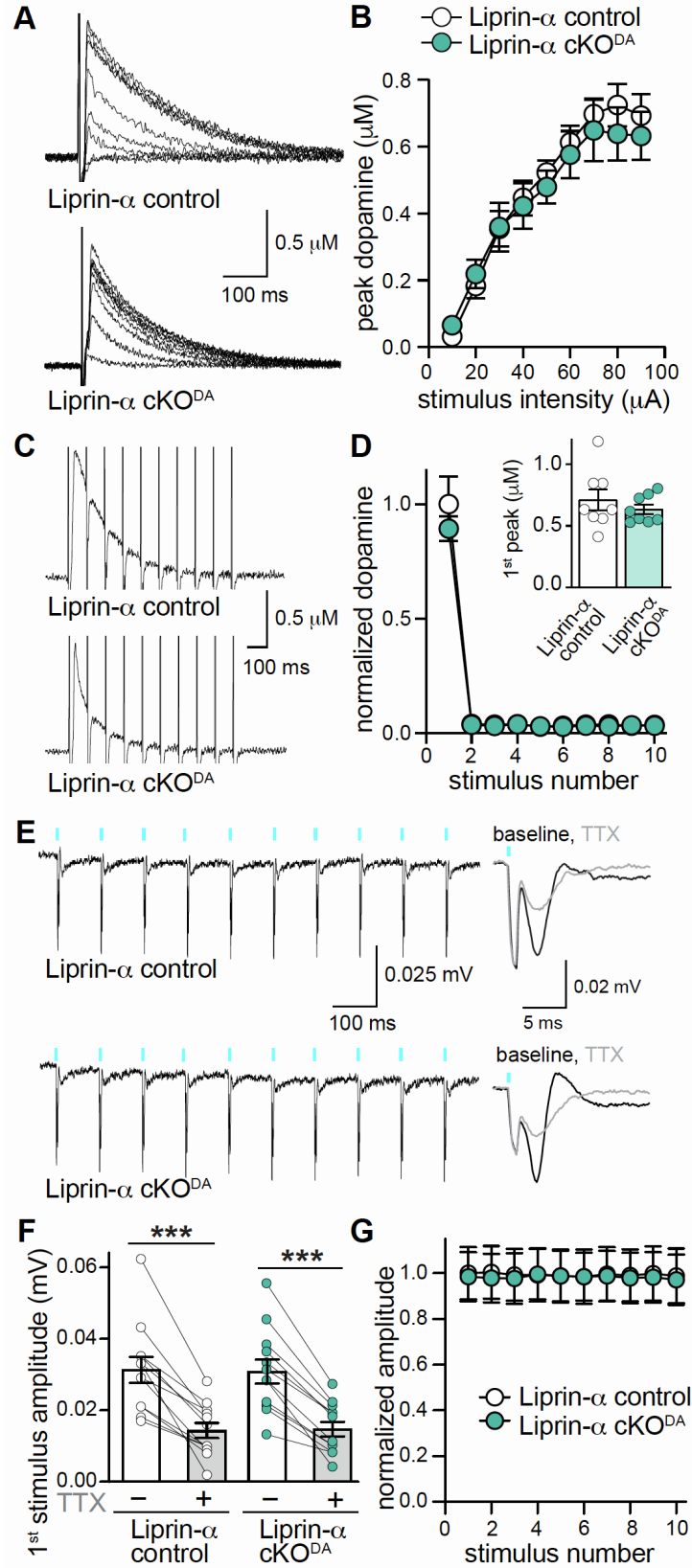


Figure S7. Additional electrophysiological characterization of Liprin- $\alpha$  cKO<sup>DA</sup> mice,

**related to Fig. 7**

**(A, B)** Sample traces (A, single sweeps) and quantification of peak amplitudes (B) of dopamine release evoked by electrical stimulation (10-90  $\mu$ A single electrical pulses at increasing stimulation intensities), 12 slices/8 mice each.

**(C, D)** Sample traces (C, average of 4 sweeps) and quantification of peak amplitudes (D) of dopamine release normalized to the first peak amplitude of Liprin- $\alpha$  control in response to 10 electrical stimuli at 10 Hz train, inset in D shows the peak dopamine amplitude for the 1<sup>st</sup> stimulus, 8/3 each.

**(E-G)** Sample traces (E, average of 100 sweeps) and quantification (F, G) of extracellular potentials evoked by 10 stimuli at 10 Hz of optogenetic stimulation. In E (inset, right), the extracellular potential for the first stimulus of a 10-Hz train before (black) and after 1  $\mu$ M TTX (grey) is magnified, the full train (left) and inset (right) are from different slices. Quantification of extracellular potential amplitudes evoked by the 1<sup>st</sup> stimulus of a 10 Hz train before and after TTX is shown in F, and the extent of TTX inhibition is similar between Liprin- $\alpha$  control and cKO<sup>DA</sup>. The normalized extracellular potential amplitudes for 10 Hz after normalization to the mean first response amplitude of Liprin- $\alpha$  control are shown in G, 12/3 each.

Data are mean  $\pm$  SEM, \*\*  $p < 0.01$ , \*\*\*  $p < 0.001$  as assessed by two-way ANOVA (\*\*\*) for stimulus intensity/stimulus number, n.s. for genotype, interaction) followed by Sidak's multiple comparisons tests in B, D;  $p > 0.05$  unpaired t-test for inset in D; or repeated measures one-way ANOVA in F followed by Sidak's multiple comparisons tests for specific pairs; and two-way ANOVA (n.s. for genotype, stimulus and interaction) in G.

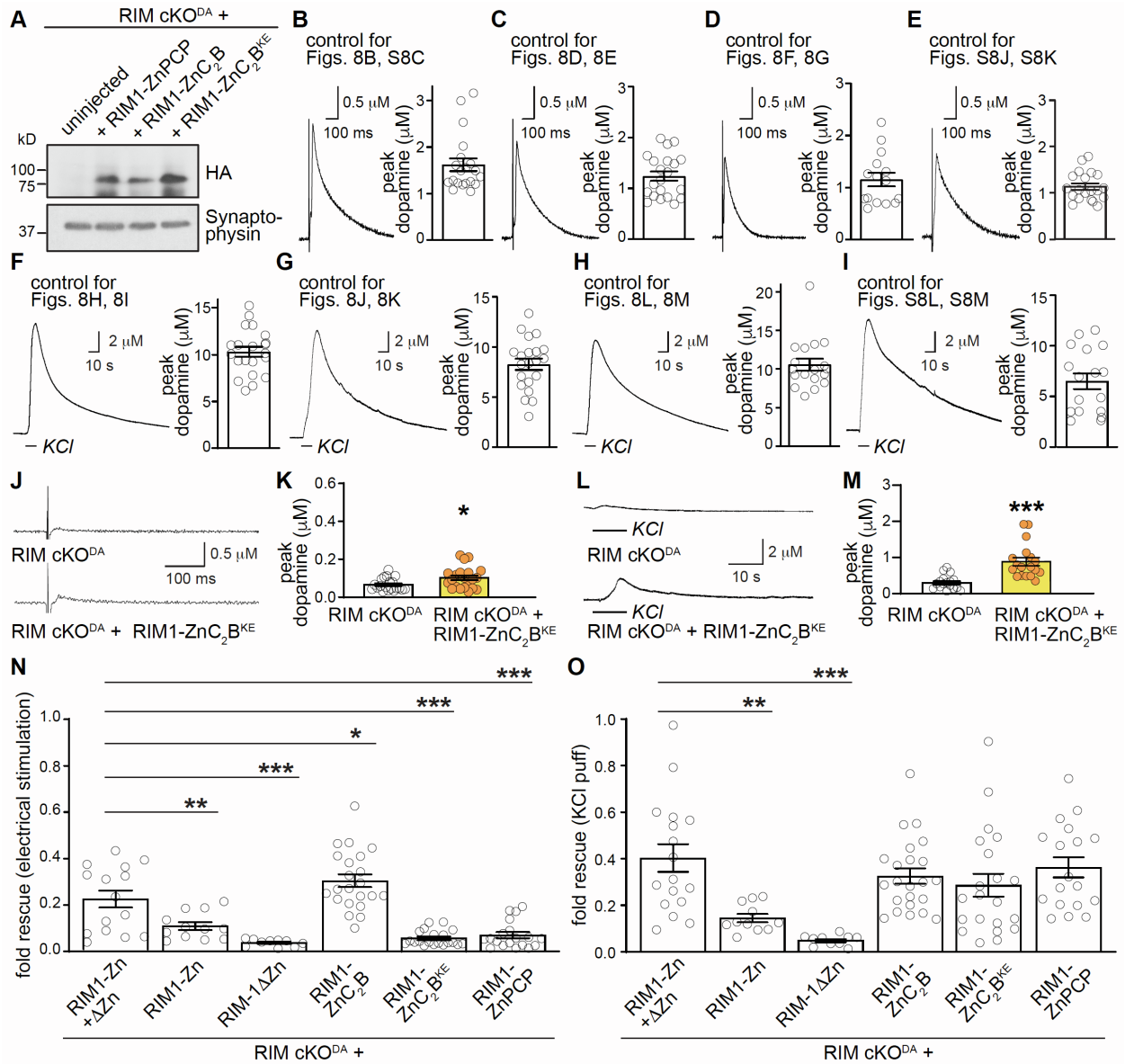


**Figure S8. Control recordings and expression analyses for rescue experiments and comparison of rescue efficacies, related to Fig. 8**

**(A)** Western blot of striatal lysates from RIM cKO<sup>DA</sup> mice injected with cre-dependent AAV viruses into the midbrain to assess expression of RIM1-ZnPCP, RIM1-ZnC<sub>2</sub>B, and RIM1-ZnC<sub>2</sub>B<sup>KE</sup>. HA antibodies were used to assess expression of rescue constructs, and synaptophysin antibodies were used to blot for loading on separate gels (with 6.5 times less material).

**(B-E)** Sample traces (single sweeps) and quantification of dopamine release in the dorsolateral

striatum evoked by a 90  $\mu$ A electrical stimulus in brain slices of unrelated control mice recorded on the same days as the experiment shown in Figs. 8 and S8, B: 20 slices/4 mice; C: 21/5; D: 15/4; E: 20/4.

**(F-I)** Same as B-E but for a local 100 mM KCl-puff, F: 21/4; G: 21/5; H: 18/4; I: 17/4.

**(J, K)** Sample traces (single sweeps, J) and quantification of peak dopamine (K) evoked by a 90  $\mu$ A electrical stimulus in brain slices, RIM cKO<sup>DA</sup> 20/4; RIM cKO<sup>DA</sup> + RIM1-ZnC<sub>2</sub>B<sup>KE</sup> 21/4.

**(L, M)** Sample traces (L) and quantification (M) of peak dopamine evoked by a local 100 mM KCl-puff, RIM cKO<sup>DA</sup> 17/4; RIM cKO<sup>DA</sup> + RIM1-ZnC<sub>2</sub>B<sup>KE</sup> 18/4.

**(N)** Rescue of peak dopamine evoked by a 90  $\mu$ A electrical stimulus for each rescue experiment in Figs. 1, S1, 8, and S8, normalized to the average of the unrelated control mice used for all rescue conditions, RIM cKO<sup>DA</sup> + RIM1-Zn + RIM1- $\Delta$ Zn 15/4; RIM cKO<sup>DA</sup> + RIM1-Zn 12/4; RIM cKO<sup>DA</sup> + RIM1- $\Delta$ Zn 10/3; RIM cKO<sup>DA</sup> + RIM1-ZnC<sub>2</sub>B 22/5; RIM cKO<sup>DA</sup> + RIM1-ZnC<sub>2</sub>B<sup>KE</sup> 20/5; RIM cKO<sup>DA</sup> + RIM1-ZnPCP 19/4; control 72/20 (used for normalization). Rescue data from the RIM cKO<sup>DA</sup> + RIM1- ZnC<sub>2</sub>B vs. RIM cKO<sup>DA</sup> + RIM1-ZnC<sub>2</sub>B<sup>KE</sup> experiment (Figs. 8D, 8E) was used for the summary plot.

**(O)** Same as N but for rescue estimated by KCl evoked dopamine release, RIM cKO<sup>DA</sup> + RIM1-Zn + RIM1- $\Delta$ Zn 17/4; RIM cKO<sup>DA</sup> + RIM1-Zn 11/4; RIM cKO<sup>DA</sup> + RIM1- $\Delta$ Zn 10/3; RIM cKO<sup>DA</sup> + RIM1-ZnC<sub>2</sub>B 23/5; RIM cKO<sup>DA</sup> + RIM1-ZnC<sub>2</sub>B<sup>KE</sup> 21/5; RIM cKO<sup>DA</sup> + RIM1-ZnPCP 18/4; control 73/20 (used for normalization). Rescue data from the RIM cKO<sup>DA</sup> + RIM1- ZnC<sub>2</sub>B vs. RIM cKO<sup>DA</sup> + RIM1-ZnC<sub>2</sub>B<sup>KE</sup> experiment (Figs. 8J, 8K) was used for the summary plot.

Data are mean  $\pm$  SEM, \*  $p < 0.05$ , \*\*  $p < 0.01$ , \*\*\*  $p < 0.001$  as assessed by Mann-Whitney tests in K, M and one-way ANOVA followed by Dunnett's multiple comparisons tests in N and O, where all comparisons were made to RIM cKO<sup>DA</sup> + RIM1-Zn + RIM1- $\Delta$ Zn.

**Table S1. Means, number of observations and statistical testing, related to Figs. 1 and S1**

For each dataset, mean  $\pm$  SEM are shown in the corresponding figure. The sample size that has been used for statistical testing is shown in bold for each data set.

Figure Parameter (units)	Mean $\pm$ SEM and sample size	Statistical test p-value
1D Peak dopamine ( $\mu$ M) evoked by a 90 $\mu$ A electrical stimulus	RIM control = $1.50 \pm 0.13$ (n = <b>17 slices</b> , 3 mice) RIM cKO <sup>DA</sup> = $0.07 \pm 0.01$ (n = <b>17 slices</b> , 3 mice) Each circle in the figure represents a slice recording that has been used for sample size in statistics.	Mann-Whitney test p < 0.0001
1F Peak dopamine ( $\mu$ M) evoked by a KCl puff	RIM control = $6.45 \pm 0.67$ (n = <b>20 slices</b> , 3 mice) RIM cKO <sup>DA</sup> = $0.40 \pm 0.05$ (n = <b>20 slices</b> , 3 mice) Each circle in the figure represents a slice recording that has been used for sample size in statistics.	Mann-Whitney test p < 0.0001
1I Peak dopamine ( $\mu$ M) evoked by a 90 $\mu$ A electrical stimulus	RIM cKO <sup>DA</sup> = $0.09 \pm 0.01$ (n = <b>12 slices</b> , 4 mice) RIM cKO <sup>DA</sup> + RIM1-Zn = $0.14 \pm 0.02$ (n = <b>12 slices</b> , 4 mice) Each circle in the figure represents a slice recording that has been used for sample size in statistics.	Mann-Whitney test p = 0.07
1K Peak dopamine ( $\mu$ M) evoked by a 90 $\mu$ A electrical stimulus	RIM cKO <sup>DA</sup> = $0.053 \pm 0.009$ (n = <b>9 slices</b> , 3 mice) RIM cKO <sup>DA</sup> + RIM1- $\Delta$ Zn = $0.050 \pm 0.006$ (n = <b>10 slices</b> , 3 mice) Each circle in the figure represents a slice recording that has been used for sample size in statistics.	Mann-Whitney test p = 0.8
1M Peak dopamine ( $\mu$ M) evoked by a 90 $\mu$ A electrical stimulus	RIM cKO <sup>DA</sup> = $0.07 \pm 0.01$ (n = <b>15 slices</b> , 4 mice) RIM cKO <sup>DA</sup> + RIM1-Zn + RIM1- $\Delta$ Zn = $0.28 \pm 0.05$ (n = <b>15 slices</b> , 4 mice) Each circle in the figure represents a slice recording that has been used for sample size in statistics.	Mann-Whitney test p = 0.0003
1O Peak dopamine ( $\mu$ M) evoked by a KCl puff	RIM cKO <sup>DA</sup> = $0.19 \pm 0.04$ (n = <b>11 slices</b> , 4 mice) RIM cKO <sup>DA</sup> + RIM1-Zn = $1.09 \pm 0.13$ (n = <b>11 slices</b> , 4 mice) Each circle in the figure represents a slice recording that has been used for sample size in statistics.	Mann-Whitney test p < 0.0001
1Q Peak dopamine ( $\mu$ M) evoked by a KCl puff	RIM cKO <sup>DA</sup> = $0.25 \pm 0.06$ (n = <b>10 slices</b> , 3 mice) RIM cKO <sup>DA</sup> + RIM1- $\Delta$ Zn = $0.38 \pm 0.05$ (n = <b>10</b> )	Mann-Whitney test p = 0.08

	<p><b>slices</b>, 3 mice) Each circle in the figure represents a slice recording that has been used for sample size in statistics.</p>	
1S Peak dopamine ( $\mu\text{M}$ ) evoked by a KCl puff	<p>RIM cKO<sup>DA</sup> = <math>0.17 \pm 0.03</math> (n = <b>16 slices</b>, 4 mice) RIM cKO<sup>DA</sup> + RIM1-Zn + RIM1-<math>\Delta</math>Zn = <math>2.98 \pm 0.44</math> (n = <b>17 slices</b>, 4 mice) Each circle in the figure represents a slice recording that has been used for sample size in statistics.</p>	Mann-Whitney test p < 0.0001
S1A Peak dopamine ( $\mu\text{M}$ ) evoked by a 90 $\mu\text{A}$ electrical stimulus before and after DH $\beta$ E	<p>ACSF = <math>1.29 \pm 0.16</math> (n = <b>6 slices</b>, 3 mice) DH<math>\beta</math>E = <math>0.14 \pm 0.02</math> (n = <b>6 slices</b>, 3 mice) Each circle in the figure represents a slice recording that has been used for sample size in statistics.</p>	Paired t-test p = 0.001
S1C Peak dopamine ( $\mu\text{M}$ ) evoked by a 90 $\mu\text{A}$ electrical stimulus	<p>Control = <math>1.34 \pm 0.15</math> (n = 12 slices, 4 mice) Each circle in the figure represents a slice recording.</p>	not applicable
S1D Peak dopamine ( $\mu\text{M}$ ) evoked by a 90 $\mu\text{A}$ electrical stimulus	<p>Control = <math>1.09 \pm 0.13</math> (n = 8 slices, 3 mice) Each circle in the figure represents a slice recording.</p>	not applicable
S1E Peak dopamine ( $\mu\text{M}$ ) evoked by a 90 $\mu\text{A}$ electrical stimulus	<p>Control = <math>1.45 \pm 0.08</math> (n = 16 slices, 4 mice) Each circle in the figure represents a slice recording.</p>	not applicable
S1F Peak dopamine ( $\mu\text{M}$ ) evoked by a KCl puff	<p>Control = <math>5.00 \pm 0.60</math> (n = 10 slices, 4 mice) Each circle in the figure represents a slice recording.</p>	not applicable
S1G Peak dopamine ( $\mu\text{M}$ ) evoked by a KCl puff	<p>Control = <math>3.83 \pm 0.43</math> (n = 9 slices, 3 mice) Each circle in the figure represents a slice recording.</p>	not applicable
S1H Peak dopamine ( $\mu\text{M}$ ) evoked by a KCl puff	<p>Control = <math>6.23 \pm 0.51</math> (n = 15 slices, 4 mice) Each circle in the figure represents a slice recording.</p>	not applicable
S1J Peak dopamine ( $\mu\text{M}$ ) evoked by a KCl puff	<p>(a) KCl evoked 1<sup>st</sup> response in ACSF with 2 mM Ca<sup>2+</sup> = <math>4.46 \pm 0.56</math> (b) KCl evoked 2<sup>nd</sup> response in ACSF with 2 mM Ca<sup>2+</sup> after 15 min = <math>2.64 \pm 0.44</math> (c) KCl evoked 1<sup>st</sup> response in ACSF with 0 mM Ca<sup>2+</sup> + 1 mM EGTA = <math>0.14 \pm 0.03</math> (d) KCl evoked 2<sup>nd</sup> response after switching (c) to ACSF with 2 mM Ca<sup>2+</sup> = <math>3.47 \pm 0.46</math> Each circle in the figure represents a slice recording that has been used for sample size in statistics and sample size was <b>15 slices</b> from 4 mice each.</p>	Repeated measures one-way ANOVA (p < 0.0001, F = 32.05) followed by Sidak's multiple comparisons tests for specific pairs: a vs. b (p = 0.0029); a vs. c (p < 0.0001); c vs. d (p < 0.0001); and b vs. d (p = 0.1).
S1L Peak dopamine ( $\mu\text{M}$ ) evoked by a KCl puff	<p>ACSF = <math>7.98 \pm 1.17</math> (n = <b>10 slices</b>, 4 mice) DH<math>\beta</math>E = <math>8.31 \pm 0.87</math> (n = <b>10 slices</b>, 4 mice) DH<math>\beta</math>E + TTX = <math>7.75 \pm 1.01</math> (n = <b>10 slices</b>, 4 mice)</p>	One-way ANOVA (p = 0.9, F = 0.07609) followed by Sidak's multiple comparisons tests for specific pairs:

	Each circle in the figure represents a slice recording that has been used for sample size in statistics.	ACSF vs. DH $\beta$ E ( $p = 0.9$ ) and ACSF vs. DH $\beta$ E + TTX ( $p = 0.9$ ).
--	--	--

**Table S2. Means, medians, number of observations and statistical testing, related to Fig. 2**

For each dataset, mean  $\pm$  SEM are shown in the corresponding figure. For image data, median values are reported here in addition to mean  $\pm$  SEM. The sample size that has been used for statistical testing is shown in bold for each data set.

Figure Parameter (units)	Mean $\pm$ SEM and sample size Median (for imaging data only)	Statistical test p-value
2C Munc13-1 clusters/image volume ( $\#\mu\text{m}^3$ )	Munc13-1-EYFP = $3.598 \pm 0.033$ , median: 3.611 (n = <b>88 images</b> , 3 mice) wild type = $0.017 \pm 0.001$ , median: 0.016 (n = <b>86 images</b> , 3 mice) The distribution of values for each image is shown as violin plots with superimposed mean $\pm$ SEM for Munc13-1-EYFP. All values for wild type were very close to zero and are shown as scatter plots, where each circle represents an image that has been used for sample size in statistics.	Unpaired t-test p < 0.0001
2D Munc13-1 volume/image volume ( $\mu\text{m}^3/\mu\text{m}^3$ )	Munc13-1-EYFP = $0.047 \pm 0.001$ , median: 0.047 (n = <b>88 images</b> , 3 mice) wild type = $0.00022 \pm 0.00002$ , median: 0.0002 (n = <b>86 images</b> , 3 mice) The distribution of values for each image is shown as violin plots with superimposed mean $\pm$ SEM for Munc13-1-EYFP. All values for wild type were very close to zero and are shown as scatter plots, where each circle represents an image that has been used for sample size in statistics.	Unpaired t-test p < 0.0001
2E TH volume/image volume ( $\mu\text{m}^3/\mu\text{m}^3$ )	Munc13-1-EYFP = $0.078 \pm 0.002$ , median: 0.077 (n = <b>88 images</b> , 3 mice) wild type = $0.079 \pm 0.002$ , median: 0.077 (n = <b>86 images</b> , 3 mice) The distribution of images in the figure is shown as violin plots with superimposed mean $\pm$ SEM.	Unpaired t-test p = 0.5
2F TH length/image volume ( $\mu\text{m}/\mu\text{m}^3$ )	Munc13-1-EYFP = $1.02 \pm 0.03$ , median: 0.98 (n = <b>88 images</b> , 3 mice) wild type = $0.98 \pm 0.02$ , median: 0.94 (n = <b>86 images</b> , 3 mice) The distribution of images in the figure is shown as violin plots with superimposed mean $\pm$ SEM.	Unpaired t-test p = 0.2
2G Munc13-1 clusters/ $\mu\text{m}$ of TH axon	Munc13-1-EYFP = $0.448 \pm 0.009$ , median: 0.445 (n = <b>88 images</b> , 3 mice) wild type = $0.003 \pm 0.001$ , median: 0.002 (n = <b>86 images</b> , 3 mice) The distribution of values for each image is shown as violin plots with superimposed mean $\pm$ SEM for Munc13-1-EYFP. All values for wild type were very close to zero and are shown as scatter plots, where each circle represents an	Unpaired t-test p < 0.0001



	image that has been used for sample size in statistics.	
2H Munc13-1 clusters/ $\mu\text{m}$ of TH axon	Munc13-1-EYFP actual = $0.448 \pm 0.009$ , median: 0.445 (n = <b>88 images</b> , 3 mice) Munc13-1-EYFP shuffled = $0.270 \pm 0.003$ , median: 0.272 (n = <b>88 images</b> , 3 mice) Each circle in the figure represents an image that has been used for sample size in statistics.	Paired t-test $p < 0.0001$
2I Munc13-1 cluster volume ( $\times 0.01 \mu\text{m}^3$ )	Munc13-1-EYFP actual = $1.17 \pm 0.01$ , median: 1.18 (n = <b>88 images</b> , 3 mice) Munc13-1-EYFP shuffled = $1.08 \pm 0.01$ , median: 1.08 (n = <b>88 images</b> , 3 mice) Each circle in the figure represents an image that has been used for sample size in statistics.	Paired t-test $p < 0.0001$

**Table S3. Means, number of observations and statistical testing, related to Figs. 3 and S2-S4**

For each dataset, mean  $\pm$  SEM are shown in the corresponding figure. The sample size that has been used for statistical testing is shown in bold for each data set.

Figure Parameter (units)	Mean $\pm$ SEM and sample size	Statistical test p-value
3D Peak dopamine ( $\mu$ m) evoked by the 1 <sup>st</sup> stimulus of a 10 Hz train of optogenetic stimulation	Munc13 control = $0.482 \pm 0.033$ (n = <b>5 slices</b> , 3 mice) Munc13 control + TTX = $0.008 \pm 0.002$ (n = <b>5 slices</b> , 3 mice) Munc13 cKO <sup>DA</sup> = $0.076 \pm 0.008$ (n = <b>5 slices</b> , 3 mice) Munc13 cKO <sup>DA</sup> + TTX = $0.012 \pm 0.002$ (n = <b>5 slices</b> , 3 mice) Each circle in the figure represents a slice recording that has been used for sample size in statistics.	Repeated measures one-way ANOVA ( $p < 0.0001$ , $F = 193.7$ ) followed by Sidak's multiple comparisons tests for specific pairs: Munc13 control vs. Munc13 control + TTX ( $p = 0.0006$ ); Munc13 control vs. Munc13 cKO <sup>DA</sup> ( $p = 0.0006$ ); Munc13 cKO <sup>DA</sup> vs. Munc13 cKO <sup>DA</sup> + TTX ( $p = 0.0062$ ); and Munc13 control + TTX vs. Munc13 cKO <sup>DA</sup> + TTX ( $p = 0.7$ ).
3E Peak dopamine evoked by a 10 Hz train of optogenetic stimulation normalized to the 1 <sup>st</sup> peak amplitude of Munc13 control (mean $\pm$ SEM for stimulus 2, 6 and 10 are listed here)	Munc13 control stimulus 2: $0.36 \pm 0.05$ ; stimulus 6: $0.09 \pm 0.02$ and stimulus 10: $0.06 \pm 0.01$ . Munc13 cKO <sup>DA</sup> stimulus 2: $0.11 \pm 0.02$ ; stimulus 6: $0.06 \pm 0.01$ and stimulus 10: $0.06 \pm 0.01$ . Each circle in the figure represents the mean $\pm$ SEM from all recorded slices; Munc13 control = <b>6 slices</b> , 3 mice and Munc13 cKO <sup>DA</sup> = <b>6 slices</b> , 3 mice.	Two-way ANOVA ( $p < 0.0001$ for genotype $F = 445.4$ ; $p < 0.0001$ for stimulus number $F = 101.5$ and $p < 0.0001$ for interaction $F = 112.1$ ) followed by Sidak's multiple comparisons tests between Munc13 control vs. Munc13 cKO <sup>DA</sup> for each stimulus: stimulus 1-4 ( $p < 0.0001$ ); stimulus 5 ( $p = 0.0128$ ); and stimulus 6-10 ( $p > 0.9$ ).
3G Peak dopamine ( $\mu$ M) evoked by a KCl puff	Munc13 control = $3.55 \pm 0.53$ (n = <b>7 slices</b> , 3 mice) Munc13 cKO <sup>DA</sup> = $0.09 \pm 0.01$ (n = <b>7 slices</b> , 3 mice) Each circle in the figure represents a slice recording that has been used for sample size in statistics.	Mann-Whitney test $p = 0.0006$
3H Total dopamine ( $\times 100 \mu$ M $\times$ s) evoked by a KCl puff	Munc13 control = $1.012 \pm 0.205$ (n = <b>7 slices</b> , 3 mice) Munc13 cKO <sup>DA</sup> = $0.021 \pm 0.004$ (n = <b>7 slices</b> , 3 mice) Each circle in the figure represents a slice recording that has been used for sample size in statistics.	Mann-Whitney test $p = 0.0006$
S2D Normalized protein level	Munc13-1 <sup>+/+</sup> = $1.00 \pm 0.08$ (n = 3 mice) Munc13-1 <sup>fl/fl</sup> = $1.02 \pm 0.12$ (n = 3 mice)	no statistics used
S2F	Munc13-1 <sup>+/+</sup> = $1.00 \pm 0.21$ (n = 3 mice)	no statistics used

Normalized protein level	Munc13-1 cKO <sup>gl</sup> = 0.05 ± 0.01 (n = 3 mice)	
S3B mEPSC frequency (Hz)	Munc13-1 <sup>+/+</sup> = 6.04 ± 0.84 (n = <b>36 neurons</b> , 3 independent cultures) Munc13-1 cKO <sup>gl</sup> = 1.79 ± 0.44 (n = <b>39 neurons</b> , 3 independent cultures) Each circle in the figure represents a whole cell recording from a neuron that has been used for sample size in statistics.	Mann-Whitney test (p < 0.0001)
S3C mEPSC amplitude (pA)	Munc13-1 <sup>+/+</sup> = 36.35 ± 2.30 (n = <b>36 neurons</b> , 3 independent cultures) Munc13-1 cKO <sup>gl</sup> = 27.27 ± 1.76 (n = <b>33 neurons</b> , 3 independent cultures) Each circle in the figure represents a whole cell recording from a neuron that has been used for sample size in statistics.	Mann-Whitney test (p = 0.0176)
S3E EPSC amplitude (nA)	Munc13-1 <sup>+/+</sup> = 6.50 ± 0.54 (n = <b>57 neurons</b> , 3 independent cultures) Munc13-1 cKO <sup>gl</sup> = 1.89 ± 0.25 (n = <b>56 neurons</b> , 3 independent cultures) Each circle in the figure represents a whole cell recording from a neuron that has been used for sample size in statistics.	Mann-Whitney test (p < 0.0001)
S3G sucrose EPSC amplitude (nC)	Munc13-1 <sup>+/+</sup> = 1.04 ± 0.18 (n = <b>54 neurons</b> , 3 independent cultures) Munc13-1 cKO <sup>gl</sup> = 0.14 ± 0.25 (n = <b>53 neurons</b> , 3 independent cultures) Each circle in the figure represents a whole cell recording from a neuron that has been used for sample size in statistics.	Mann-Whitney test (p < 0.0001)
S3I EPSC triggered by 10 stimuli at 10 Hz normalized to the mean of the 1 <sup>st</sup> EPSC of Munc13-1 <sup>+/+</sup> (mean ± SEM for stimulus 1, 2, 6 and 10 are listed here)	Munc13-1 <sup>+/+</sup> stimulus 1: 1.00 ± 0.09; stimulus 2: 0.90 ± 0.08; stimulus 6: 0.70 ± 0.07 and stimulus 10: 0.65 ± 0.07. Munc13-1 cKO <sup>gl</sup> stimulus 1: 0.31 ± 0.04; stimulus 2: 0.23 ± 0.03; stimulus 6: 0.18 ± 0.02 and stimulus 10: 0.19 ± 0.02. Each circle in the figure represents the mean ± SEM from all neuronal recordings that has been used for sample size in statistics; Munc13-1 <sup>+/+</sup> = <b>40 neurons</b> , 3 independent cultures and Munc13-1 cKO <sup>gl</sup> = <b>44 neurons</b> , 3 independent cultures.	Two-way ANOVA (p < 0.0001, F = 496.4 for genotype, p < 0.0001, F = 3.901 for stimulus number and p = 0.4, F = 1.013 for interaction) followed by Sidak's multiple comparisons tests between Munc13-1 <sup>+/+</sup> vs. Munc13-1 cKO <sup>gl</sup> for each stimulus: stimulus 1-10 (p < 0.0001).
S4D Amplitude (mV) of the extracellular potential evoked by the 1 <sup>st</sup> stimulus of a 10 Hz train of optogenetic stimulation	Munc13 control = 0.046 ± 0.006 (n = <b>8 slices</b> , 6 mice) Munc13 control + TTX = 0.022 ± 0.003 (n = <b>8 slices</b> , 6 mice) Munc13 cKO <sup>DA</sup> = 0.050 ± 0.006 (n = <b>8 slices</b> , 6 mice) Munc13 cKO <sup>DA</sup> + TTX = 0.026 ± 0.005 (n = <b>8 slices</b> , 6 mice) Each circle in the figure represents a slice recording that has been used for sample size in statistics.	Repeated measures one-way ANOVA (p < 0.0001, F = 16.38) followed by Sidak's multiple comparisons tests for specific pairs: Munc13 control vs. Munc13 control + TTX (p = 0.0003); Munc13 control vs. Munc13 cKO <sup>DA</sup> (p = 0.8); Munc13 cKO <sup>DA</sup> vs. Munc13 cKO <sup>DA</sup> + TTX (p = 0.0003); and

		Munc13 control + TTX vs. Munc13 cKO <sup>DA</sup> + TTX (p = 0.9).
S4E Amplitudes of the extracellular potentials evoked by a 10 Hz train of optogenetic stimulation normalized to the 1 <sup>st</sup> peak amplitude of Munc13 control (mean ± SEM for stimulus 2, 6 and 10 are listed here)	Munc13 control stimulus 2: 0.98 ± 0.15; stimulus 6: 0.98 ± 0.15 and stimulus 10: 0.99 ± 0.15. Munc13 cKO <sup>DA</sup> stimulus 2: 1.06 ± 0.16; stimulus 6: 1.09 ± 0.15 and stimulus 10: 1.06 ± 0.16. Each circle in the figure represents the mean ± SEM from all recorded slices; Munc13 control = <b>8 slices</b> , 6 mice and Munc13 cKO <sup>DA</sup> = <b>8 slices</b> , 6 mice.	Two-way ANOVA (p = 0.7, F = 0.1554 for genotype; p = 0.0646, F = 1.923 for stimulus number and p = 0.4, F = 0.9617 for interaction).
S4G Amplitudes of the extracellular potentials evoked by a 40 Hz train of optogenetic stimulation normalized to the 1 <sup>st</sup> peak amplitude of Munc13 control (mean ± SEM for stimulus 1, 2, 6 and 10 are listed here)	Munc13 control stimulus 1: 1.00 ± 0.11; stimulus 2: 0.73 ± 0.11; stimulus 6: 0.67 ± 0.10 and stimulus 10: 0.68 ± 0.10. Munc13 cKO <sup>DA</sup> stimulus 1: 0.88 ± 0.19; stimulus 2: 0.65 ± 0.18; stimulus 6: 0.64 ± 0.18 and stimulus 10: 0.62 ± 0.16. Each circle in the figure represents the mean ± SEM from all recorded slices; Munc13 control = <b>6 slices</b> , 5 mice and Munc13 cKO <sup>DA</sup> = <b>6 slices</b> , 5 mice.	Two-way ANOVA (p = 0.7, F = 0.1394 for genotype; p < 0.0001, F = 74.06 for stimulus number and p = 0.3, F = 1.187 for interaction).

**Table S4. Means, number of observations and statistical testing, related to Fig. 4**

For each dataset, mean  $\pm$  SEM are shown in the corresponding figure. The sample size that has been used for statistical testing is shown in bold for each data set.

Figure Parameter (units)	Mean $\pm$ SEM and sample size	Statistical test p-value
4B Peak dopamine ( $\mu\text{M}$ ) evoked by single electrical pulses at increasing stimulation intensities of 10-90 $\mu\text{A}$ (mean $\pm$ SEM for 10 $\mu\text{A}$ , 50 $\mu\text{A}$ and 90 $\mu\text{A}$ are listed here)	Munc13 control 10 $\mu\text{A}$ : $0.06 \pm 0.02$ ; 50 $\mu\text{A}$ : $0.65 \pm 0.07$ and 90 $\mu\text{A}$ : $0.78 \pm 0.14$ . Munc13 cKO <sup>DA</sup> 10 $\mu\text{A}$ : $0.02 \pm 0.01$ ; 50 $\mu\text{A}$ : $0.08 \pm 0.02$ and 90 $\mu\text{A}$ : $0.07 \pm 0.01$ . Each circle in the figure represents the mean $\pm$ SEM from all recorded slices; Munc13 control = <b>10 slices</b> , 5 mice and Munc13 cKO <sup>DA</sup> = <b>10 slices</b> , 5 mice.	Two-way ANOVA ( $p < 0.0001$ , $F = 92.43$ for genotype; $p < 0.0001$ , $F = 13.28$ for stimulus intensity and $p < 0.0001$ , $F = 10.00$ for interaction) followed by Sidak's multiple comparisons tests between Munc13 control vs. Munc13 cKO <sup>DA</sup> for each stimulus intensity: 10 $\mu\text{A}$ ( $p > 0.9$ ); 20 $\mu\text{A}$ ( $p = 0.0119$ ); and 30-90 $\mu\text{A}$ ( $p < 0.0001$ ).
4D Peak dopamine evoked by a 10 Hz train of electrical stimulation at 90 $\mu\text{A}$ normalized to the 1 <sup>st</sup> peak amplitude of Munc13 control (mean $\pm$ SEM for stimulus 2, 6 and 10 are listed here)	Munc13 control stimulus 2: $0.028 \pm 0.004$ ; stimulus 6: $0.027 \pm 0.003$ and stimulus 10: $0.029 \pm 0.005$ . Munc13 cKO <sup>DA</sup> stimulus 2: $0.023 \pm 0.005$ ; stimulus 6: $0.026 \pm 0.005$ and stimulus 10: $0.029 \pm 0.005$ Each circle in the figure represents the mean $\pm$ SEM from all recorded slices; Munc13 control = <b>8 slices</b> , 4 mice and Munc13 cKO <sup>DA</sup> = <b>8 slices</b> , 4 mice.	Two-way ANOVA ( $p < 0.0001$ , $F = 206.8$ for genotype; $p < 0.0001$ , $F = 506.4$ for stimulus number and $p < 0.0001$ , $F = 216.8$ for interaction) followed by Sidak's multiple comparisons tests between Munc13 control vs. Munc13 cKO <sup>DA</sup> for each stimulus: stimulus 1 ( $p < 0.0001$ ); and stimulus 2-10 ( $p > 0.9$ ).
4D inset Peak dopamine ( $\mu\text{M}$ ) evoked by 1 <sup>st</sup> stimulus of a 10 Hz train of electrical stimulation	Munc13 control = $0.86 \pm 0.04$ ( $n =$ <b>8 slices</b> , 4 mice) Munc13 cKO <sup>DA</sup> = $0.04 \pm 0.02$ ( $n =$ <b>8 slices</b> , 4 mice) Each circle in the figure represents a slice recording that has been used for sample size in statistics; sample size as in Fig. 4D.	Mann-Whitney test $p = 0.0002$
4E In vivo extracellular dopamine measured in microdialysis, normalized to the average dopamine values of the 76 <sup>th</sup> – 120 <sup>th</sup> min of Munc13 control (mean $\pm$ SEM for 90 <sup>th</sup> , 165 <sup>th</sup> and 240 <sup>th</sup> min are listed here)	Munc13 control 90 <sup>th</sup> min: $1.00 \pm 0.07$ ; 165 <sup>th</sup> min: $0.37 \pm 0.05$ and 240 <sup>th</sup> min: $0.27 \pm 0.04$ Munc13 cKO <sup>DA</sup> 90 <sup>th</sup> min: $0.36 \pm 0.08$ ; 165 <sup>th</sup> min: $0.25 \pm 0.06$ and 240 <sup>th</sup> min: $0.22 \pm 0.05$ Each circle in the figure represents the mean $\pm$ SEM of all experimental mice that was used for sample size in statistics; Munc13 control = <b>7 mice</b> and Munc13 cKO <sup>DA</sup> = <b>7 mice</b> .	Two-way ANOVA ( $p = 0.0004$ , $F = 50.18$ for genotype; $p < 0.0001$ , $F = 158.60$ for time points and $p < 0.0001$ , $F = 49.00$ for interaction) followed by Sidak's multiple comparisons tests between Munc13 control vs. Munc13 cKO <sup>DA</sup> for each time point: 90-150 <sup>th</sup> min ( $p < 0.0001$ ); 165-195 <sup>th</sup> min ( $p < 0.01$ ); and 210-240 <sup>th</sup> min ( $p > 0.6$ ).

**Table S5. Means, medians, number of observations and statistical testing, related to Figs. 5 and S5**

For each dataset, mean  $\pm$  SEM are shown in the corresponding figure, except for Fig. 5J (mean  $\pm$  SD). For image data, median values are reported in the tables in addition to mean  $\pm$  SEM. The sample size that has been used for statistical testing is shown in bold for each data set.

Figure Parameter (units)	Mean $\pm$ SEM and sample size Median (for imaging data only)	Statistical test p-value
5B TH intensity (a.u.) in TH <sup>+</sup> ROIs	Munc13 control = 1402 $\pm$ 102, median: 1374 (n = <b>30 images</b> , 3 mice) Munc13 cKO <sup>DA</sup> = 1715 $\pm$ 79, median: 1723 (n = <b>30 images</b> , 3 mice) Each circle in the figure represents an image that has been used for sample size in statistics.	Unpaired t-test p = 0.018
5C Synaptophysin intensity (a.u.) in TH <sup>+</sup> ROIs	Munc13 control = 400 $\pm$ 22, median: 373 (n = <b>30 images</b> , 3 mice) Munc13 cKO <sup>DA</sup> = 348 $\pm$ 13, median: 338 (n = <b>30 images</b> , 3 mice) Each circle in the figure represents an image that has been used for sample size in statistics.	Unpaired t-test p = 0.043
5D Bassoon intensity (a.u.) in synaptophysin <sup>+</sup> TH <sup>-</sup> (syp <sup>+</sup> TH <sup>-</sup> ) and synaptophysin <sup>+</sup> TH <sup>+</sup> (syp <sup>+</sup> TH <sup>+</sup> ) ROIs	syp <sup>+</sup> TH <sup>-</sup> of Munc13 control = 480 $\pm$ 23, median: 433 (n = <b>30 images</b> , 3 mice) syp <sup>+</sup> TH <sup>-</sup> of Munc13 cKO <sup>DA</sup> = 493 $\pm$ 21, median: 495 (n = <b>30 images</b> , 3 mice) syp <sup>+</sup> TH <sup>+</sup> of Munc13 control = 511 $\pm$ 29, median: 528 (n = <b>29 images</b> , 3 mice) syp <sup>+</sup> TH <sup>+</sup> of Munc13 cKO <sup>DA</sup> = 613 $\pm$ 39, median: 617 (n = <b>29 images</b> , 3 mice) Each circle in the figure represents an image that has been used for sample size in statistics.	One-way ANOVA (p = 0.0055, F = 4.428) followed by Sidak's multiple comparisons tests for specific pairs: syp <sup>+</sup> TH <sup>-</sup> of Munc13 control vs. Munc13 cKO <sup>DA</sup> (p = 0.9); and syp <sup>+</sup> TH <sup>+</sup> of Munc13 control vs. Munc13 cKO <sup>DA</sup> (p = 0.0291).
5E Frequency histogram of Bassoon intensity (a.u.) in syp <sup>+</sup> TH <sup>+</sup> ROIs	syp <sup>+</sup> TH <sup>+</sup> of Munc13 control (n = <b>221 syp<sup>+</sup>TH<sup>+</sup> ROIs</b> , 29 images, 3 mice) syp <sup>+</sup> TH <sup>+</sup> of Munc13 cKO <sup>DA</sup> (n = <b>168 syp<sup>+</sup>TH<sup>+</sup> ROIs</b> , 29 images, 3 mice)	Kolmogorov-Smirnov test p < 0.0001
5G TH volume/image volume ( $\mu\text{m}^3/\mu\text{m}^3$ )	Munc13 control = 0.073 $\pm$ 0.002, median: 0.07 (n = <b>163 images</b> , 4 mice) Munc13 cKO <sup>DA</sup> = 0.063 $\pm$ 0.002, median: 0.06 (n = <b>165 images</b> , 4 mice) The distribution of images in the figure is shown as violin plots with superimposed mean $\pm$ SEM.	Unpaired t-test p < 0.0001
5H TH length/image volume ( $\mu\text{m}/\mu\text{m}^3$ )	Munc13 control = 0.99 $\pm$ 0.02, median: 0.92 (n = <b>163 images</b> , 4 mice) Munc13 cKO <sup>DA</sup> = 0.68 $\pm$ 0.02, median: 0.62 (n = <b>165 images</b> , 4 mice) The distribution of images in the figure is shown as violin plots with superimposed mean $\pm$ SEM.	Unpaired t-test p < 0.0001
5J Fraction of the TH surface area at increasing distances	Munc13 control 0.2 $\mu\text{m}$ : 0.196 $\pm$ 0.007, median: 0.197; 0.4 $\mu\text{m}$ : 0.022 $\pm$ 0.004, median: 0.021; 0.6 $\mu\text{m}$ : 0.0020 $\pm$ 0.0004, median: 0.002	Two-way ANOVA (p < 0.0001, F = 68.16 for genotype; p < 0.0001, F = 22330 for distance)

from the medial axis of the TH axon (mean $\pm$ SD and median for 0.2 $\mu\text{m}$ , 0.4 $\mu\text{m}$ , and 0.6 $\mu\text{m}$ are listed here)	Munc13 cKO <sup>DA</sup> 0.2 $\mu\text{m}$ : 0.162 $\pm$ 0.014, median: 0.164; 0.4 $\mu\text{m}$ : 0.043 $\pm$ 0.008, median: 0.043; 0.6 $\mu\text{m}$ : 0.006 $\pm$ 0.002, median: 0.006 Sample size was <b>160 images</b> from 4 mice each for Munc13 control and Munc13 cKO <sup>DA</sup> .	and $p < 0.0001$ , $F = 506.1$ for interaction).
5K Bassoon clusters/ $\mu\text{m}$ of TH axon	Munc13 control = 0.172 $\pm$ 0.003, median: 0.18 (n = <b>163 images</b> , 4 mice) Munc13 cKO <sup>DA</sup> = 0.254 $\pm$ 0.007, median: 0.26 (n = <b>165 images</b> , 4 mice) The distribution of images in the figure is shown as violin plots with superimposed mean $\pm$ SEM.	Unpaired t-test $p < 0.0001$
5L Bassoon cluster volume (x 0.01 $\mu\text{m}^3$ )	Munc13 control = 1.25 $\pm$ 0.01, median: 1.26 (n = <b>163 images</b> , 4 mice) Munc13 cKO <sup>DA</sup> = 1.54 $\pm$ 0.02, median: 1.59 (n = <b>165 images</b> , 4 mice) The distribution of images in the figure is shown as violin plots with superimposed mean $\pm$ SEM.	Unpaired t-test $p < 0.0001$
S5B Bassoon intensity (a.u.) in TH <sup>+</sup> ROIs	Munc13 control = 426 $\pm$ 25, median: 429 (n = <b>40 images</b> , 4 mice) Munc13 cKO <sup>DA</sup> = 625 $\pm$ 33, median: 633 (n = <b>39 images</b> , 4 mice) Each circle in the figure represents an image that has been used for sample size in statistics.	Unpaired t-test $p < 0.0001$
S5C Frequency histogram of Bassoon intensity (a.u.) in TH <sup>+</sup> ROIs	Munc13 control (n = <b>3035 TH<sup>+</sup> ROIs</b> , 40 images, 4 mice) Munc13 cKO <sup>DA</sup> (n = <b>1745 TH<sup>+</sup> ROIs</b> , 39 images, 4 mice)	Kolmogorov-Smirnov test $p < 0.0001$
S5E RIM intensity (a.u.) in TH <sup>+</sup> ROIs	Munc13 control = 371 $\pm$ 12, median: 363 (n = <b>29 images</b> , 3 mice) Munc13 cKO <sup>DA</sup> = 485 $\pm$ 21, median: 495 (n = <b>29 images</b> , 3 mice) Each circle in the figure represents an image that has been used for sample size in statistics.	Unpaired t-test $p < 0.0001$
S5F Frequency histogram of RIM intensity (a.u.) in TH <sup>+</sup> ROIs	Munc13 control (n = <b>4766 TH<sup>+</sup> ROIs</b> , 29 images, 3 mice) Munc13 cKO <sup>DA</sup> (n = <b>1639 TH<sup>+</sup> ROIs</b> , 29 images, 3 mice)	Kolmogorov-Smirnov test $p < 0.0001$
S5H TH volume/image volume ( $\mu\text{m}^3/\mu\text{m}^3$ )	Munc13 control = 0.11 $\pm$ 0.01, median: 0.1 (n = <b>37 images</b> , 3 mice) Munc13 cKO <sup>DA</sup> = 0.07 $\pm$ 0.01, median: 0.06 (n = <b>37 images</b> , 3 mice) Each circle in the figure represents an image that has been used for sample size in statistics.	Unpaired t-test $p < 0.0001$
S5I TH length/image volume ( $\mu\text{m}/\mu\text{m}^3$ )	Munc13 control = 1.10 $\pm$ 0.06, median: 1.0 (n = <b>37 images</b> , 3 mice) Munc13 cKO <sup>DA</sup> = 0.72 $\pm$ 0.06, median: 0.68 (n = <b>37 images</b> , 3 mice) Each circle in the figure represents an image that has been used for sample size in statistics.	Unpaired t-test $p < 0.0001$
S5J ELKS2 clusters/ $\mu\text{m}$ of TH axon	Munc13 control = 0.32 $\pm$ 0.02, median: 0.34 (n = <b>37 images</b> , 3 mice) Munc13 cKO <sup>DA</sup> = 0.42 $\pm$ 0.04, median: 0.41 (n =	Unpaired t-test $p = 0.021$

	<p><b>37 images</b>, 3 mice)  Each circle in the figure represents an image that has been used for sample size in statistics.</p>	
<p>S5K  ELKS2 cluster volume  (x 0.01 <math>\mu\text{m}^3</math>)</p>	<p>Munc13 control = <math>1.76 \pm 0.06</math>, median: 1.88 (n = <b>37 images</b>, 3 mice)  Munc13 cKO<sup>DA</sup> = <math>1.60 \pm 0.06</math>, median: 1.51 (n = <b>37 images</b>, 3 mice)  Each circle in the figure represents an image that has been used for sample size in statistics.</p>	<p>Unpaired t-test  p = 0.083</p>



**Table S6. Means, number of observations and statistical testing, related to Figs. 6 and S6**

For each dataset, mean  $\pm$  SEM are shown in the corresponding figure. The sample size that has been used for statistical testing is shown in bold for each data set.

Figure Parameter (units)	Mean $\pm$ SEM and sample size	Statistical test p-value
6C Peak dopamine evoked by a 10 Hz train of optogenetic stimulation normalized to the 1 <sup>st</sup> peak amplitude of RIM-BP control (mean $\pm$ SEM for stimulus 2, 6 and 10 are listed here)	RIM-BP control stimulus 2: $0.28 \pm 0.05$ ; stimulus 6: $0.07 \pm 0.01$ and stimulus 10: $0.06 \pm 0.01$ . RIM-BP cKO <sup>DA</sup> stimulus 2: $0.24 \pm 0.05$ ; stimulus 6: $0.06 \pm 0.01$ and stimulus 10: $0.06 \pm 0.01$ . Each circle in the figure represents the mean $\pm$ SEM from all recorded slices; RIM-BP control = <b>8 slices</b> , 5 mice and RIM-BP cKO <sup>DA</sup> = <b>8 slices</b> , 5 mice.	Two-way ANOVA ( $p = 0.6$ , $F = 0.2854$ for genotype; $p < 0.0001$ , $F = 106.7$ for stimulus number and $p = 0.9$ , $F = 0.349$ for interaction) followed by Sidak's multiple comparisons tests between RIM-BP control vs. RIM-BP cKO <sup>DA</sup> for each stimulus: stimulus 1-10 ( $p > 0.8$ ).
6C inset 1 Peak dopamine ( $\mu\text{M}$ ) evoked by the 1 <sup>st</sup> stimulus of a 10 Hz train of optogenetic stimulation	RIM-BP control = $0.60 \pm 0.07$ (n = <b>8 slices</b> , 5 mice) RIM-BP cKO <sup>DA</sup> = $0.57 \pm 0.06$ (n = <b>8 slices</b> , 5 mice) Each circle in the figure represents a slice recording that has been used for sample size in statistics; sample size as in Fig. 6C.	Mann-Whitney test $p = 0.7$
6C inset 2 Paired pulse ratio (PPR) of the 2 <sup>nd</sup> to the 1 <sup>st</sup> response in a 10 Hz train of optogenetic stimulation	RIM-BP control = $0.26 \pm 0.03$ (n = <b>8 slices</b> , 5 mice) RIM-BP cKO <sup>DA</sup> = $0.23 \pm 0.03$ (n = <b>8 slices</b> , 5 mice) Each circle in the figure represents a slice recording that has been used for sample size in statistics; sample size as in Fig. 6C.	Mann-Whitney t-test $p = 0.6$
6D 20-80% rise time (ms) of the response evoked by the 1 <sup>st</sup> stimulus of a 10 Hz train of optogenetic stimulation	RIM-BP control = $1.97 \pm 0.24$ (n = <b>8 slices</b> , 5 mice) RIM-BP cKO <sup>DA</sup> = $2.29 \pm 0.25$ (n = <b>8 slices</b> , 5 mice) Each circle in the figure represents a slice recording that has been used for sample size in statistics.	Mann-Whitney test $p = 0.3$
6F Peak dopamine ( $\mu\text{M}$ ) evoked by a KCl puff	RIM-BP control = $5.99 \pm 0.88$ (n = <b>8 slices</b> , 3 mice) RIM-BP cKO <sup>DA</sup> = $5.02 \pm 0.39$ (n = <b>8 slices</b> , 3 mice) Each circle in the figure represents a slice recording that has been used for sample size in statistics.	Mann-Whitney test $p = 0.2$
6G Total dopamine ( $\times 100 \mu\text{M} \times \text{s}$ ) evoked by a KCl puff	RIM-BP control = $1.40 \pm 0.17$ (n = <b>8 slices</b> , 3 mice) RIM-BP cKO <sup>DA</sup> = $1.12 \pm 0.06$ (n = <b>8 slices</b> , 3 mice) Each circle in the figure represents a slice recording that has been used for sample size in statistics.	Mann-Whitney test $p = 0.1$

<p>S6B Peak dopamine (<math>\mu\text{M}</math>) evoked by single electrical pulses at increasing stimulation intensities of 10-90 <math>\mu\text{A}</math> (mean <math>\pm</math> SEM for 10 <math>\mu\text{A}</math>, 50 <math>\mu\text{A}</math> and 90 <math>\mu\text{A}</math> are listed here)</p>	<p>RIM-BP control 10 <math>\mu\text{A}</math>: <math>0.09 \pm 0.02</math>; 50 <math>\mu\text{A}</math>: <math>0.76 \pm 0.09</math> and 90 <math>\mu\text{A}</math>: <math>0.74 \pm 0.07</math>. RIM-BP cKO<sup>DA</sup> 10 <math>\mu\text{A}</math>: <math>0.06 \pm 0.02</math>; 50 <math>\mu\text{A}</math>: <math>0.68 \pm 0.07</math> and 90 <math>\mu\text{A}</math>: <math>0.72 \pm 0.06</math>. Each circle in the figure represents the mean <math>\pm</math> SEM from all recorded slices; RIM-BP control = <b>16 slices</b>, 5 mice and RIM-BP cKO<sup>DA</sup> = <b>16 slices</b>, 5 mice.</p>	<p>Two-way ANOVA (<math>p = 0.3</math>, <math>F = 0.9502</math> for genotype; <math>p &lt; 0.0001</math>, <math>F = 49.17</math> for stimulus intensity and <math>p = 0.9</math>, <math>F = 0.3909</math> for interaction) followed by Sidak's multiple comparisons tests between RIM-BP control vs. RIM-BP cKO<sup>DA</sup> for each stimulus intensity: 10-90 <math>\mu\text{A}</math> (<math>p &gt; 0.3</math>).</p>
<p>S6D Peak dopamine evoked by a 10 Hz train of electrical stimulation at 90 <math>\mu\text{A}</math> normalized to the 1<sup>st</sup> peak amplitude of RIM-BP control (mean <math>\pm</math> SEM for stimulus 2, 6 and 10 are listed here)</p>	<p>RIM-BP control stimulus 2: <math>0.025 \pm 0.004</math>; stimulus 6: <math>0.028 \pm 0.004</math> and stimulus 10: <math>0.029 \pm 0.003</math>. RIM-BP cKO<sup>DA</sup> stimulus 2: <math>0.026 \pm 0.003</math>; stimulus 6: <math>0.026 \pm 0.004</math> and stimulus 10: <math>0.027 \pm 0.004</math>. Each circle in the figure represents the mean <math>\pm</math> SEM from all recorded slices; RIM-BP control = <b>8 slices</b>, 4 mice and RIM-BP cKO<sup>DA</sup> = <b>8 slices</b>, 4 mice.</p>	<p>Two-way ANOVA (<math>p = 0.6</math>, <math>F = 0.2839</math> for genotype; <math>p &lt; 0.0001</math>, <math>F = 170.5</math> for stimulus number and <math>p = 0.9</math>, <math>F = 0.1706</math> for interaction) followed by Sidak's multiple comparisons tests between RIM-BP control vs. RIM-BP cKO<sup>DA</sup> for each stimulus: stimulus 1-10 (<math>p &gt; 0.8</math>).</p>
<p>S6D inset Peak dopamine (<math>\mu\text{M}</math>) evoked by 1<sup>st</sup> stimulus of a 10 Hz train of electrical stimulation</p>	<p>RIM-BP control = <math>0.97 \pm 0.14</math> (<math>n = \mathbf{8 slices}</math>, 4 mice) RIM-BP cKO<sup>DA</sup> = <math>0.89 \pm 0.09</math> (<math>n = \mathbf{8 slices}</math>, 4 mice) Each circle in the figure represents a slice recording that has been used for sample size in statistics; sample size as in Fig. S6D.</p>	<p>Mann-Whitney test <math>p = 0.9</math></p>

**Table S7. Means, medians, number of observations and statistical testing, related to Figs. 7 and S7**

For each dataset, mean  $\pm$  SEM are shown in the corresponding figure, except for Fig. 7E (mean  $\pm$  SD). For image data, median values are reported in the tables in addition to mean  $\pm$  SEM. The sample size that has been used for statistical testing is shown in bold for each data set.

Figure Parameter (units)	Mean $\pm$ SEM and sample size Median (for imaging data only)	Statistical test p-value
7C TH volume/image volume ( $\mu\text{m}^3/\mu\text{m}^3$ )	Liprin- $\alpha$ control = $0.056 \pm 0.003$ , median: 0.05 (n = <b>84 images</b> , 4 mice) Liprin- $\alpha$ cKO <sup>DA</sup> = $0.051 \pm 0.003$ , median: 0.043 (n = <b>85 images</b> , 4 mice) The distribution of images in the figure is shown as violin plots with superimposed mean $\pm$ SEM.	Unpaired t-test p = 0.2
7D TH length/image volume ( $\mu\text{m}/\mu\text{m}^3$ )	Liprin- $\alpha$ control = $0.69 \pm 0.03$ , median: 0.62 (n = <b>84 images</b> , 4 mice) Liprin- $\alpha$ cKO <sup>DA</sup> = $0.63 \pm 0.03$ , median: 0.55 (n = <b>85 images</b> , 4 mice) The distribution of images in the figure is shown as violin plots with superimposed mean $\pm$ SEM.	Unpaired t-test p = 0.2
7E Fraction of the TH surface area at increasing distances from the medial axis of the TH axon (mean $\pm$ SD and medians for 0.2 $\mu\text{m}$ , 0.4 $\mu\text{m}$ , and 0.6 $\mu\text{m}$ are listed here)	Liprin- $\alpha$ control 0.2 $\mu\text{m}$ : $0.187 \pm 0.014$ , median: 0.19; 0.4 $\mu\text{m}$ : $0.024 \pm 0.009$ , median: 0.024 and 0.6 $\mu\text{m}$ : $0.002 \pm 0.001$ , median: 0.002. Liprin- $\alpha$ cKO <sup>DA</sup> 0.2 $\mu\text{m}$ : $0.193 \pm 0.014$ , median: 0.195; 0.4 $\mu\text{m}$ : $0.028 \pm 0.007$ , median: 0.028 and 0.6 $\mu\text{m}$ : $0.003 \pm 0.001$ , median: 0.002. Sample size: Liprin- $\alpha$ control = <b>84 images</b> , 4 mice and Liprin- $\alpha$ cKO <sup>DA</sup> = <b>85 images</b> , 4 mice.	Two-way ANOVA (p = 0.9, F = 0.013 for genotype; p < 0.0001, F = 4244 for distance and p < 0.0001, F = 18.55 for interaction)
7F Bassoon clusters/ $\mu\text{m}$ of TH axon	Liprin- $\alpha$ control = $0.45 \pm 0.01$ , median: 0.48 (n = <b>84 images</b> , 4 mice) Liprin- $\alpha$ cKO <sup>DA</sup> = $0.50 \pm 0.01$ , median: 0.51 (n = <b>85 images</b> , 4 mice) The distribution of images in the figure is shown as violin plots with superimposed mean $\pm$ SEM.	Unpaired t-test p = 0.0005
7G Bassoon cluster volume (x 0.01 $\mu\text{m}^3$ )	Liprin- $\alpha$ control = $1.47 \pm 0.02$ , median: 1.5 (n = <b>84 images</b> , 4 mice) Liprin- $\alpha$ cKO <sup>DA</sup> = $1.49 \pm 0.02$ , median: 1.49 (n = <b>85 images</b> , 4 mice) The distribution of images in the figure is shown as violin plots with superimposed mean $\pm$ SEM.	Unpaired t-test p = 0.5
7I Peak dopamine evoked by a 10 Hz train of optogenetic stimulation normalized to the 1 <sup>st</sup> peak amplitude of Liprin- $\alpha$ control (mean $\pm$ SEM for stimulus 2, 6 and 10 are listed here)	Liprin- $\alpha$ control stimulus 2: $0.32 \pm 0.03$ ; stimulus 6: $0.11 \pm 0.01$ and stimulus 10: $0.09 \pm 0.01$ . Liprin- $\alpha$ cKO <sup>DA</sup> stimulus 2: $0.18 \pm 0.02$ ; stimulus 6: $0.06 \pm 0.01$ and stimulus 10: $0.05 \pm 0.01$ . Each circle in the figure represents the mean $\pm$ SEM from all recorded slices; Liprin- $\alpha$ control = <b>11 slices</b> , 4 mice and Liprin- $\alpha$ cKO <sup>DA</sup> = <b>11 slices</b> , 4 mice.	Two-way ANOVA (p = 0.0008, F = 22.05 for genotype; p < 0.0001, F = 226.5 for stimulus number and p < 0.0001, F = 17.21 for interaction) followed by Sidak's multiple comparisons tests between Liprin- $\alpha$ control vs. Liprin- $\alpha$ cKO <sup>DA</sup> for stimulus number: stimulus 1-2 (p <

		0.0001); and stimulus 3-10 ( $p > 0.06$ ).
7I inset 1 Peak dopamine ( $\mu\text{M}$ ) evoked by the 1 <sup>st</sup> stimulus of a 10 Hz train of optogenetic stimulation	Liprin- $\alpha$ control = $0.56 \pm 0.05$ (n = <b>11 slices</b> , 4 mice) Liprin- $\alpha$ cKO <sup>DA</sup> = $0.32 \pm 0.03$ (n = <b>11 slices</b> , 4 mice) Each circle in the figure represents a slice recording that has been used for sample size in statistics, sample size as in Fig. 7I.	Mann-Whitney test $p = 0.0003$
7I inset 2 Paired pulse ratio (PPR) of the 2 <sup>nd</sup> to the 1 <sup>st</sup> response in a 10 Hz train of optogenetic stimulation	Liprin- $\alpha$ control = $0.32 \pm 0.01$ (n = <b>11 slices</b> , 4 mice) Liprin- $\alpha$ cKO <sup>DA</sup> = $0.33 \pm 0.02$ (n = <b>11 slices</b> , 4 mice) Each circle in the figure represents a slice recording that has been used for sample size in statistics, sample size as in Fig. 7I.	Mann-Whitney t-test $p = 0.3$
7J 20-80% rise time (ms) of the response evoked by the 1 <sup>st</sup> stimulus of a 10 Hz train of optogenetic stimulation	Liprin- $\alpha$ control = $2.16 \pm 0.12$ (n = <b>11 slices</b> , 4 mice) Liprin- $\alpha$ cKO <sup>DA</sup> = $2.32 \pm 0.10$ (n = <b>11 slices</b> , 4 mice) Each circle in the figure represents a slice recording that has been used for sample size in statistics.	Mann-Whitney test $p = 0.3$
7L Peak dopamine ( $\mu\text{M}$ ) evoked by a KCl puff	Liprin- $\alpha$ control = $4.50 \pm 0.50$ (n = <b>12 slices</b> , 8 mice) Liprin- $\alpha$ cKO <sup>DA</sup> = $2.82 \pm 0.36$ (n = <b>12 slices</b> , 8 mice) Each circle in the figure represents a slice recording that has been used for sample size in statistics.	Mann-Whitney test $p = 0.01$
7M Total dopamine ( $\times 100 \mu\text{M} \times \text{s}$ ) evoked by a KCl puff	Liprin- $\alpha$ control = $1.24 \pm 0.13$ (n = <b>12 slices</b> , 8 mice) Liprin- $\alpha$ cKO <sup>DA</sup> = $0.72 \pm 0.09$ (n = <b>12 slices</b> , 8 mice) Each circle in the figure represents a slice recording that has been used for sample size in statistics.	Mann-Whitney test $p = 0.002$
S7B Peak dopamine ( $\mu\text{M}$ ) evoked by single electrical pulses at increasing stimulation intensities of 10-90 $\mu\text{A}$ (mean $\pm$ SEM for 10 $\mu\text{A}$ , 50 $\mu\text{A}$ and 90 $\mu\text{A}$ are listed here)	Liprin- $\alpha$ control 10 $\mu\text{A}$ : $0.03 \pm 0.01$ ; 50 $\mu\text{A}$ : $0.52 \pm 0.04$ and 90 $\mu\text{A}$ : $0.69 \pm 0.07$ . Liprin- $\alpha$ cKO <sup>DA</sup> 10 $\mu\text{A}$ : $0.07 \pm 0.02$ ; 50 $\mu\text{A}$ : $0.48 \pm 0.05$ and 90 $\mu\text{A}$ : $0.63 \pm 0.07$ . Each circle in the figure represents the mean $\pm$ SEM from all recorded slices; Liprin- $\alpha$ control = <b>12 slices</b> , 8 mice and Liprin- $\alpha$ cKO <sup>DA</sup> = <b>12 slices</b> , 8 mice.	Two-way ANOVA ( $p = 0.6$ , $F = 0.1755$ for genotype; $p < 0.0001$ , $F = 61.02$ for stimulus intensity and $p = 0.8$ , $F = 0.4974$ for interaction) followed by Sidak's multiple comparisons tests between Liprin- $\alpha$ control vs. Liprin- $\alpha$ cKO <sup>DA</sup> for each stimulus intensity: 10-90 $\mu\text{A}$ ( $p > 0.7$ ).
S7D Peak dopamine evoked by a 10 Hz train of electrical stimulation at 90 $\mu\text{A}$ normalized to the 1 <sup>st</sup> peak amplitude of Liprin- $\alpha$ control	Liprin- $\alpha$ control stimulus 2: $0.041 \pm 0.006$ ; stimulus 6: $0.033 \pm 0.006$ and stimulus 10: $0.037 \pm 0.004$ . Liprin- $\alpha$ cKO <sup>DA</sup> stimulus 2: $0.037 \pm 0.004$ ; stimulus 6: $0.028 \pm 0.005$ and stimulus 10: $0.033 \pm 0.004$ .	Two-way ANOVA ( $p = 0.2$ , $F = 1.493$ for genotype; $p < 0.0001$ , $F = 178.9$ for stimulus number and $p = 0.7$ , $F = 0.6439$ for interaction) followed by Sidak's multiple comparisons tests

(mean $\pm$ SEM for stimulus 2, 6 and 10 are listed here)	Each circle in the figure represents the mean $\pm$ SEM from all recorded slices; Liprin- $\alpha$ control = <b>8 slices</b> , 3 mice and Liprin- $\alpha$ cKO <sup>DA</sup> = <b>8 slices</b> , 3 mice.	between Liprin- $\alpha$ control vs. Liprin- $\alpha$ cKO <sup>DA</sup> for each stimulus: stimulus 1-10 ( $p > 0.1$ ).
S7D inset Peak dopamine ( $\mu$ m) evoked by the 1 <sup>st</sup> stimulus of a 10 Hz train of electrical stimulation	Liprin- $\alpha$ control = $0.71 \pm 0.09$ (n = <b>8 slices</b> , 3 mice) Liprin- $\alpha$ cKO <sup>DA</sup> = $0.63 \pm 0.04$ (n = <b>8 slices</b> , 3 mice) Each circle in the figure represents a slice recording that has been used for sample size in statistics; sample size as in Fig. S7D.	Unpaired t-test $p = 0.4$
S7F Amplitude (mV) of the extracellular potential evoked by the 1 <sup>st</sup> stimulus of a 10 Hz train of optogenetic stimulation	Liprin- $\alpha$ control = $0.031 \pm 0.004$ (n = <b>12 slices</b> , 3 mice) Liprin- $\alpha$ control + TTX = $0.014 \pm 0.002$ (n = <b>12 slices</b> , 3 mice) Liprin- $\alpha$ cKO <sup>DA</sup> = $0.031 \pm 0.003$ (n = <b>12 slices</b> , 3 mice) Liprin- $\alpha$ cKO <sup>DA</sup> + TTX = $0.015 \pm 0.002$ (n = <b>12 slices</b> , 3 mice). Each circle in the figure represents a slice recording that has been used for sample size in statistics.	Repeated measures one-way ANOVA ( $p < 0.0001$ , $F = 11.06$ ) followed by Sidak's multiple comparisons tests for specific pairs: Liprin- $\alpha$ control vs. Liprin- $\alpha$ control + TTX ( $p = 0.0005$ ); Liprin- $\alpha$ control vs. Liprin- $\alpha$ cKO <sup>DA</sup> ( $p > 0.9$ ); Liprin- $\alpha$ cKO <sup>DA</sup> vs. Liprin- $\alpha$ cKO <sup>DA</sup> + TTX ( $p = 0.0011$ ); and Liprin- $\alpha$ control + TTX vs. Liprin- $\alpha$ cKO <sup>DA</sup> + TTX ( $p > 0.9$ ).
S7G Amplitudes of the extracellular potentials evoked by a 10 Hz train of optogenetic stimulation normalized to the 1 <sup>st</sup> peak amplitude of Liprin- $\alpha$ control (mean $\pm$ SEM for stimulus 2, 6 and 10 are listed here)	Liprin- $\alpha$ control stimulus 2: $1.00 \pm 0.12$ ; stimulus 6: $0.99 \pm 0.12$ and stimulus 10: $0.99 \pm 0.12$ . Liprin- $\alpha$ cKO <sup>DA</sup> stimulus 2: $0.98 \pm 0.11$ ; stimulus 6: $0.99 \pm 0.10$ and stimulus 10: $0.97 \pm 0.11$ . Each circle in the figure represents the mean $\pm$ SEM from all recorded slices; Liprin- $\alpha$ control = <b>12 slices</b> , 3 mice and Liprin- $\alpha$ cKO <sup>DA</sup> = <b>12 slices</b> , 3 mice.	Two-way ANOVA ( $p = 0.9$ , $F = 0.006742$ for genotype; $p = 0.7$ , $F = 0.6628$ for stimulus number and $p = 0.8$ , $F = 0.5567$ for interaction).

**Table S8. Means, number of observations and statistical testing, related to Figs. 8 and S8**

For each dataset, mean  $\pm$  SEM are shown in the corresponding figure. The sample size that has been used for statistical testing is shown in bold for each data set.

Figure Parameter (units)	Mean $\pm$ SEM and sample size	Statistical test p-value
8C Peak dopamine ( $\mu$ M) evoked by a 90 $\mu$ A electrical stimulus	RIM cKO <sup>DA</sup> = 0.08 $\pm$ 0.01 (n = <b>16 slices</b> , 4 mice) RIM cKO <sup>DA</sup> + RIM1-ZnC <sub>2</sub> B = 0.42 $\pm$ 0.03 (n = <b>16 slices</b> , 4 mice) Each circle in the figure represents a slice recording that has been used for sample size in statistics.	Mann-Whitney test p < 0.0001
8E Peak dopamine ( $\mu$ M) evoked by a 90 $\mu$ A electrical stimulus	RIM cKO <sup>DA</sup> + RIM1-ZnC <sub>2</sub> B = 0.39 $\pm$ 0.04 (n = <b>22 slices</b> , 5 mice) RIM cKO <sup>DA</sup> + RIM1-ZnC <sub>2</sub> B <sup>KE</sup> = 0.08 $\pm$ 0.01 (n = <b>20 slices</b> , 5 mice) Each circle in the figure represents a slice recording that has been used for sample size in statistics.	Mann-Whitney test p < 0.0001
8G Peak dopamine ( $\mu$ M) evoked by a 90 $\mu$ A electrical stimulus	RIM cKO <sup>DA</sup> = 0.05 $\pm$ 0.01 (n = <b>19 slices</b> , 4 mice) RIM cKO <sup>DA</sup> + RIM1-ZnPCP = 0.09 $\pm$ 0.02 (n = <b>19 slices</b> , 4 mice) Each circle in the figure represents a slice recording that has been used for sample size in statistics.	Mann-Whitney test p = 0.042
8I Peak dopamine ( $\mu$ M) evoked by a KCl puff	RIM cKO <sup>DA</sup> = 0.38 $\pm$ 0.07 (n = <b>18 slices</b> , 4 mice) RIM cKO <sup>DA</sup> + RIM1-ZnC <sub>2</sub> B = 1.40 $\pm$ 0.14 (n = <b>18 slices</b> , 4 mice) Each circle in the figure represents a slice recording that has been used for sample size in statistics.	Mann-Whitney test p < 0.0001
8K Peak dopamine ( $\mu$ M) evoked by a KCl puff	RIM cKO <sup>DA</sup> + RIM1-ZnC <sub>2</sub> B = 2.42 $\pm$ 0.24 (n = <b>23 slices</b> , 5 mice) RIM cKO <sup>DA</sup> + RIM1-ZnC <sub>2</sub> B <sup>KE</sup> = 2.13 $\pm$ 0.37 (n = <b>21 slices</b> , 5 mice) Each circle in the figure represents a slice recording that has been used for sample size in statistics.	Mann-Whitney test p = 0.1
8M Peak dopamine ( $\mu$ M) evoked by a KCl puff	RIM cKO <sup>DA</sup> = 0.70 $\pm$ 0.11 (n = <b>18 slices</b> , 4 mice) RIM cKO <sup>DA</sup> + RIM1-ZnPCP = 2.70 $\pm$ 0.32 (n = <b>18 slices</b> , 4 mice) Each circle in the figure represents a slice recording that has been used for sample size in statistics.	Mann-Whitney test p < 0.0001
S8B	Control = 1.62 $\pm$ 0.14 (n = 20 slices, 4 mice)	not applicable

Peak dopamine ( $\mu\text{M}$ ) evoked by a 90 $\mu\text{A}$ electrical stimulus	Each circle in the figure represents a slice recording.	
S8C Peak dopamine ( $\mu\text{M}$ ) evoked by a 90 $\mu\text{A}$ electrical stimulus	Control = $1.24 \pm 0.09$ (n = 21 slices, 5 mice) Each circle in the figure represents a slice recording.	not applicable
S8D Peak dopamine ( $\mu\text{M}$ ) evoked by a 90 $\mu\text{A}$ electrical stimulus	Control = $1.16 \pm 0.13$ (n = 15 slices, 4 mice) Each circle in the figure represents a slice recording.	not applicable
S8E Peak dopamine ( $\mu\text{M}$ ) evoked by a 90 $\mu\text{A}$ electrical stimulus	Control = $1.15 \pm 0.07$ (n = 20 slices, 4 mice) Each circle in the figure represents a slice recording.	not applicable
S8F Peak dopamine ( $\mu\text{M}$ ) evoked by a KCl puff	Control = $10.30 \pm 0.53$ (n = 21 slices, 4 mice) Each circle in the figure represents a slice recording.	not applicable
S8G Peak dopamine ( $\mu\text{M}$ ) evoked by a KCl puff	Control = $8.28 \pm 0.57$ (n = 21 slices, 5 mice) Each circle in the figure represents a slice recording.	not applicable
S8H Peak dopamine ( $\mu\text{M}$ ) evoked by a KCl puff	Control = $10.58 \pm 0.77$ (n = 18 slices, 4 mice) Each circle in the figure represents a slice recording.	not applicable
S8I Peak dopamine ( $\mu\text{M}$ ) evoked by a KCl puff	Control = $6.51 \pm 0.78$ (n = 17 slices, 4 mice) Each circle in the figure represents a slice recording.	not applicable
S8K Peak dopamine ( $\mu\text{M}$ ) evoked by a 90 $\mu\text{A}$ electrical stimulus	RIM cKO <sup>DA</sup> = $0.07 \pm 0.01$ (n = <b>20 slices</b> , 4 mice) RIM cKO <sup>DA</sup> + RIM1-ZnC <sub>2</sub> B <sup>KE</sup> = $0.11 \pm 0.01$ (n = <b>21 slices</b> , 4 mice) Each circle in the figure represents a slice recording.	Mann-Whitney test p = 0.04
S8M Peak dopamine ( $\mu\text{M}$ ) evoked by a KCl puff	RIM cKO <sup>DA</sup> = $0.31 \pm 0.05$ (n = <b>17 slices</b> , 4 mice) RIM cKO <sup>DA</sup> + RIM1-ZnC <sub>2</sub> B <sup>KE</sup> = $0.89 \pm 0.11$ (n = <b>18 slices</b> , 4 mice) Each circle in the figure represents a slice recording.	Mann-Whitney test p < 0.0001
S8N Rescue evoked by a 90 $\mu\text{A}$ electrical stimulus normalized to the average of all controls	(a) RIM cKO <sup>DA</sup> + RIM1-Zn + RIM1- $\Delta$ Zn = $0.218 \pm 0.037$ (n = <b>15 slices</b> , 4 mice) (b) RIM cKO <sup>DA</sup> + RIM1-Zn = $0.111 \pm 0.017$ (n = <b>12 slices</b> , 4 mice) (c) RIM cKO <sup>DA</sup> + RIM1- $\Delta$ Zn = $0.039 \pm 0.005$ (n = <b>10 slices</b> , 3 mice) (d) RIM cKO <sup>DA</sup> + RIM1-ZnC <sub>2</sub> B = $0.304 \pm 0.027$ (n = <b>22 slices</b> , 5 mice) (e) RIM cKO <sup>DA</sup> + RIM1-ZnC <sub>2</sub> B <sup>KE</sup> = $0.060 \pm 0.007$ (n = <b>20 slices</b> , 5 mice) (f) RIM cKO <sup>DA</sup> + RIM1-ZnPCP = $0.072 \pm 0.013$ (n = <b>19 slices</b> , 4 mice) Each circle in the figure represents a slice recording. The sample size for control slices that has been used for normalization is <b>72 slices</b> , 20 mice.	One-way ANOVA (p < 0.0001, F = 24.76) followed by Dunnett's multiple comparisons tests where all conditions were compared to RIM cKO <sup>DA</sup> + RIM1-Zn + RIM1- $\Delta$ Zn (a): a vs. b (p = 0.0128); a vs. c (p < 0.0001); a vs. d (p = 0.0230); a vs. e (p < 0.0001); and a vs. f (p < 0.0001).
S8O Rescue evoked by a KCl puff	(a) RIM cKO <sup>DA</sup> + RIM1-Zn + RIM1- $\Delta$ Zn = $0.401 \pm 0.060$ (n = <b>17 slices</b> , 4 mice)	One-way ANOVA (p < 0.0001, F = 6.731) followed by

<p>normalized to the average of all controls</p>	<p>(b) RIM cKO<sup>DA</sup> + RIM1-Zn = 0.147 ± 0.018 (n = <b>11 slices</b>, 4 mice)  (c) RIM cKO<sup>DA</sup> + RIM1-ΔZn = 0.051 ± 0.007 (n = <b>10 slices</b>, 3 mice)  (d) RIM cKO<sup>DA</sup> + RIM1-ZnC<sub>2</sub>B = 0.326 ± 0.033 (n = <b>23 slices</b>, 5 mice)  (e) RIM cKO<sup>DA</sup> + RIM1-ZnC<sub>2</sub>B<sup>KE</sup> = 0.287 ± 0.050 (n = <b>21 slices</b>, 5 mice)  (f) RIM cKO<sup>DA</sup> + RIM1-ZnPCP = 0.364 ± 0.043 (n = <b>18 slices</b>, 4 mice)  Each circle in the figure represents a slice recording. The sample size for control slices that has been used for normalization is <b>73 slices</b>, 20 mice.</p>	<p>Dunnett's multiple comparisons tests where all conditions were compared to RIM cKO<sup>DA</sup> + RIM1-Zn + RIM1-ΔZn (a):  a vs. b (p = 0.0026);  a vs. c (p &lt; 0.0001);  a vs. d (p = 0.5);  a vs. e (p = 0.2); and  a vs. f (p = 0.9).</p>
--	--	---